NUCLEAR STRUCTURE OF THE N=88 ISOTONES: THE DECAY OF 156Tm TO 156Er

A Thesis
Presented to
The Academic Faculty

by

Serkan Dursun

In Partial Fulfillment
of the Requirements for the Degree
Doctor of Philosophy in the
School of Physics

Georgia Institute of Technology
December 2009

NUCLEAR STRUCTURE OF THE N=88 ISOTONES:
THE DECAY OF 156Tm TO 156Er

Approved by:

Dr. John L. Wood, Advisor
School of Physics
Georgia Institute of Technology

Dr. A. Turgay Uzer
School of Physics
Georgia Institute of Technology

Dr. T.A. Brian Kennedy
School of Physics
Georgia Institute of Technology

Dr. W. David Kulp
School of Physics
Georgia Institute of Technology

Dr. Robert A. Braga
School of Chemistry
Georgia Institute of Technology

Date Approved: 11 November 2009

To my parents Fazlı and Elmas,

my wife Zeliha,

my brother Gökhan and my sister Merve

for their endless support and encouragement.

ACKNOWLEDGEMENTS

My graduate years at Georgia Tech Physics Department was a wonderful experience for me. I want to thank the department which has provided to me the great opportunity to make physics and research.

First of all, I want to thank John Wood most of all. Without his perpetual help and motivation I would not be able to finish this thesis. His explanations and teachings about the complex structure of nuclei, analysis of the nuclear data and his suggestions about life and career plans helped me a lot.

I want to, also, thank David for his endless effort to help me with technical issues. I will never forget the patience he showed me to my countless questions about the computational techniques and experimental setup. I want to thank also to my group members Mitch and Nate for their collaboration.

I, also, will never forget Serdar, Huseyin, Serkan B, Se il, for being good friends and the time and enjoyment we had together during our PhD.

Finally, I would like to thank especially my father Fazlı, my mother Elmas, my brother Gökhan, my sister Merve and my beloved wife Zeliha for their endless support, motivation, guidence and love.

TABLE OF CONTENTS

LIST OF TABLES

LIST OF FIGURES

SUMMARY

The N=88 nuclei lie in a transitional region of the nuclear chart. Collective structure and nuclear deformation for this region is commonly occurring. Previously, some of the nuclei having 88 neutrons have been well studied, e.g., ^{148}Nd, ^{150}Sm, ^{152}Gd, ^{154}Dy; however, ^{156}Er has not. To be able to understand the nuclei in this region one needs to extract all the systematics of these deformed nuclei and the relations between them. The structure of ^{156}Er is the main focus in this thesis and the work seeks understanding of the N=88 nuclei and systematics among them. To accomplish this task, ^{156}Tm to ^{156}Er β^+ decay was studied. Many new levels and γ transitions have been added to the existing scheme. The significance for detailed decay scheme studies far from stability is also discussed.

CHAPTER I

INTRODUCTION

Nuclei have an enormously complex structure. To be able to understand the structure and to elucidate the underlying properties of nuclei depends upon experiment. Nuclei exhibit more than simply a spherical shape. The nuclear shape is often prolate deformed. For similar numbers of protons or neutrons, nuclei generally exhibit similar properties. The region, N=88, is one in which the shape of the nuclei is "transitional"; therefore this region has attracted many spectroscopists seeking to identify the structure and characterize the corresponding nuclei.

The development of models based both on quantum mechanical principles and experimental data is the way that the structure of the nucleus is elucidated. The nucleus is a many-body quantum problem.

Even though nuclei with N=88 have been the subject of numerous studies, reliable descriptive models for this region are lacking. In Chapter 2, the main models, i.e., the shell model, the pairing model, and the collective model (including vibrational, rotational and vibrational-rotational behaviors) are discussed in detail to build the theoretical base of our study.

In nuclear structure research, γ-ray transitions between the levels of nuclei are the main source of information. The properties of nuclei are deduced by the observation of γ-ray spectra. To build a complete picture, all γ rays need to be placed in a decay scheme and all spins have to be determined. Beta-decay scheme studies is one of the ways to observe the γ rays. In the β decay of ^{156}Tm to ^{156}Er, a proton turns into a neutron, and ^{156}Er nuclei are left in an excited state due to the mass-energy difference of the parent and daughter nuclei. Excited states de-excite to the ground state by emission of γ ray.

The nucleus, ^{156}Er, is lacking in detailed structural information [1]. The other N=88 isotones, e.g., ^{148}Nd, ^{150}Sm, ^{152}Gd, ^{154}Dy have been the subject of many studies, see the evaluations [2, 3, 4, 5] and references therein. To form a more complete picture, it is desirable to elucidate the structure of ^{156}Er and ^{158}Yb.

Using modern spectroscopic capability in a given detailed analysis of a specific nucleus, $\gtrsim$1000 γ rays can be placed in a level scheme. This depends on Compton-suppressed, background-subtracted γ-γ coincidences with large detector arrays. In the present study an array of 20 Compton-suppressed HPGe (High Purity Germanium Detectors) was used. The focus of this work is γ-γ coincidence spectrometry of ^{156}Er.

CHAPTER II

NUCLEAR MODELS AND NUCLEAR DECAY PROCESSES

2.1 The Nucleus

The nucleus with its constituents, protons and neutrons, constitutes the core of an atom. Nuclei exhibit quantized states similar to atoms. However, the excitation energy of nuclei is far greater than atoms, ranging from keV to MeV, and the excitation pattern is different.

Due to the complexity of the nucleus, models are needed to explain of their structure. Models have to be consistent with observed quantum properties of the nucleus and they have to have predictive power. The shell model is the most fundamental. However, the collective model, and the pairing model also are needed to explain all the phenomena observed in nuclear structure studies.

In a given neighborhood of the Chart of the Nuclides, similar structural features are observed. Usually, one of the models is dominant for that particular region compared to the other models. The physics of nuclear structure is embodied in studying the models through a region of similar (and slowly changing) structure.

2.2 Nuclear Shell Model

The shell model is the fundamental model of nuclear structure because it describes nuclei at the level of independent protons and neutrons. It provides an enormous clarification of the complex nature and structure of the nucleus. The shell structure of nuclei is very similar to the shell stucture of atoms. Even though it is very important to explain nuclear structure at closed or very close to closed shells, it fails or at least does not explain well phenomena further away from closed shells.

Nucleons are spin-1/2 fermions and they obey the Pauli exclusion principle. In the shell model, nucleons occupy single-particle orbitals such that only two are residing in orbitals

with identical spatial quantum numbers. The main strength of the shell model comes from allowing for the Pauli exclusion principle and explaining why the orbitals group into "shells" separated by large energy gaps.

The nuclear Hamiltonian can be expressed as

$$H = H_0 + V, \tag{1}$$

where H_0 is an independent particle Hamiltonian (the sum of the single-particle Hamiltonians) and V describes the residual two-body interactions. The nucleons move under the influence of a spherically symmetric field, and the single-particle Hamiltonian has the simple form

$$h = \frac{p^2}{2m} + U(r), \tag{2}$$

where $U(r) = \frac{1}{2}m\omega^2 r^2$ is commonly used due to the simplicity of the analytical solutions of eigenvectors and eigenvalues of a spherical harmonic oscillator. The eigenvalues of the spherical harmonic oscillator are given by

$$\varepsilon = (N + 3/2)\hbar\omega, \tag{3}$$

where $N = 0, 1, 2....$, and ω is fixed by the size of the nucleus.

The eigenvectors have the form $|N\ell j\Omega\rangle$, where, in addition to N, ℓ is the angular momentum quantum number, $j = \ell + s$ is the total spin, and $\Omega(= m_j)$ is its directional component.

In order to obtain the correct magic numbers (2, 8, 20, 28, 50, 82, 126) it is necessary to add a spin-orbit interaction to the single-particle Hamiltonian. This was first introduced by Goeppert-Mayer [6, 7] and by Haxel, Jensen, Suess [8, 9]. This term takes the form $\epsilon l \cdot s$, where ϵ is an empirically determined energy ($\epsilon < 0$), l is the orbital angular momentum, and s is the intrinsic spin;

$$l \cdot s \mid N\ell j\Omega\rangle = \frac{1}{2}(j^2 - l^2 - s^2) \mid N\ell j\Omega\rangle = \frac{1}{2}(j(j+1) - l(l+1) - s(s+1)) \mid N\ell j\Omega\rangle, \tag{4}$$

with the eigenvalues $\frac{l}{2}$ for $j = l + 1/2$ and $-\frac{(l+1)}{2}$ for $j = l - 1/2$. A term Dl^2 is also added to the Hamiltonan with $D < 0$, so that the l degeneracy is removed, as observed in actual nuclei.

2.3 Pairing Model

Because nucleons are spin-$\frac{1}{2}$ fermions they have a tendency to form proton-proton, neutron-neutron, and even sometimes proton-neutron pairs. In even-even nuclei, the $J = 0$ angular momentum is strongly favored due to the strong pair couplings.

The corresponding pairing interaction Hamiltonian

$$V_p = V^{\pi\pi} + V^{\nu\nu} + (V^{\pi\nu}), \tag{5}$$

where $V^{\pi\pi}$ is the interaction between protons, $V^{\nu\nu}$ is the interaction between neutrons and $V^{\pi\nu}$ is the proton-neutron interaction. The Hamiltonian for π-π or ν-ν can be written in terms of fermion creation and annihilation operators as

$$H = \sum_i \varepsilon_i a_i^+ a_i + \sum_{i,j} V_{i,j} a_j^+ a_{-j}^+ a_{-i} a_i, \tag{6}$$

where the first term describes single-particle degrees of freedom and the second term describes the pairing interactions between the nucleons. If the above equation is approximated with constant terms, $\varepsilon_i = \varepsilon$ and $V_{i,j} = G$, then

$$H = \varepsilon \sum_i a_i^+ a_i + G \sum_{i,j} a_j^+ a_{-j}^+ a_{-i} a_i. \tag{7}$$

For i=1,2 this has the form (for a two-state system)

$$H_0 + V = \begin{pmatrix} \varepsilon + G & G \\ G & \varepsilon + G \end{pmatrix}. \tag{8}$$

A "pairing gap" [10] and the removal of the energy degeneracy are produced by the diagonalization of this matrix, as shown in the Figure 1.

In actual nuclei it is within this pairing gap that collective states are most easy to see and study.

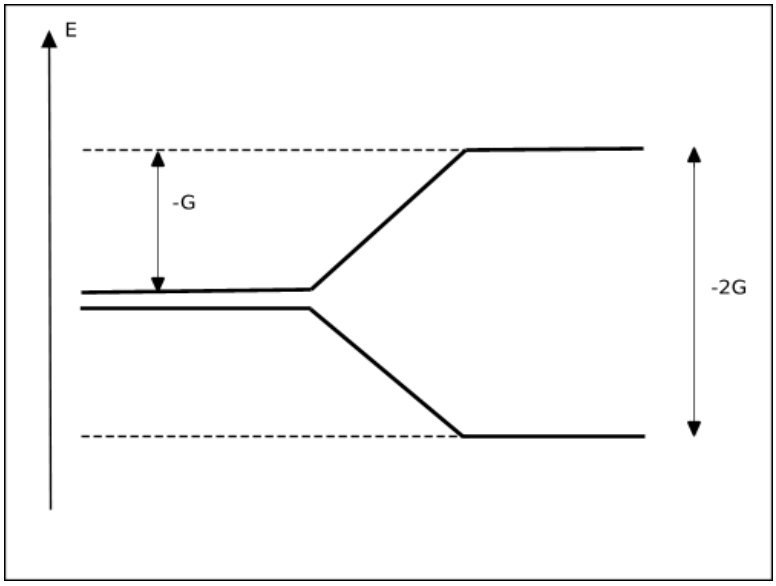

Figure 1: Pairing gap in a two-level pairing model with $G < 0$.

2.4 Collective Model

Shell structure in nuclei is most dominant at or near shell closures. Collective structure is more dominant further away from closed shells.

The collective behavior of the nucleus is similar to that of an incompressible liquid drop [11]. Excitation occurs by changing the shape while conserving the volume of the nucleus. The collective model of the nucleus is parameterized by the radius expansion [12]

$$R(\theta,\psi) = R_{avg}\Big\{1 + \alpha_{00}Y_{00} + \sum_{\mu}\alpha_{2\mu}Y_{2\mu}(\theta,\psi)\Big\}, \qquad \mu = \pm 2, \pm 1, 0, \tag{9}$$

where R_{avg} is the average radius, the quadrupole-spherical harmonics, $Y_{2\mu}$, are the most important terms describing the shape of nuclei, and the Y_{00} term is to conserve the nuclear volume. The orientation of the nucleus in space is characterized by the $\alpha_{2\mu}$ term. The Hill-Wheeler [13] coordinates are introduced here to specify the orientation of the principal axes of the nucleus in space. Correspondingly, the equations below provide the necessary $\alpha_{2\mu}$ dependence,

$$\alpha_0 = \beta cos\gamma, \tag{10}$$

$$\alpha_{2\mu} = \frac{1}{\sqrt{2}}\beta sin\gamma, \tag{11}$$

where β is positive. Particular values for β and γ define, e.g., spherical, prolate, oblate, or triaxial shapes. $\beta = 0$ corresponds to a spherical shape, $\gamma = \pm 60°, -180°$ correspond to oblate shapes and $\gamma = 0°, \pm 120°$ correspond to prolate shapes.

2.4.1 Vibrations

Vibrations of the nucleus are described by time dependence of the nuclear shape parameters $\alpha_{2\mu}$. The eigenvalues of a harmonic quadrupole vibrator are

$$\varepsilon = \hbar\omega(N + 5/2), \tag{12}$$

where N is the number of phonons, and ω is an empirically-determined frequency.

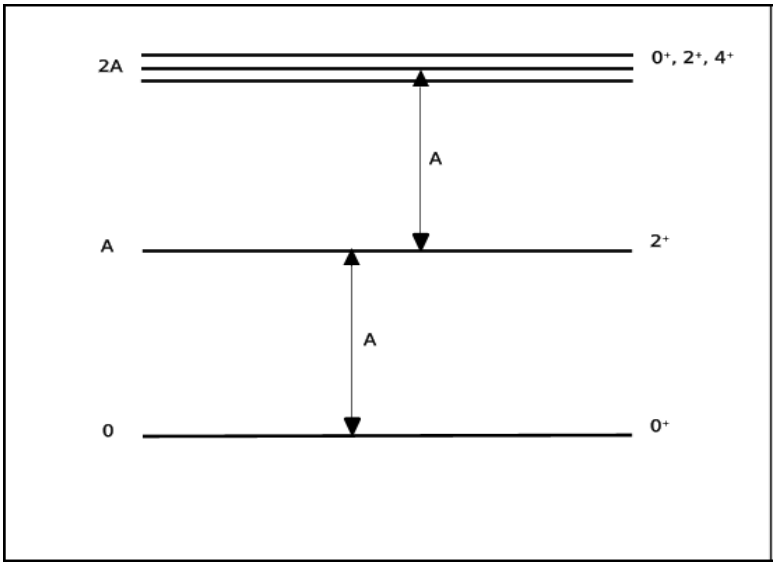

Figure 2: Quadrupole vibrational energy spectrum with $A = \hbar\omega$.

For $N = 0$, $\varepsilon = \frac{5}{2}\hbar\omega$, where $\frac{5}{2}$ describes the zero-point motion of the five dimensions of the quadrupole shape. There is one state with spin-parity 0^+. With the addition of one phonon, a state with 2^+ spin-parity results. With two phonons, states with $0^+, 2^+, 4^+$ result at around twice the one-phonon energy. With three phonons, states with $0^+, 2^+, 3^+, 4^+, 6^+$ result, etc. The low-energy vibrational spectrum of a nucleus is shown in Figure 2.

2.4.2 Rotations

Rotations occur if the shape parameters $\alpha_{2\mu}$ have non-zero, time-independent values. A rotational Hamiltonian for the nucleus is expressed by

$$H = \sum_i \frac{I_i^2}{2\Im_i}, \tag{13}$$

where the $\Im_i$ are the principal moments of inertia, and $\Im_1 = \Im_2 \neq \Im_3$ is a good approximation for most nuclei; with the corresponding Hamiltonian

$$H' = \frac{\hbar^2}{2}\left\{\frac{I^2}{\Im} + (\frac{1}{\Im_3} - \frac{1}{\Im})I_3^2\right\}, \tag{14}$$

and energy eigenvalues

$$E = \frac{\hbar^2}{2}\left\{\frac{I(I+1)}{\Im} + (\frac{1}{\Im_3} - \frac{1}{\Im})K^2\right\}, \tag{15}$$

where the quantum number K is the angular momentum projection on the nuclear symmetry axis.

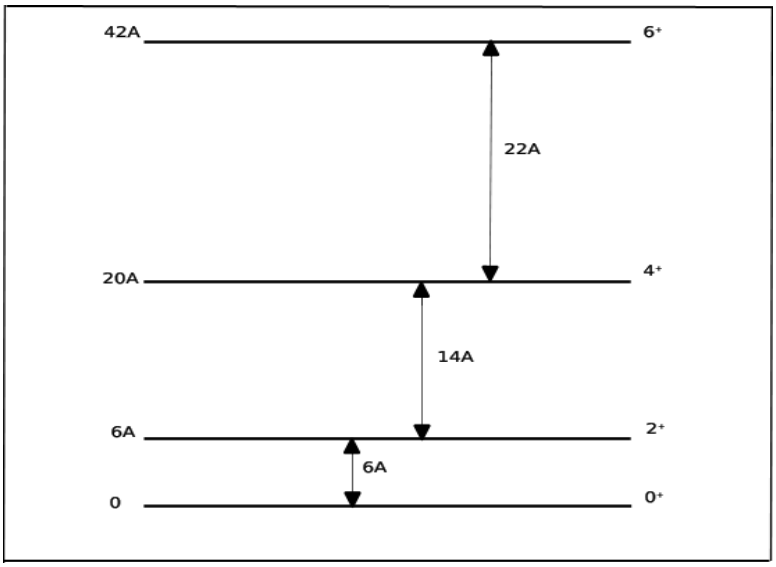

Figure 3: Rotational energy spectrum for $K = 0$ with $A = \frac{\hbar^2}{2\Im}$.

For deformed even-even nuclei, $K = 0$, and

$$E = \frac{\hbar^2}{2\Im} I(I+1). \tag{16}$$

The low-energy rotational spectrum is shown in Figure 3.

The corresponding energy eigenstates are given by

$$|IMK\rangle = \frac{1}{\sqrt{2}}\big\{\ |IM,+K\rangle + (-1)^{I+K}\ |IM,-K\rangle\big\}, \tag{17}$$

where I is the total angular momentum, K is the component of I along the body-fixed symmetry axis, and M is the component of I along the laboratory-fixed z-axis.

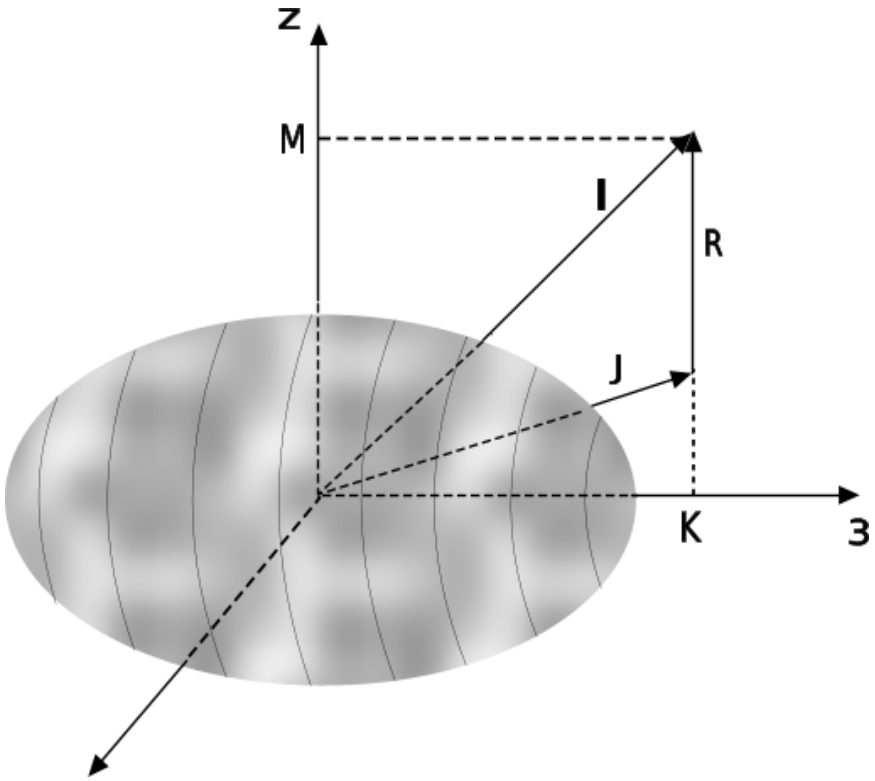

Figure 4: The angular momentum diagram for an axially symmetric rotor where I is the total angular momentum with contributions, R(rotational angular momentum), J(intrinsic angular momentum), K is the component of I(and J) along the body-fixed symmetry axis, and M is the component of I along the laboratory-fixed z-axis.

The angular momentum coupling for a rotor is shown in Figure 4. The prolate shape (the preferred shape for nuclei) of nucleus is depicted in the corresponding figure. For the ground state the K value is simply 0. In even-even nuclei, $K = 0$ produces the spin sequence $I = 0, 2, 4, ...$ due to the reflection symmetry. An odd spin would produce antisymmetric states according to Equation 17. When $K = 2$, the spin sequence would be $I = 2, 3, 4, ...$ and a so-called γ band is produced.

2.4.3 Rotational-vibrational behavior

Nuclei tend to have neither a simple rigid rotational structure nor a simple vibrational structure. The pure vibrational picture yields $E_4/E_2 = 2.00$ and the pure rotational picture yields $E_4/E_2 = 3.33$. However, most nuclei exhibit values in between.

Time dependence of α_{20} yields β vibrations with $K = 0$, and time dependence of $\alpha_{2,\pm2}$ yields γ-vibrations with $K = 2$. The energy spacing between rotational states are smaller than those between vibrational states. A rotational-vibrational spectrum is shown in Figure 5. Geometrical views of β and γ are depicted in Figures 6 and 7, respectively.

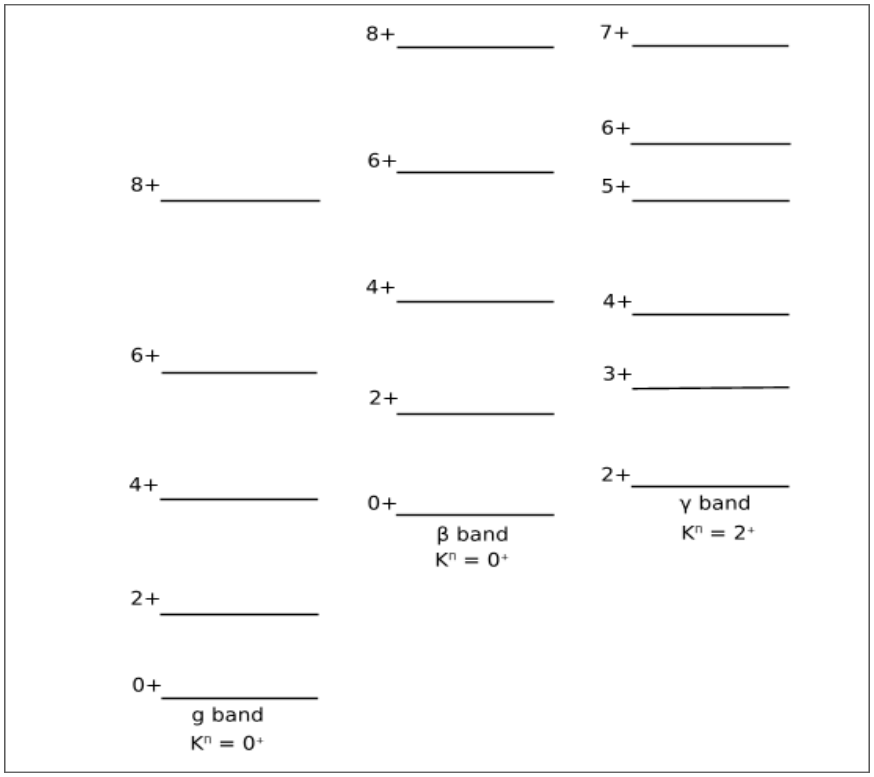

Figure 5: Rotational bands built upon vibrational bands. Ground(g), β-vibrational, and γ-vibrational bands are shown in the figure.

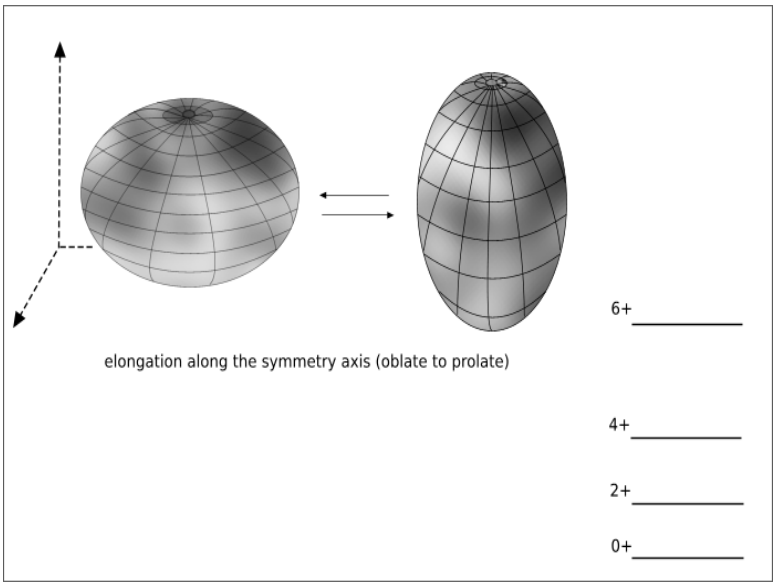

Figure 6: β vibration of the nucleus. The $\alpha_{20}(t)Y_{20}(\theta, \psi)$ term is the parameterization of the radius expansion describing the β vibration in the nucleus.

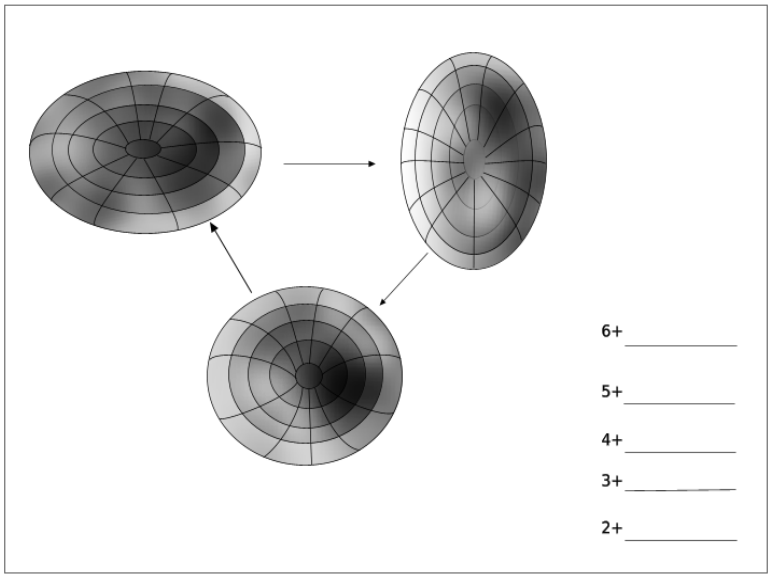

Figure 7: Top-down view of γ vibration of the nucleus. The $\alpha_{22}(t)\{Y_{22}(\theta, \psi) + Y_{2-2}(\theta, \psi)\}$ term is the parameterization of the radius expansion describing the γ vibration in the nucleus.

2.5 Decay Types and Nuclear Transitions

A few important decay types are discussed briefly, which are seen in our experiment when ^{156}Yb decays to more stable nuclei. From [14], more information can be obtained.

2.5.1 β decay

β decay is one of the population methods of excited states of a nucleus. Three different types of β decay occur.

$$n \longrightarrow p + e^- + \overline{\upsilon_e}$$
$$p \longrightarrow n + e^+ + \upsilon_e$$
$$p + e^- \longrightarrow n + \upsilon_e$$

In the first, in a nucleus, a neutron turns into a proton, in which a neutron-rich (proton-deficient) nucleus moves towards stability line. In the second, in a nucleus, a proton turns into a neutron, in which a proton-rich (neutron-deficient) nucleus moves towards the stability line. The third, an electron is captured by the nucleus from an atomic shell with the same result as the second process.

2.5.2 α decay

This nuclear decay type is one in which the proton number and neutron number both decrease by two, and an α particle is emitted.

$$^{A}_{Z}X \longrightarrow ^{A-4}_{Z-2}Y + \alpha$$

2.5.3 γ decay

When an excited state in a nucleus de-excites to a lower state, a γ ray is emitted. The energy of a transition is the difference of the level energies. De-excitation to a lower state occurs in a very short time (half-lives are generally $\sim$-fs to $\sim$-ns). Then, we say that they are in coincidence with each other which means they occur at (almost) the same time. If the structure of the decay is very complex (many γ rays are emitted), coincidence spectroscopy is the most effective method to deduce the structure as opposed to singles spectroscopy.

2.5.4 Multipole radiation

The change of current and charge distributions in nuclei result in magnetic and electric transitions, respectively. The eigenvectors of the initial state and the final state together with the electromagnetic multipole operator lead to a transition matrix element. The angular momentum conservation is expressed by

$$|J_i - J_f| \leq L \leq J_i + J_f, \tag{18}$$

where L is the multipolarity of the transition. Electric multipole radiation, EL obeys the parity-change rule $(-1)^L$, and magnetic multipole radiation, ML obeys the parity-change rule $(-1)^{L+1}$.

The *Weisskopf estimates* [15] are derived from the following equations for transition probabilities. These units are used to compare transition rates. The electric transition probability is expressed by (as described in [14])

$$T(EL) = \frac{8\pi(L+1)}{L[(2L+1)!!]^2}\frac{e^2}{4\pi\epsilon_0\hbar c}\left(\frac{E}{\hbar c}\right)^{2L+1}\left(\frac{3}{L+3}\right)^2 cR^{2L}, \tag{19}$$

where $R = R_0 A^{\frac{1}{3}}$, $R_0 = 1.2$ fm, A is the mass of the nucleus, L is the multipolarity, and E is in units of MeV, T is in s^{-1} .

The magnetic transition probability is expressed by (as described in [14])

$$T(ML) = \frac{8\pi(L+1)}{\hbar L[(2L+1)!!]^2}\left(\mu_p - \frac{1}{L+1}\right)^2\left(\frac{\hbar}{m_p c}\right)^2\left(\frac{e^2}{4\pi\epsilon_0\hbar c}\right)\left(\frac{E}{\hbar c}\right)^{2L+1}\left(\frac{3}{L+2}\right)^2 cR^{2L-2} \tag{20}$$

where L is the multipolarity, $R = R_0 A^{\frac{1}{3}}$, and E is in units MeV, T is in s^{-1}, and μ_p is the magnetic moment of the proton in Bohr magnetons.

The electric transition probability equation can be expressed in terms of a reduced transition probability, $B(EL; J_i \to J_f)$, as follows

$$\Gamma(EL; J_i \to J_f) = \frac{8\pi(L+1)}{\hbar L[(2L+1)!!]^2}\left(\frac{E}{\hbar c}\right)^{2L+1} B(EL; J_i \to J_f), \tag{21}$$

where the unit of $B(EL)$ is $e^2(fm)^{2L}$.

Reduced transition probabilities give fundamental information about the structure of nuclei. It is specific for each nucleus, and it is used to compare different structures. In collective nuclei, the dominant transition type is electric quadrupole. Electric quadrupole transition probabilities depend on transition energy as E^5. However, we observe in nuclei E1 and M1 transitions as well. If the multipolarity increases, the total transition probability decreases by the order of $\times 10^{-5}$ per unit of L.

2.6 Shape Coexistence in Nuclei and E0 Multipolarity

Shape coexistence in nuclei is a known phenomena for a long time. It simply means that there are different types of deformation in a single nucleus. The first suggestion was made by Morinaga [16] and the concept was detailed in the review studies of Heyde *et al.* [17] and Wood *et al.* [18]. It was proven that shape coexistence in a nucleus occurs mainly at and close to closed shells as observed, e.g., in ^{16}O. The ground state of such nuclei is spherical, however, excited states are deformed.

E0 monopole transitions and shape coexistence in nuclei are strongly correlated. The reference [19] explains the correlation between them explicitly. It is useful to define a monopole operator

$$\hat{T}(E0) = \sum_j e_j r_j^2. \tag{22}$$

where e is the charge and r is the position of the corresponding nucleon. Two-photon emission and internal-pair (IP) formation are produced by this operator which couples the nucleus to the electromagnetic field, and internal-conversion (IC) process is produced by coupling the nucleus to the atomic electrons, as well. The IC process mainly occurs through $1s(K)$ and $2s(L_1)$ shells. The transition rate derived from the monopole operator is defined by

$$\frac{1}{\tau(E0)} = \rho_{f_i}^2(\Omega_K + ... + \Omega_{IP}), \tag{23}$$

Consequently the monopole transition rate can be written in terms of the initial and final states

$$\rho_{f_i}^2 = |\frac{\langle \Psi_f | \hat{T}(E0) | \Psi_i \rangle}{eR^2}|^2 \tag{24}$$

where Ω is a non-nuclear term, R is the nuclear radius ($R \simeq 1.2A^{1/3}$ fm), and e is the electrical charge. The quantity ρ involves all the structural information and the connection of nuclear charge radii to the electric monopole operator.

Deformed nuclei having coexisting shapes usually exhibit non-zero $\rho^2(E0)$ values. If the coexisting shapes are mixed, the ρ values are strong. The strength of the E0 transitions results from the difference of the charge radii and the strength of the mixing. Mixing for two configurations can be written as

$$|\Psi_i\rangle = \alpha|1\rangle + \beta|2\rangle, \qquad |\Psi_f\rangle = -\alpha|1\rangle + \beta|2\rangle. \tag{25}$$

The corresponding relation between the monopole operator and two-level mixing is defined in terms of the transition rate

$$\rho(E0)_{fi} = \frac{1}{eR^2}[\alpha\beta(\langle 1|\hat{T}(E0)|1\rangle - \langle 2|\hat{T}(E0)|2\rangle + (\alpha^2 - \beta^2)\langle 2|\hat{T}(E0)|1\rangle]. \tag{26}$$

where different α and β values indicate the strength of mixing. This can show the coexistence of spherical and deformed shapes in a single nucleus. We can argue that stronger E0 transitions indicate greater shape coexistence.

CHAPTER III

PREVIOUS EXPERIMENTAL WORK

The N=88 isotones, except ^{156}Er and ^{158}Yb, have been the subject of a number of studies so far, see the evaluations [2, 3, 4, 5] and references therein. However, our knowledge is very limited [1] for the low-energy, low-spin structure of ^{156}Er. As mentioned earlier, $N = 88$ isotones lie in a transition region from spherical to deformed nuclear shape.

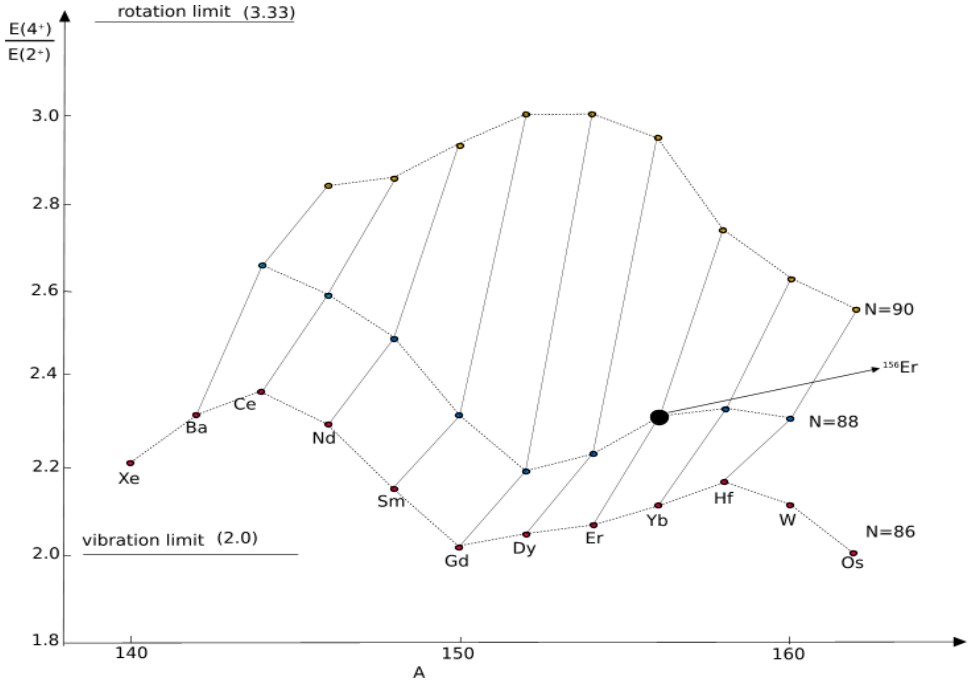

Figure 8: The $E(4^+)/E(2^+)$ energy ratios of the $N = 86, 88, 90$ isotones. (The data are taken from *Nuclear Data Sheets.)*

When the ratio $E(4^+)/E(2^+)$ equals 3.33, a nucleus is rotational (deformed); and when this ratio equals 2.00, a nucleus is vibrational (spherical). The nucleus ^{156}Er lies in between these values. Figure 8 illustrates the ground-state energy ratios $E(4^+)/E(2^+)$ of N=86, N=88, and N=90 isotones neighboring ^{156}Er. Significant shape change is observed, when two neutrons are added to the $N = 88$ isotones, ^{150}Sm, ^{152}Gd, and ^{154}Dy. The nucleus ^{156}Er appears also to exhibit a shape change when two neutrons are added, see the Figure 8.

3.1 Population Methods

Two methods which populate ^{156}Er are given in reference [1], the β decay of ^{156}Tm and heavy ion evaporation studies (they will be discussed in detail below and the actual references will be given accordingly). Beta decay mainly populates low-spin states. In heavy-ion evaporation studies, normally, high-spin states are populated.

3.1.1 Decay Studies-β Decay

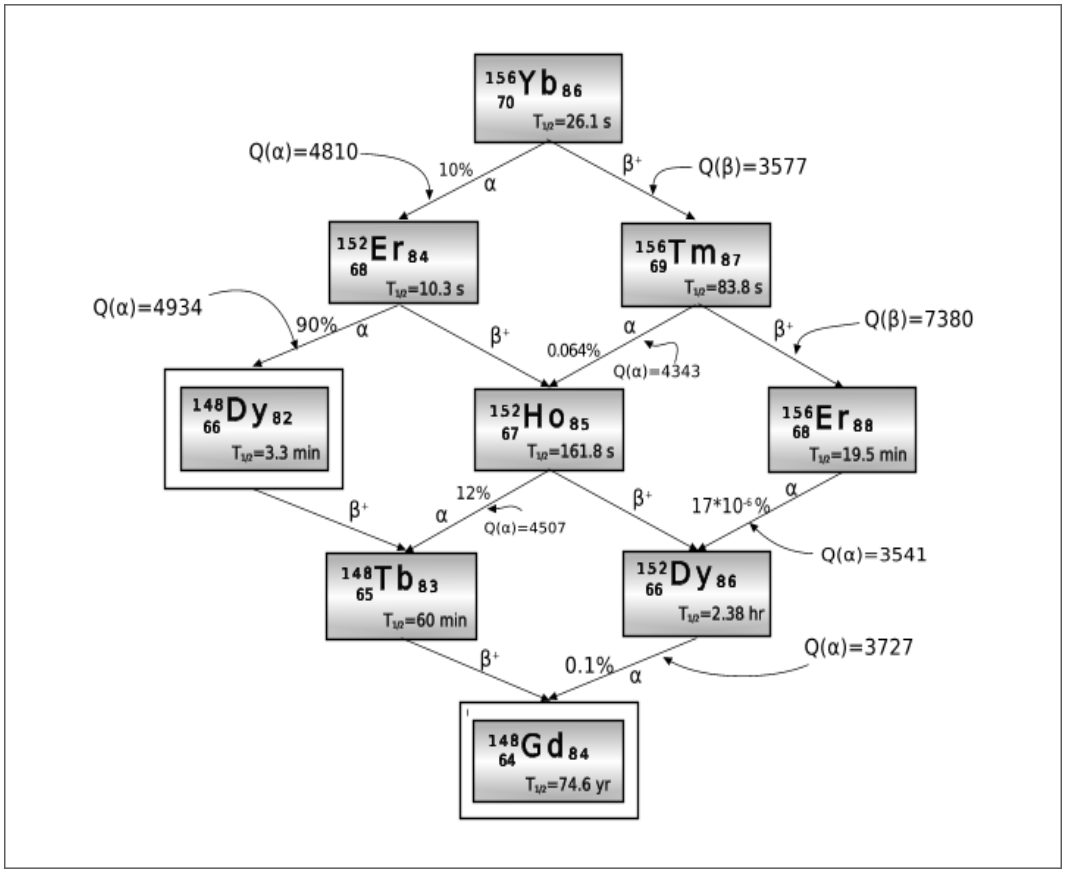

Figure 9: Decay chains of ^{156}Yb and its decay daughters. All α, β/ϵ^+ decays are shown along with Q(α) and Q(β) values (in keV) and half lives, $T_{\frac{1}{2}}$, of the nuclei. (The data are taken from *Nuclear Data Sheets* for A=148, 152, and 156.)

The β decay of a nucleus refers to three different kinds of processes: β^+, β^- or EC (Electron Capture) emissions. The decay is in fact controlled by selection rules for spins. By this decay, low-spin low-energy levels as well as low-spin high-energy levels can be populated..

The decay chains relevant to the present study are shown in Figure 9. Excited states of ^{156}Er are populated by the β decay of the ^{156}Tm isomers ($T_{\frac{1}{2}} = 83.8$ s and 19.0 s [20]). The short half lives of the ^{156}Tm isomers make them difficult to study. There are two studies on the β decay of ^{156}Tm in literature, the studies of Aguer *et al.* [21] and Zolnowski *et al.* [22]. The high Q value of the β decay of ^{156}Tm ($Q(\beta) = 7380 \pm 60$ keV) allows many transitions to occur, shown in Figure 10. It is noticeable that the ground level of ^{156}Er has a relatively longer half life ($T_{\frac{1}{2}} = 19.5$ minute) compared to the ground-state half life of ^{156}Tm. Note that, in Figure 10, the intensity of each γ ray was multiplied by 0.857 in order to obtain absolute intensities per 100 decays [1].

Aguer *et al.* used two Ge(Li) detectors with volumes 30 cm^3, 40 cm^3, and one Si(Li) detector with dimensions 150 $mm^2 \times$ 3 mm. They performed γ-singles, conversion-electron, and γ-γ coincidence spectroscopy. A decay scheme with 16 levels and 30 γ rays were placed in this study. The ground-state band was identified up to spin 6^+, and members of β and γ bands were proposed. Two levels at ∼930 keV were suggested. These two levels were identified as the bandheads of β and γ bands. The β and γ bands were identified up to their 4^+ members. Due to the E1 multipolarity of a transition out of the 1303.6 keV level, they suggested that this level might be a 3^- level of the octupole band.

The second study was performed by Zolnowski *et al.*. The study deduced quasirotational-band structures for each of the N=88 isotones. It also suggested a spin-parity assignment, 3^+, for the parent nucleus (^{156}Tm), whereas the assignment of Aguer *et al.* was 3^+ or 3^-. This study offered a more complete picture compared to the study of Aguer *et al.*. The ^{156}Tm was produced by isotope separation following the reaction $^{148}Sm(^{14}N, 6n)$. Two Ge(Li) detectors with volumes 30 cm^3 and 55 cm^3 and one planar Ge(Li) detector with volume 1 cm^3 were used to observe $\gamma - \gamma$ coincidences. A Si(Li) detector with dimensions 2 $cm^2 \times$ 3 mm was used to detect conversion electrons. γ-ray singles and $\gamma - \gamma$ coincidences were recorded. Twenty levels with 37 transitions, including 11 levels (in common with the study of Aguer *et al.*) were placed. Only the placement of one γ-ray line was different in these two studies. A 3^+ spin-parity assignment to the 1243.0 keV level, as opposed to 3^+

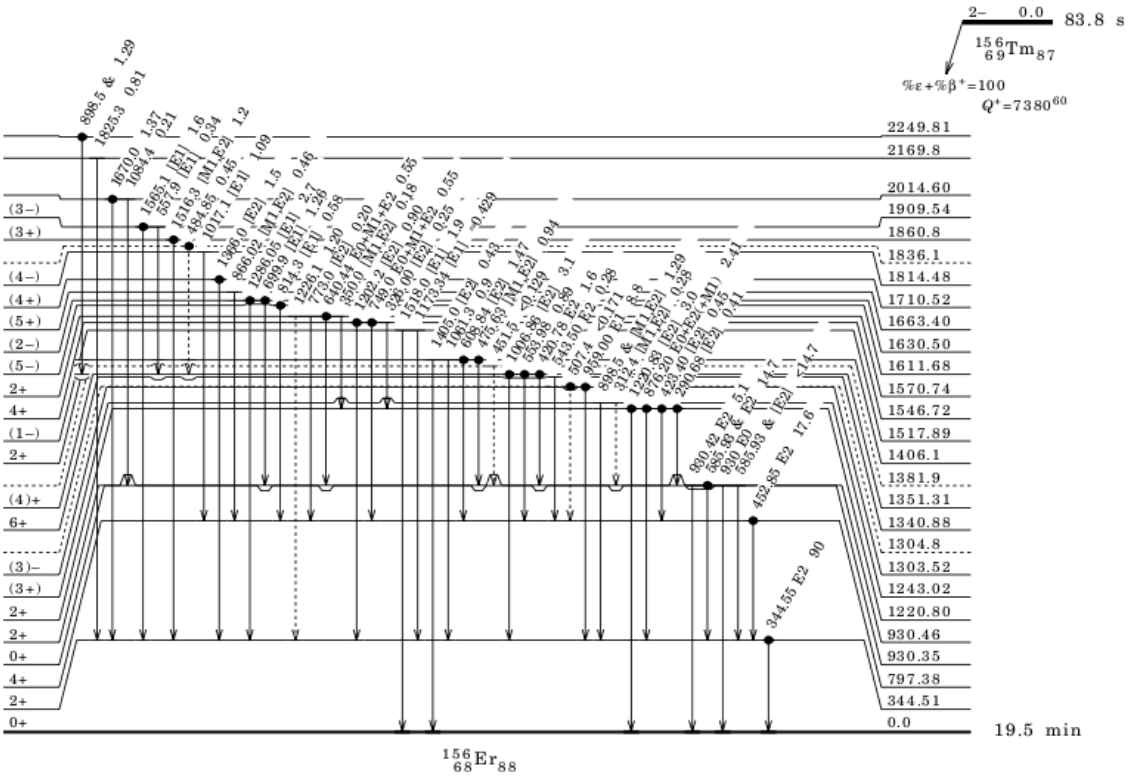

Figure 10: The level scheme of ^{156}Er based on the studies of Aguer *et al.* and Zolnowski *et al.*. (The figure is taken from reference [1].)

spin-parity assignment of 1351.4 keV level in the study of Aguer *et al.*, changed the γ band structure. The 1351.4 keV level became the new 4^+ member of the band. A 1405.9 keV level was suggested as the 2^+ member of a positive-parity even-spin band, contrary to the suggestion of Aguer *et al.* that the level was the 4^+ member of the β-band. The ground-state band was assigned up to 8^+, the γ band up to 5^+, the β band up to 4^+, and a negative-parity band up to 7^- with tentative assignments of 1^- and 5^- levels. And a new octupole negative-parity band was also tentatively assigned. In both studies, the second excited 0^+ state for ^{156}Er, which had been assigned in the neighboring N=88 isotones, was not observed. The second excited 0^+ states were assigned as having 2-phonon β-vibrational character in all other N=88 isotones by [22], due to their large reduced transitional probabilities to the one-phonon β-vibrational states.

The low-energy ground- β- and γ-band systematics of the N=88 isotones are shown in Figure 11. The most complete picture so far is for ^{148}Nd and ^{150}Sm.

3.1.2 Heavy-Ion Evaporation Studies

The remaining information about the nucleus ^{156}Er comes from heavy-ion evaporation reaction studies [23] which give considerable information about high-spin high-energy levels [24, 25, 26, 27]. The study carried out by Stephens *et al*. [27] is the most detailed one. Nine Compton-suppressed Ge detector were used and approximately 100 levels, corresponding to 130 new γ rays were placed. Five different bands were identified consisting of three negative-parity bands extending up to spin-parity 38^-, and two positive-parity bands extending up to spin-parity 43^+.

References [24, 25, 26] also focused on determining the half lives of the levels. The evaluated [1] half lives of the levels are the weighted averages of these three studies.

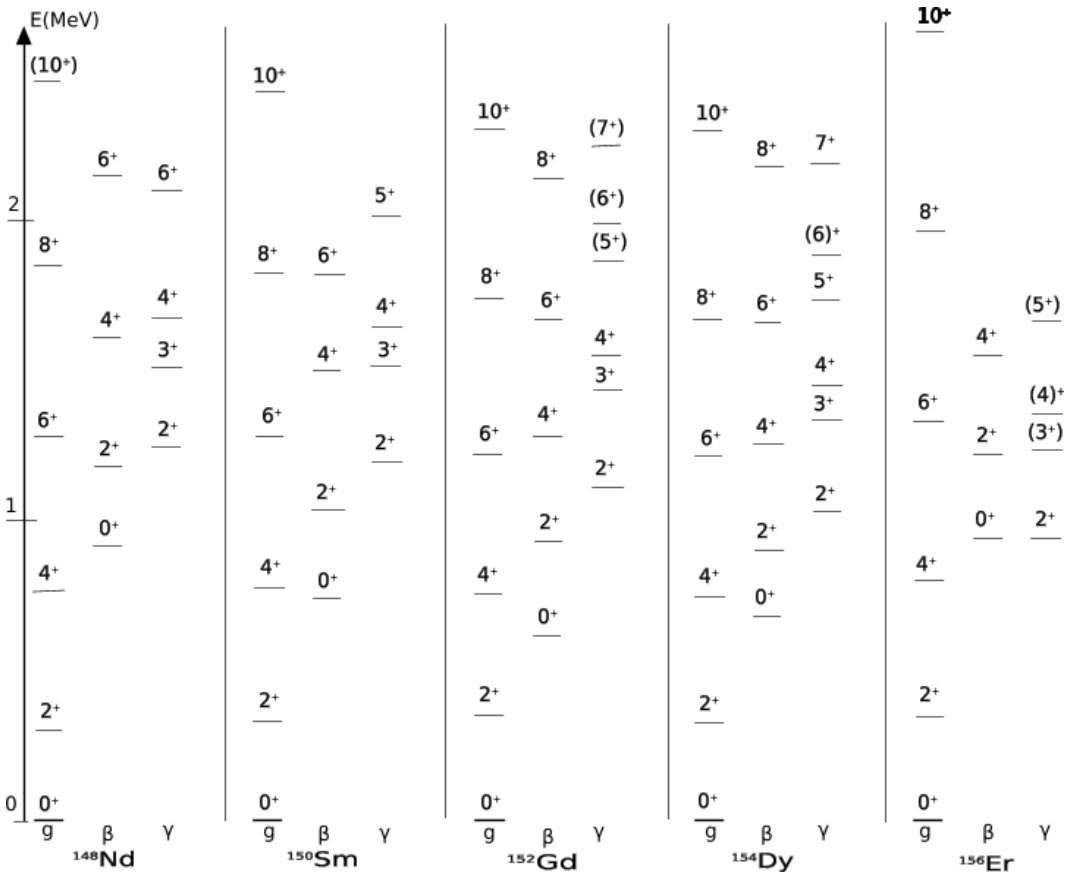

Figure 11: The low-lying ground, β, and γ bands of the $N = 88$ isotones. The nuclei ^{148}Nd and ^{150}Sm provide the most complete picture. (The data are taken from *Nuclear Data Sheets*.)

CHAPTER IV

EXPERIMENTAL PROCEDURE AND THE 8π SPECTROMETER

4.1 Introduction

The experiment was performed at TRIUMF (TRI-Universities Meson Facility), in Vancouver, Canada. TRIUMF has the World's largest cyclotron, a sector-focusing cyclotron capable of up to 400 μA proton beams with energies up to 520 MeV [28]. This accelerator is used to produce the World's highest-power radioactive ion beams [29], delivered to ISAC (Isotope Separator and ACcelerator) facility at TRIUMF, illustrated in Figure 13. Ion beams of radioactive nuclei [30] with half-lives as short as $\sim$8 ms (^{11}Li) have been studied at the 8π Spectrometer in the low-energy ISAC-I area.

4.2 The ISAC Facility and ISOL Method

Radioactive nuclei are produced at TRIUMF/ISAC through the spallation of heavy target nuclei using 500 MeV protons from the TRIUMF cyclotron. Spallation products are accelerated to 60 kV in the target/ion source of the mass separator station, shown in Figure 12. The beam is directed to the experimental hall where it can be delivered to one of the experiments in the low-energy area, or further accelerated for nuclear reactions.

The spallation process produces a great variety of radioactive isotopes. To obtain the desired radioactive ion beam, only specific spallation products are selected using the Isotope separation On-Line (ISOL) method [31, 32]. The ISOL method works by first passing the ion beam through orthogonal electric and magnetic fields in a velocity selector. Next, a uniform magnetic field is used as a momentum selector, in which ions are deflected by different amounts according to mass [14]. The path that an ion follows depends on its mass-to-charge ratio, or A/Q, where V/B (Velocity/Magnetic field) is a constant.

In the present experiment, a 40 μA proton beam impinged upon a target of stacked Ta (tantalum) foils. Those foils were heated to high temperature to promote the release and ionization of the spallation products. The mass separator, set to A/Q=156, provided a nearly pure beam of A=156 nuclei delivered to the 8π experimental station (a small amount of molecular species were detected, as discussed later).

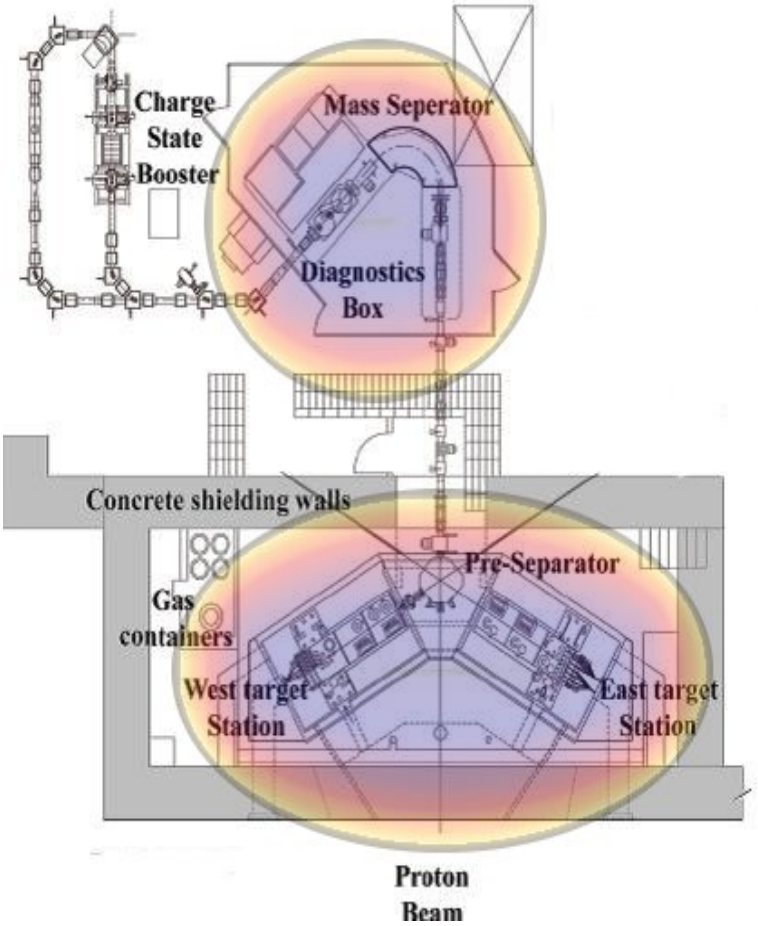

Figure 12: The TRIUMF/ISAC target/ion source and mass separation station [33].

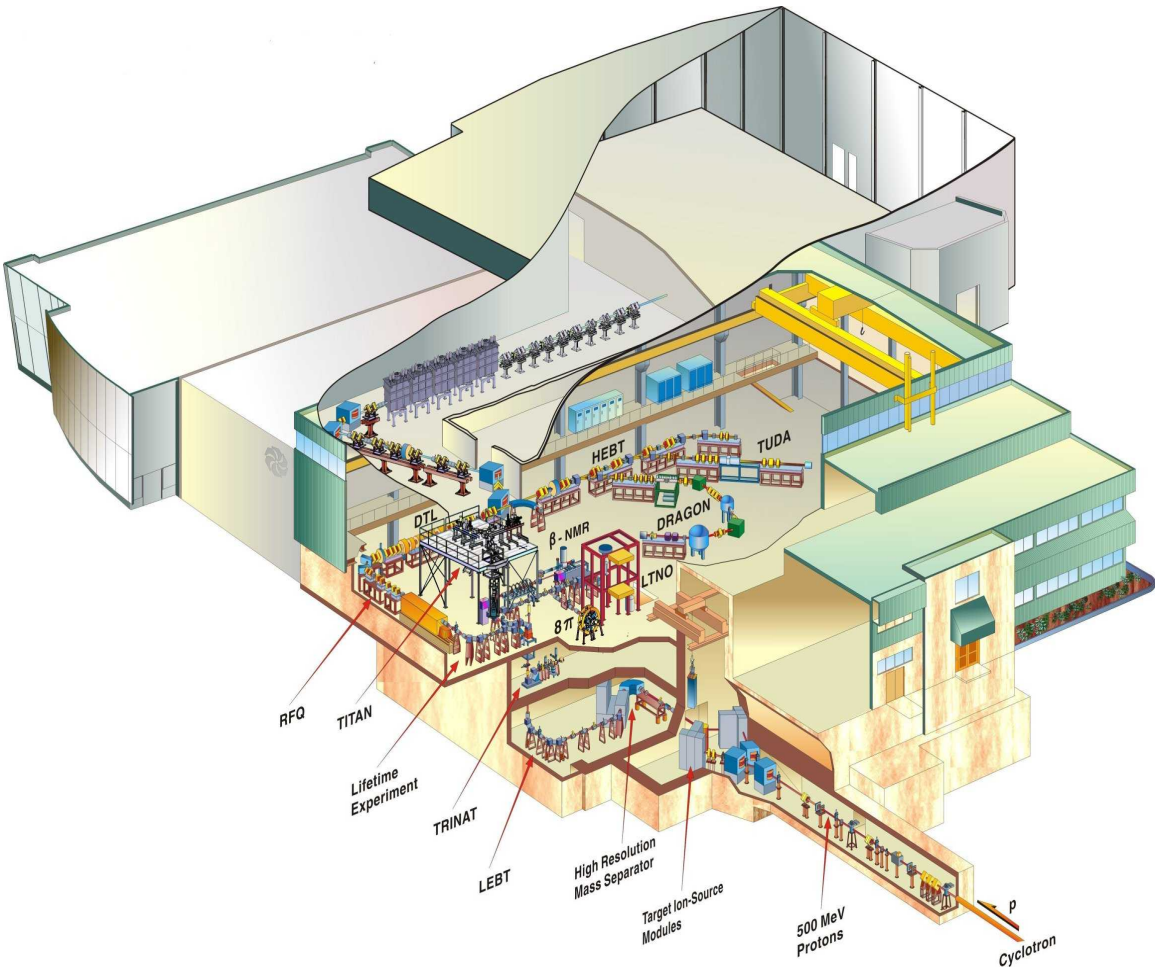

Figure 13: A picture of the TRIUMF/ISAC facility. The proton beam from the cyclotron (shown entering the target area from the bottom-right corner of the figure) strikes the production target, creating radioactive nuclei through spallation. The spallation products are mass separated and delivered to a facility, such as the 8π, in the experimental hall [34].

4.2.1 Spallation Yield

Spallation is the process of breaking up heavy nuclei, e.g, tantalum (Ta) with a high-energy proton beam. This process occurs in Nature when cosmic rays hit the Earth. The semi-empirical formula

$$\sigma \propto e^{(-P\Delta A)} e^{(-R|Z-SA+TA^2|^\nu)} \tag{27}$$

introduced by Silberberg and Tsao [35, 36] is used to approximate the cross section for proton spallation of a thick target.

The $e^{(-P\Delta A)}$ factor in Equation 27, describes the reduction in cross section as the mass difference between target and product increases. The production of isotopes for a given atomic number Z is described by the second exponential factor, $e^{(-R|Z-SA+TA^2|^\nu)}$, where R describes the width of the distribution of the cross sections, S locates the peak of the distribution for a given isotope, and T describes the shift of the distribution to greater neutron excess for heavier isotopes. The parameters P, R, S, T, and ν are determined from fits to experimental data.

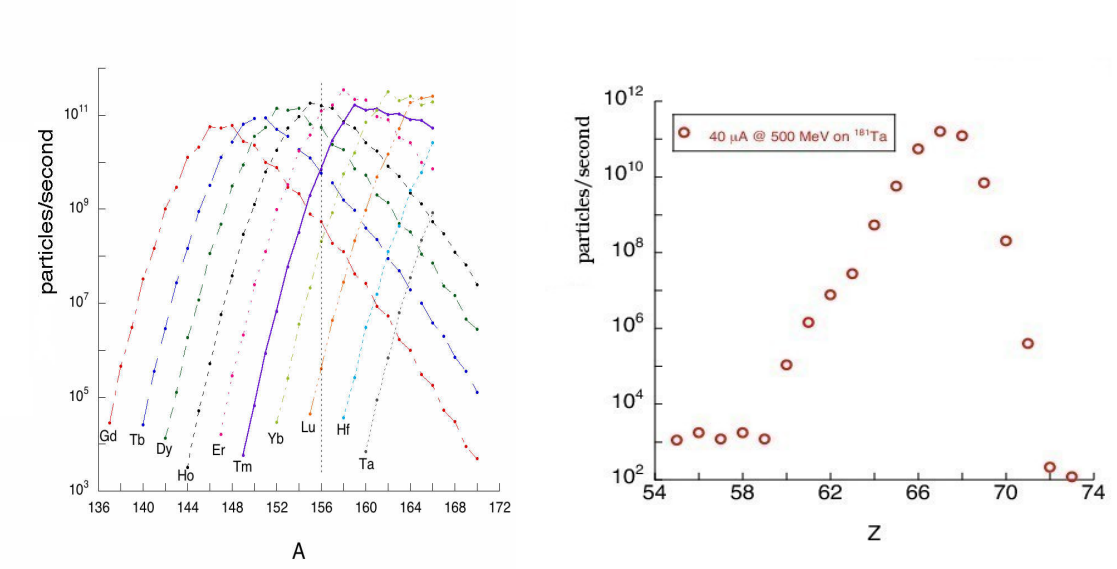

(a) Yield as a function of A

(b) Yield as a function of Z

Figure 14: The yields, atoms/s, of nuclei created through proton spallation of a tantalum target. The graph shows the results of a S-T (Silberberg-Tsao) calculation for a 40 μA beam of 500 MeV protons on a 20 g/cm^2 thick stack of Ta foils.

A FORTRAN program developed at TRIUMF uses the Silberberg-Tsao formula (Equation 27) to calculate the expected spallation yield. Figure 14 shows the expected yields of masses when a 20 g/cm^2 thick ^{181}Ta target is bombarded with a 40 μA beam of 500 MeV protons. The second exponential of Equation 27 gives the total productions for given nuclei. As the mass difference between target and product decreases, the gaussian peak moves further right, as shown in Figure 14.a. Referring to Figure 14.a, the peak of the yield curve A=156 occurs around Z=67 (Holmium), with an order of magnitude drop to $\sim 10^{10}$ particles/s at ^{156}Tm. In Figure 14.b, there are much more intense yields for other isotopes than ^{156}Tm (which is around $\sim 10^{10}$ particles/s). These more intensely produced isotopes have longer half lives and can be removed with the Moving Tape Collector (MTC). Shorter-lived, heavier isotopes are produced at much lower yields.

4.3 MTC-Moving Tape Collector

Mass-separated spallation products are deposited on 1/2-inch-wide aluminized mylar tape, shown in Figure 15, at the center of the 8π target chamber. The tape is a continuous loop, approximately 120 m long, that is moved via a stepping motor connected to a central programmable control unit. This Moving Tape Collector (MTC) provides the means to precisely set counting time and tape movement length, coordinated with beam on/off.

Periodically moving the tape and collecting new samples suppresses events from the decay of longer-lived and daughter nuclei and is a crucial aspect of spectroscopy with the 8π spectrometer. Referring to Figure 9, one sees that the decay half-lives of interest in this study range from approximately 10 seconds to over 1 hour. In order to accentuate the decays of different isotopes, the experiment was run with tape move intervals of 10.4 s, 660 s, and 105.5 minute. This study is primarily concerned with the spectroscopy of the 10.4 s tape moves which highlights the decay of the shortest-lived isotopes identified in the experiment.

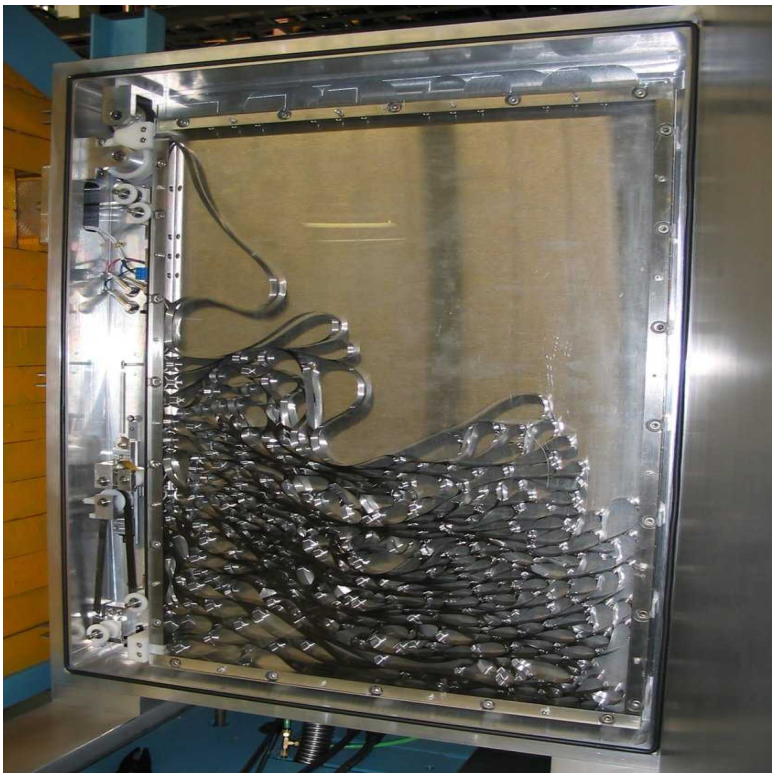

Figure 15: In this picture, the MTC is shown. After counting, activity deposits are moved out of the 8π target chamber into the MTC tape containment box. Decay products "cool" here, shielded from the spectrometer detectors by a wall of lead bricks (left). (Courtesy of David Kulp.)

4.4 8π *Spectrometer*

The γ-ray spectroscopy in this experiment was carried out using the 8π Spectrometer [37, 38, 39, 40], which is an array of 20 Compton-suppressed high-purity germanium detectors. In the following sections, a brief review of photon interactions with matter, the geometry of the 8π Spectrometer, and the process of characterizing photons with the 8π are presented. From [41], more information can be obtained on Ge detectors and photon interactions with matter.

4.4.1 Ge Semiconductor Detectors

Germanium semiconductor detectors are essentially solid-state ionization chambers. Free electrons produced through the interaction of γ rays with the Ge crystal accelerate in a high-voltage field ($\sim$3000 V) across the crystal to create electron-hole pairs. The high

voltage requires liquid nitrogen temperatures (77 K) to reduce thermal ionization noise in the detector due to the small (∼1 eV) band gap between the conduction and valence bands in germanium. Combined with high carrier mobility in the crystal, the small band gap allows for nearly complete charge collection. The result is that these detectors have excellent energy resolution and can handle very high count rates in an experiment (∼10 kHz per detector).

4.4.2 The Absorption Mechanisms in Ge Detectors

The γ rays emitted by radioactive nuclei are absorbed in a Ge detector as the photons ionize atoms in the crystal through three mechanisms. In order of importance as a function of energy, these are the photoelectric effect, Compton scattering, and pair production. In Figure 16, the interaction cross sections as a function of energy for these three mechanisms are shown. Figure 17 shows a simple illustration of these mechanisms in a germanium detector. In Figure 18 may be found the schematic of an energy peak and of the possible corresponding events in a spectrum for these three absorption mechanisms. Basic information on the interaction of electromagnetic radiation with matter is given below in the order of importance of γ-ray detection.

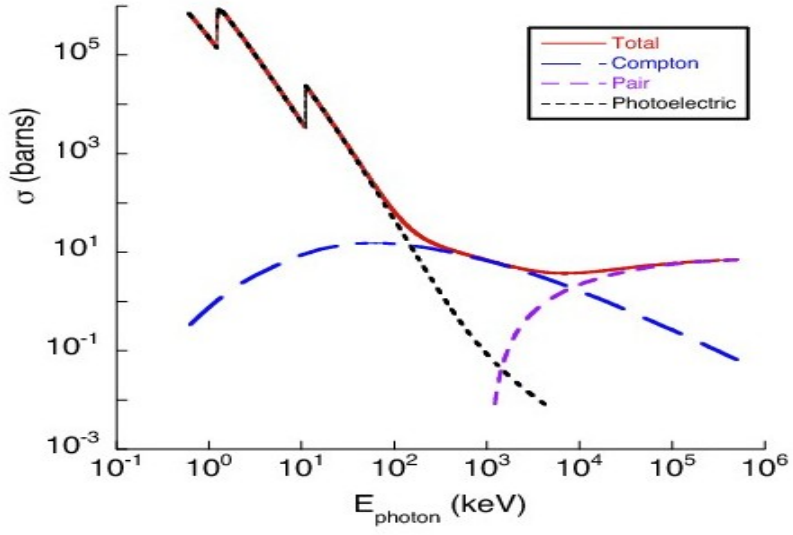

Figure 16: The interaction cross section of photoelectric effect (PE), Compton scattering (CS), and pair production (PP) are illustrated.

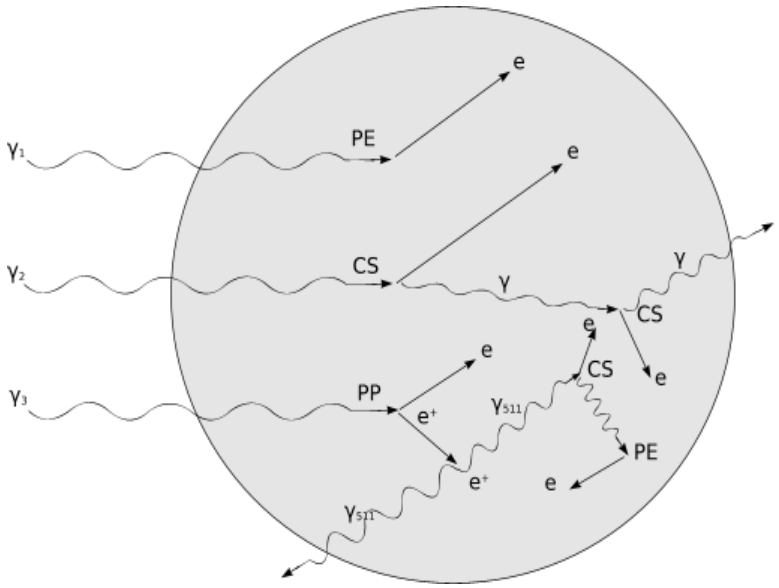

Figure 17: Interaction of γ rays in a detector. Photoelectric effect, Compton scattering and pair production mechanisms are given [41].

4.4.2.1 Photoelectric effect

The photoelectric effect is very important when the energy range is below ∼150 keV. There is a $\sim 10^6$ to $\sim 10^3$ difference in cross sections, below 100 keV between photoelectric effect and Compton scattering. The appropriate energy is found by subtraction of the electron binding energy in the detector material from the γ-ray energy ($E_e = E_\gamma - E_b$), resulting in well-defined photopeak production. The well defined photopeak for the photoelectric effect is the stand-alone photopeak at the very far right, see Figure 18. If the interaction is near the surface of the detector, it may result in a Ge escape peak ($E_e = E_\gamma - E_{K_\alpha}$). The sudden increases in the curve in Figure 16 below 100 keV are due to the binding energies of K, L or M electrons as they are ejected.

4.4.2.2 Compton scattering

In Compton scattering only a part of the γ energy is transferred ($E_e = E_\gamma - E_{\gamma'}$) to an electron in the detector. This interaction becomes important when the energy range takes the values between ∼150 keV and 7 MeV. Referring back to Figure 16, the order of magnitude difference in cross sections in this region is noticeably higher for Compton scattering. The energy range of Compton scattering is the most important one because the

energies carried by most γ rays fall into this range. A Compton scattering event may be followed by another Compton scattering event, see Figure 17, and eventually an escaped γ ray. Scattering angle dependence results in a Compton continuum in the energy spectrum. At the angle $\theta = 180°$, a Compton "edge" occurs, and a Compton backscatter peak, see Figure 18, may be seen at $\sim$200 keV, which is caused by other material nearby to the detector.

4.4.2.3 Pair production

In pair production, an electron-positron pair is created near the atom ($E_e = E_\gamma - 1022$). The threshold of γ-ray energy for this process is 1022 keV, since the total mass of electron and positron is 1022 keV. Positron annihilation results in two more γ-rays at 511 keV. In the spectrum a SEP (single escape peak) occurs when one of the 511 keV photons escapes the detector, and a DEP (double escape peak), see Figure 18, for schematic representation, occurs when both of the 511 keV photons escape the detector.

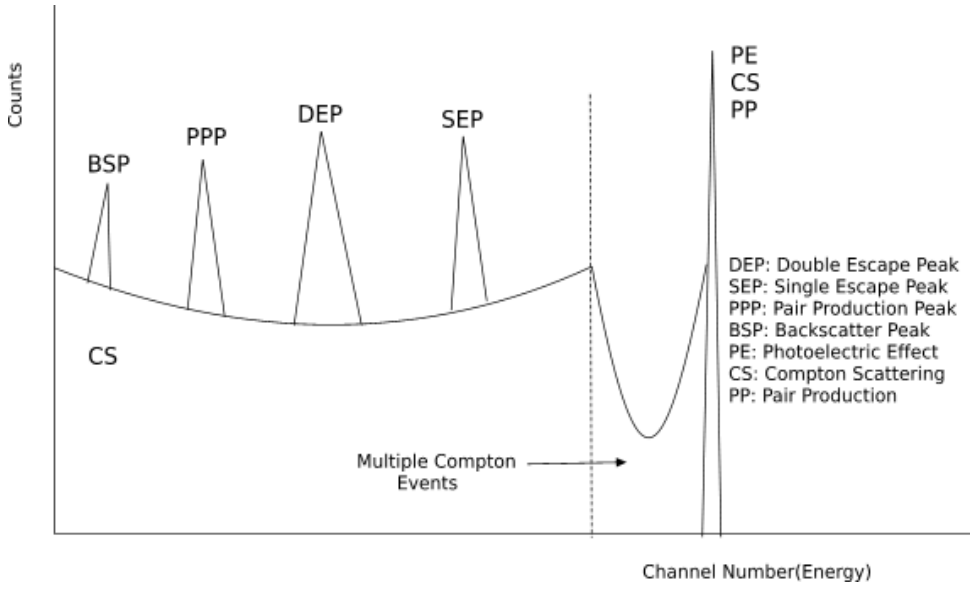

Figure 18: The schematic of typical components of an energy spectrum in γ-ray spectrometry: full energy double- and single-escape peaks, annihilation peak, Compton backscatter and Compton continuum [41].

4.5 Structure of 8π

The 20 coaxial high-purity germanium detectors (HPGe) are installed in a truncated icosahedral shape very similar to a soccer ball with 20 hexagonal and 12 pentagonal faces. This geometry inspired the name "8π" because the spectrometer previously had a concentric sphere of BGO scintillators inside the Ge detector array. To increase the efficiency, the inner BGO ball was removed and the HPGe detectors moved closer to the center. The distance from the source to each detector is 14 cm in the present configuration.

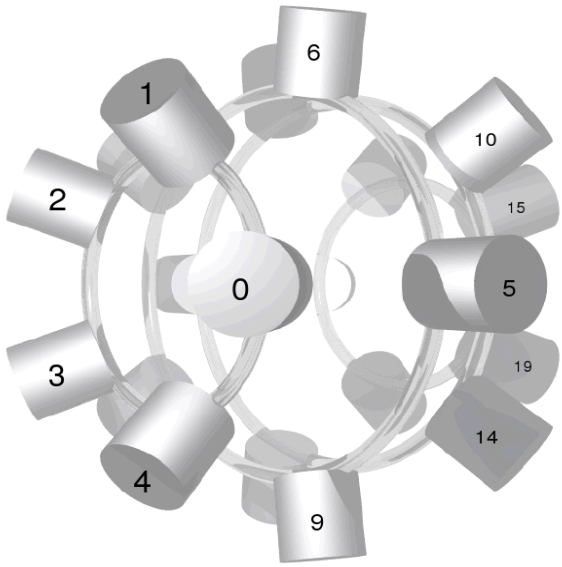

Figure 19: Geometrical distribution of the detectors in the 8π. Detectors are placed around 4 rings. Each ring involves 5 detectors ranging over positions 0-4, 5-9, 10-14, 15-19, respectively. (Courtesy of Paul Schmelzenbach.)

Icosahedral symmetry results in a pairing of the detectors. Detectors form 4 rings along with 5 angles: 30 pairs with 41.8^o, 60 pairs with 70.5^o, 60 pairs with 109.5^o, 30 pairs with 138.2^o, and 10 pairs with 180.0^o [42]. Figure 19 shows the placement of the detectors in 4 rings accordingly. The volume of each detector is approximately 115 cm^3 with a corresponding 5.2 cm diameter of its cylindrical shape. Compared with a standard NaI scintillator crystal, each Ge detector has a relative efficiency of 25%. The absolute total efficiency of the spectrometer is 1.5%.

4.5.1 BGO Shielding

High-efficiency BGO scintillator shields are mounted coaxially around each Ge detector to suppress the Compton background continuum. When Compton-scattered photons leave the Ge detector volume a continuous background results, producing "noise" that reduces the peak-to-total ratio (P/T). Suppressing this background reduces detector dead time (the time required to process each event in the electronics) and improves the ability to see weak transitions which would ordinarily be lost in the background.

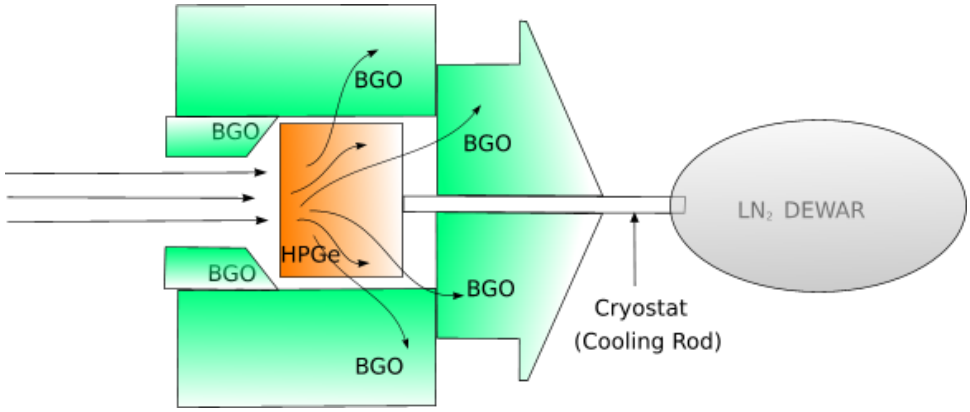

Figure 20: Basic photon interactions with a Ge detector in a Compton-suppressed arrangement. Photons incident on the Ge detector lead to voltage pulses which are routed to subsequent electronics which digitize and sort the pulses. BGO scintillation detectors capture the Compton-scattered photons. The related electronics eventually veto the Compton scattered photons. The figure is reproduced using the similar figure in reference [43].

Using fast electronic logic circuits, this continuum is reduced by rejecting events in which a Ge detector and its BGO shield detect photons. Timing signals from the BGO suppression shields, see Figure 20, are compared with timing signals from the Ge detector to suppress the Compton background continuum. In the electronic logic, the timing signals of the Ge detectors and BGO shields are compared to determine if they fall in a predetermined time window or not. If the Ge detector and BGO shield have simultaneous time signals, the result is not written out to disk.

A P/T=0.477 for the 677 keV line of ^{137}Cs was measured for this experiment. The resolution in this experiment is 2.5 keV FWHM for the 1.332 MeV line of ^{60}Co.

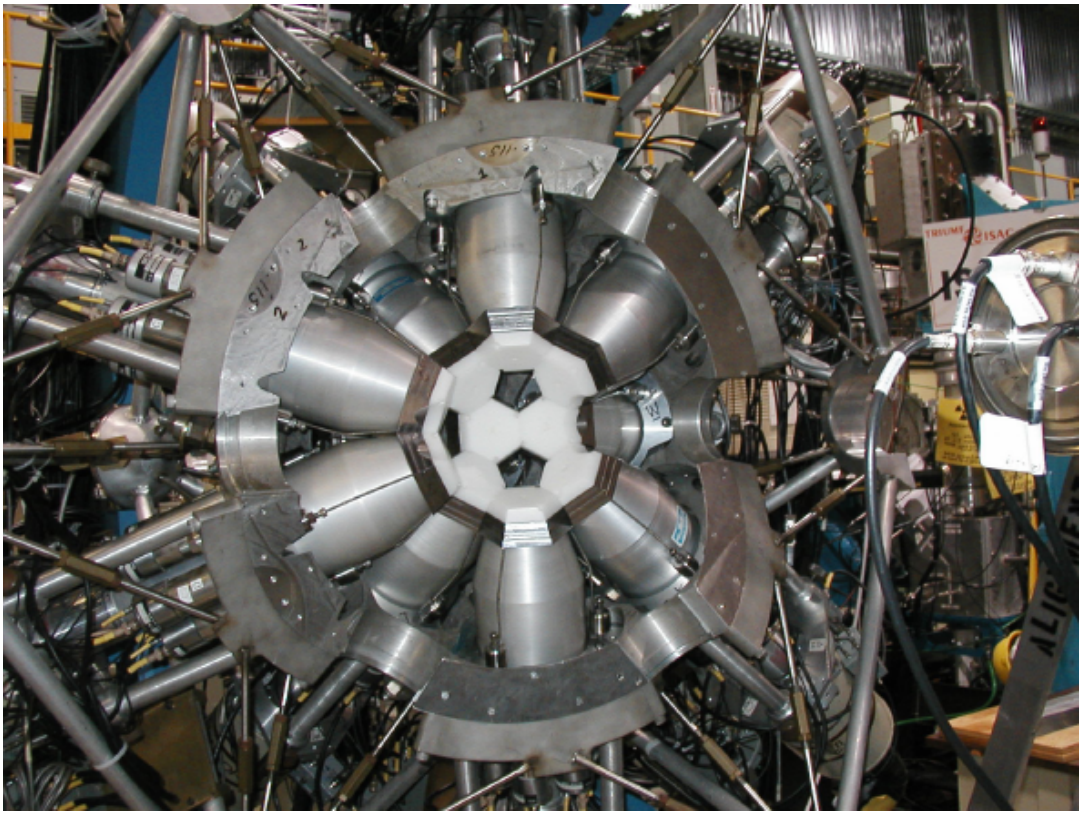

Figure 21: Picture of the 8π detector array system. The figure is taken from [44].

CHAPTER V

DATA FLOW (RUNNING, SORTING, ANALYZING)

The data flow for the experiment can be split into 3 parts: the process of writing the data to disk during the experimental run, sorting the data into a γ-ray coincidence matrix, and analyzing the resulting γ-ray coincidence spectra. Figure 22 illustrates the individual steps in these three sections. After processing nearly 1 terabyte of data written to disk, $\sim 1.3 \times 10^8$, γ-γ coincidence events were analyzed in this study.

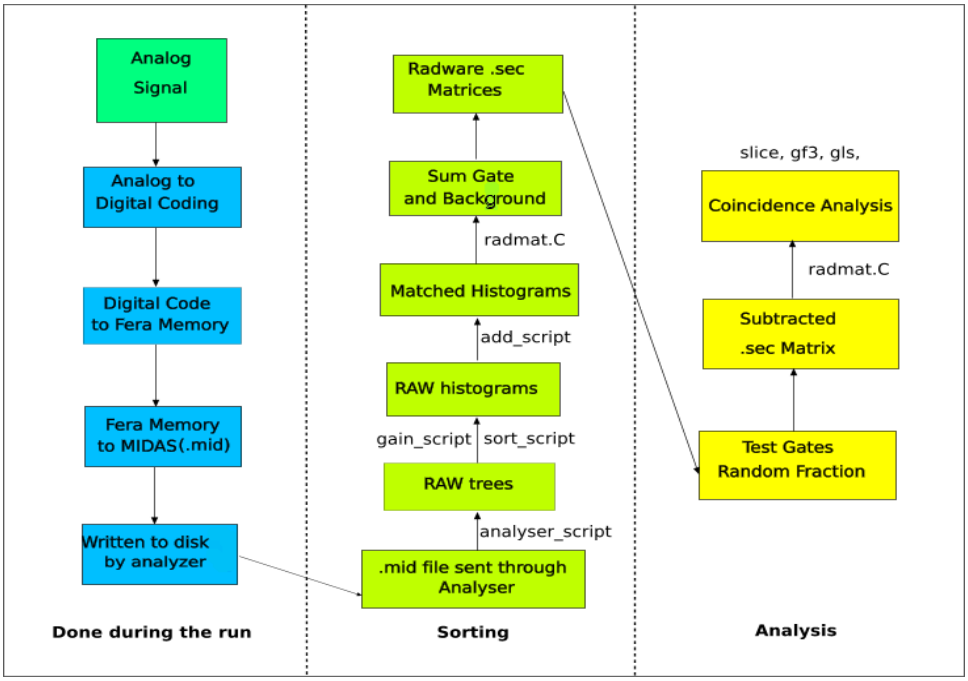

Figure 22: The data management of our study is shown. The first column was done during the run of the experiment. The second column is mainly the sort process of the data. The third column is the analysis.

5.1 Coincidence Events

Events occurring within the resolving time may be related to each other. Gamma transitions occur in a very short time (they are usually on the order of nanoseconds). When two or more γ rays immediately follow or precede each other in a γ-ray cascade, it can

be said that they are in coincidence, and they occur in the very short time window. The weak transitions which cannot be seen in the γ-ray singles spectrum can be identified with greater sensitivity in coincidence spectrometry. Coincidence events [45] are also measured to obtain more accurate intensities compared with single measurements .

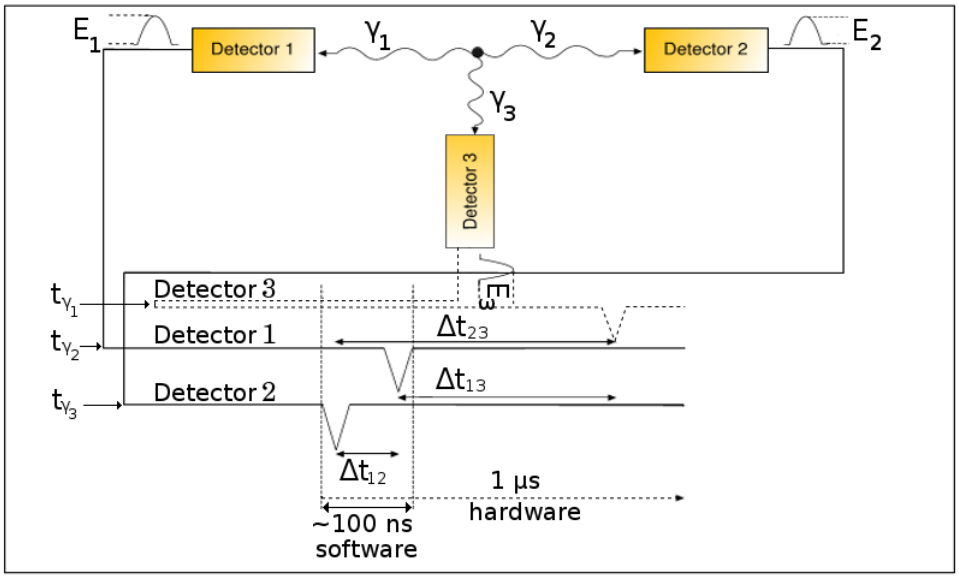

Figure 23: Data acquisition through the coincidence data collection method. The signals from all detectors are within the set time window inferring that they are in coincidence.

Coincidence events are collected if two or more γ rays occur within a set time window. This is schematically illustrated in Figure 23, where three γ rays are detected in a 1 μs coincidence window. Each detector produces a signal which carries energy (E_γ) and time (t_γ) information. An ADC (Analog to Digital Converter) converts these signals to a digital channel number for analysis. A TDC (Time Digital Converter) is used to record the time of the detector signal. A signal from detector 2 starts the 1 μs comparison window. If signals from other detectors are within the hardware window of 1 μs, information from all detectors are written to disk as a coincidence event.

Using software, a shorter time gate can be set to better distinguish between true and random coincidences. In Figure 23, a window of ~100 ns separates γ_{12} from γ_3. The γ_{12} event can be considered a true coincidence event. Events γ_{13} and γ_{23} are random

coincidences. By constructing coincidence matrices, one with true (prompt) coincidences and the other with random (delayed) coincidences, the effects of random coincidences in the data stream can be reduced. (This will be discussed in detail in section 5.2.1).

5.2 Data Sorting

Experimental data were written to disk using software developed at TRIUMF using MIDAS (Maximum Integrated Data Acquisition System). For further information on MIDAS, reference [46] is useful. The timing and energy information were written out as MIDAS formatted events. In this format, the events are stored as blocks read from hardware (FERA) memory. Each block indicates the event length, the event time, and so on to assist further analysis. The data written to disk were modified through this analysis and formatted as MIDAS (.mid) files.

Offline, a modified analyzer (batch-processed using *analyser_script*) was used to decode the MIDAS-formatted data and to reorganize the events for further processing. The output from this was written in a format readable by ROOT [47], an object oriented environment for data analysis. It has functions to create 1-dimensional (spectra) and 2-dimensional (matrices) histograms for data. ROOT stores data in a "tree" format. This allows for rapid isolation of event parameters, such as E_γ or t_γ for calibration purposes.

Electronic jitter, delays in the electronic circuits, cable lengths, etc., can result in timing differences between detectors. A suitable timing offset for each detector was determined by comparing raw time spectra for each detector. Consistent time differences between pairs of γ rays in an event were then determined for coincidence time analysis.

Detector amplifier gains may drift during the course of the experiment. Calibration was performed through *gain_script*, a program using ROOT functions. Detector gains were matched using strong reference peaks in the raw energy spectra so that all detectors line up in order to create the correct summed spectrum.

Gain-matched and time-corrected data for each run were written as 1-dimensional spectra and 2-dimensional matrices using the *sort_script* software developed at Georgia Tech. The computer code, *add_script*, creates summed histograms from the individual run files.

5.2.1 Prompt and Delayed Matrices

A source with a higher activity increases the rate of γ-ray emission, thus increasing the chances of detecting γ-γ coincidences and weak γ-decay branches. However, a more active source also increases the rate of detecting uncorrelated (random) coincidence events. The ratio of random (accidental) coincidences to prompt (true) coincidences is proportional with the set time window and the source activity [48]. The corresponding equation is

$$\frac{N_{random}}{N_{true}} = 2\tau N_0 \tag{28}$$

where 2τ is the set time window, and N_0 is the source activity.

A hardware time interval of $2\tau = 1\mu$s was used to trigger the 8π data acquisition and write the event to disk. An interval of 10^{-6} s may seem very short; but, when compared with nuclear level lifetimes that can be femtoseconds (10^{-15} s) in duration, this is a very long time. This long coincidence window was used to reduce the effect of random coincidences by defining two complementary subsets of the data.

The two complementary sets of data represent prompt and delayed coincidence events. A schematic histogram of time differences, as shown in Figure 24, indicates how this information was used to construct the prompt and delayed matrices. Small Δt values, i.e., Δt_{12} occurs in $\sim$100 ns region, see Figure 23, and large Δt values, i.e., Δt_{13}, and Δt_{23} can be readily separated. The whole matrix was then written out as symmetric E_γ-E_γ matrix forms. The upper matrix (the prompt matrix-($E_{\gamma 1}$ vs. $E_{\gamma 2}$)) was formed using the Δt_{12} time interval, and the lower matrix (the delayed matrix-($E_{\gamma 1}$ vs. $E_{\gamma 2}$)) was formed using the Δt_{13} and Δt_{23} time intervals.

To construct a γ-γ coincidence projection matrix in a high count rate experiment involves properly accounting for random coincidences. In this work, a delayed coincidence matrix

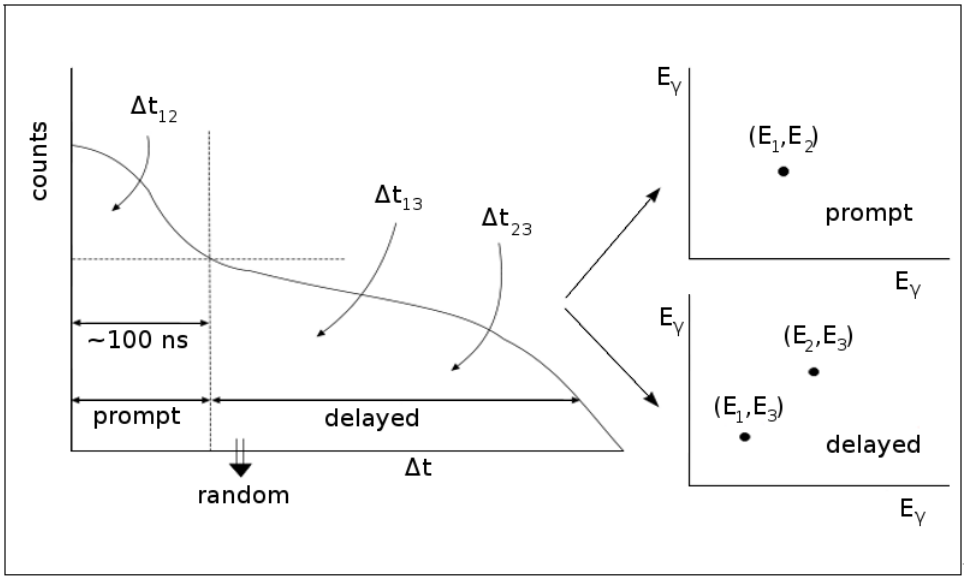

Figure 24: The schematic representation of the formation of prompt and delayed matrices and the writing of results into the E_γ-E_γ matrix. The events in the Δt_{12} time represents prompt (true) events, and in the Δt_{13} and Δt_{23} times are delayed (random) events. One axis in the energy matrix represents the γ-ray energy in detector 1, the other one the γ-ray energy in detector 2.

was scaled with an appropriate factor and subtracted from the prompt matrix [49, 50]. A ∼100 ns prompt coincidence time gate was used to remove the considerable amount of random coincidences.

Figure 25 shows the prompt and the delayed matrix projections of our data. The number of counts in the 115 keV line (strongest γ ray of ^{156}Tm) in the prompt matrix projection is $\sim 2{\times}10^6$, on the other hand it is $\sim 8 \times 10^6$ in the delayed matrix projection. The different number of counts in the prompt and delayed matrix projections exhibit the necessity of scaling the delayed matrix and subtracting it from the prompt matrix.

One of the strong lines in ^{156}Er is a 344 keV line, and in ^{156}Tm there is a strong 115 keV line. In Figures 26 and 27, the gated spectra of these two energies are shown. Since the 115 keV and 344 keV lines belong to different nuclei, it is expected that the 115 keV line should not be seen in the 344 keV γ-ray gated spectrum, or vice versa. However, the coincidences in the Figures 26 and 27 show the rate of random coincidences. It is also expected that

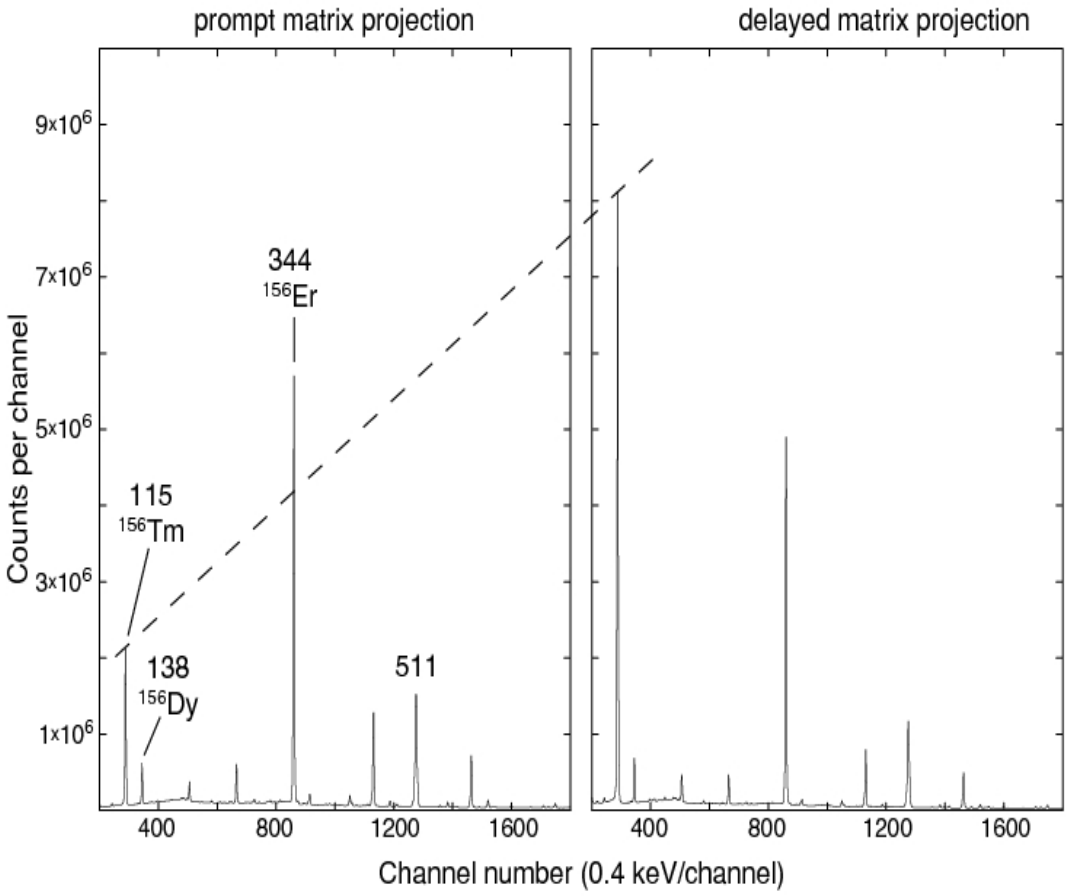

Figure 25: The prompt and delayed matrix projections of the data. The high counts of 115 keV line in the delayed matrix projection is very notable showing the necessity of scaling the delayed matrix.

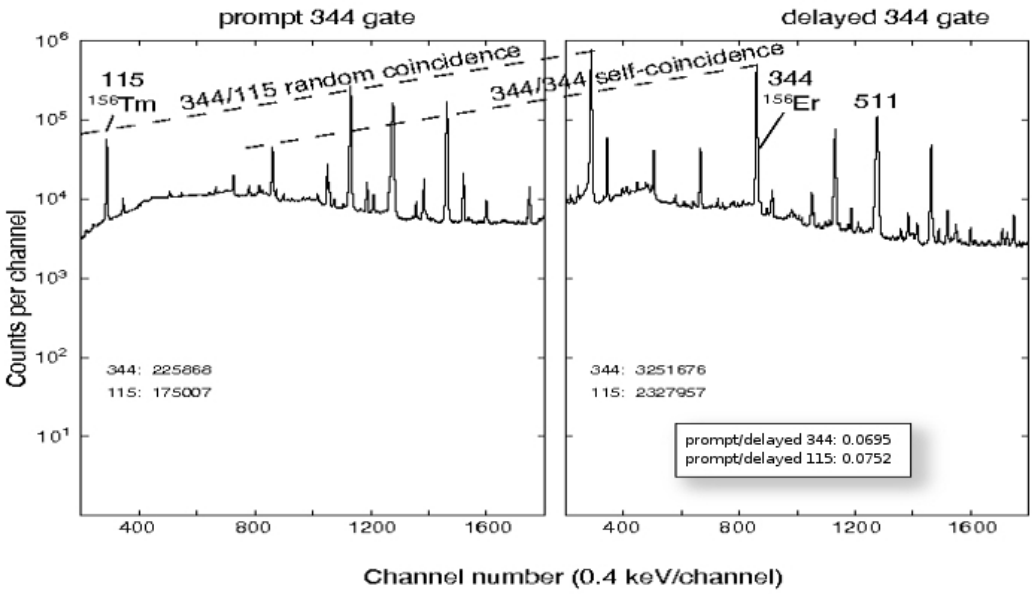

Figure 26: The prompt and delayed matrix projections of the data for the 344 keV gate. The large number of the counts in the delayed 344 keV gate is very notable. The prompt/delayed count rate appeared to be ∼7 %.

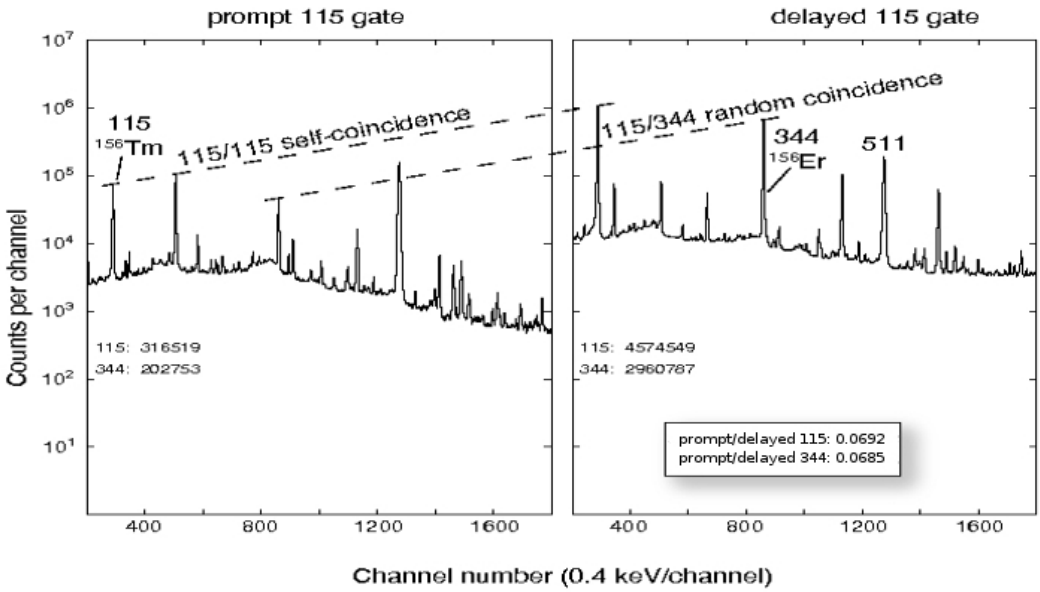

Figure 27: The prompt and delayed matrix projections of the data for the 115 keV gate. The prompt/delayed count rate appeared to be ∼7 %.

the 344 keV and 115 keV lines should not be seen in the gates themselves, yet the self coincidences appear in the same figures. The self coincidences of the 344 keV line in the 344 keV gated spectrum and the 115 keV line in the 115 keV gated spectrum, the random coincidences of the 344 keV line in the 115 keV gated spectrum and the 115 keV line in the 344 keV gated spectrum are considerably less in the prompt matrix projection than in the delayed matrix projection. The delayed/prompt ratio for the 344 keV line in the 344 keV gated spectrum and the 115 keV line in the 344 keV gated spectrum were calculated to be 0.0792 and 0.0695, respectively. The delayed/prompt ratio for the 115 keV line in the 115 keV gated spectrum and the 344 keV line in the 115 keV gated spectrum were calculated to be 0.0692 and 0.0685, respectively. To reduce the unwanted random coincidences, the delayed matrix was multiplied with the ∼7 % ratio and then subtracted from the prompt matrix to obtain the final corrected projection spectrum.

5.3 Coincidence Spectrum

A full range of (channels from 0 to 8192∼3276 keV full-range) of the coincidence spectrum (one channel is equal to 0.4 keV) is shown in Figure 28. The spectrum counts are displayed in a logarithmic scale for first 2000 channels to show the complexity as well as the high statistics of the data set. The spectrum involves not only the γ lines of ^{156}Er, but also the lines of ^{156}Tm and ^{156}Dy because they are the decay daughters of ^{158}Yb (see Figure 9). The strong peaks for ^{156}Er (e.g., 345, 453, 586, 959, 1007 and 1286 keV), for ^{156}Tm (e.g., 115, 203 keV), and for ^{156}Dy (e.g., 138, 266 keV) are shown along with the K_α and K_β X-rays for ^{156}Er and the annihilation peak (511 keV).

It is necessary to separate the γ rays of ^{156}Er from those which belong to different nuclei, i.e., ^{156}Dy and ^{156}Tm. The transitions of ^{156}Dy are rather well-known, so there was not made any attempt to resolve ^{156}Dy data. Some of the γ rays belonging to ^{156}Dy were seen in the pulled gates of γ rays belonging to ^{156}Er. When a γ ray was seen in the pulled gates of ^{156}Er, it was compared with the adopted scheme [1] to decide whether it is a γ ray belonging to ^{156}Er or to ^{156}Dy.

However, the lack of known γ rays in ^{156}Tm complicated the analysis for ^{156}Er. It was decided that as full an assignment of γ rays to ^{156}Tm was required. The nucleus ^{156}Tm is an odd-odd nuclei. To build a decay scheme for an odd nucleus is rather difficult using only γ-γ coincidences, without e-γ data. Internally-converted transitions are common for odd-odd nuclei, and it was noticed that some gaps between γ ray cascades occurred. Even though a γ-γ coincidence decay scheme was constucted for ^{156}Tm during the analysis, it was used for reference purposes only to identify the γ rays of ^{156}Er in the projection spectrum.

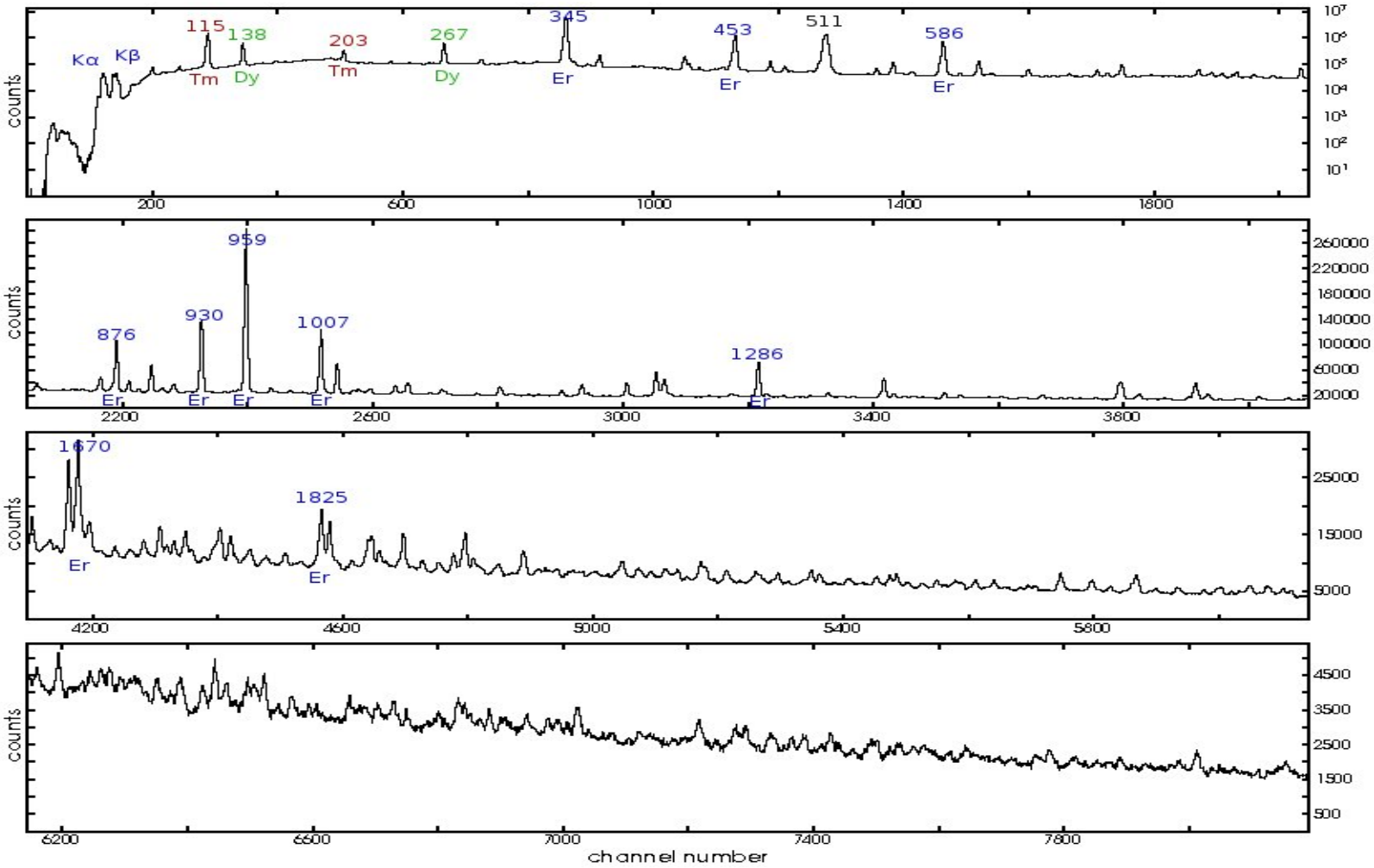

Figure 28: The projection spectrum of the γ-γ coincidence matrix. The spectrum involves transitions in ^{156}Tm, ^{156}Dy, and ^{156}Er. A logarithmic scale is preferred for channels 0-2000, and a linear scale is preferred for the rest of the spectrum.

5.4 Calibrations and Data Analysis

Because the data set has a high number of coincidence events, ($\sim 1.3 \times 10^8$ γ-γ events), a very detailed coincidence analysis could be carried out. Coincidence spectra were generated from the random-coincidence subtracted γ-γ matrix and subsequently fitted using the computer software package written by Radford [51] for Linux. The Radware program *gf3* was used to display spectra for analysis and fit the γ-ray peaks. Selected regions of the coincidence matrix were extracted and combined to form energy-gated coincidence spectra with the program *slice*. Details of these programs and the procedures used for calibration and analysis will be discussed in the following sections.

5.4.1 Peak Fitting

The *gf3* peak-fitting routine was used to fit every peak in the spectrum analyzed. The fitting routine of gf3 has the functional form of a statistical gaussian distribution with three components, e.g., a gaussian peak, a skewed gaussian peak and a smoothed step function [52]. The gaussian component represents the photopeak from the total charge collection of the full energy of the γ ray. The skewed gaussian on the low-energy side of the peak is used to fit the "tail" due to incomplete charge collection. The smoothed step function emerges due to the scattering of photons.

As the channel number increases, the expectancy is that the peak widths increase in a smooth way. The FWHM (Full Width at Half Maximum) is parameterized in *gf3* using the following equation

$$FWHM = \sqrt{F^2 + G^2 x + H^2 x^2} \tag{29}$$

where x=(channel number)/1000, and F, G, and H are the coefficients of the quadratic equation.

Multiple peaks were fitted with varied widths to arrive at self-consistent peak width parameters. In the final analysis of the data, a fixed set of parameters was used to provide a consistent analysis of the data. The coefficients of the peak width parameters were

determined to be $F = 3.43$, $H = 2.36$, $G = 0.47$. Starting parameters for the skewed Gaussian tail, step function, and background parameters were also determined in a self-consistent way. However, these initial values were allowed to vary at times to provide a better peak fit.

The sophistication of the peak-fitting routine is illustrated in Figure 29. The 1660-1680 keV region of the 345 keV γ-ray gated spectrum contains seven γ-ray transitions in the decay.

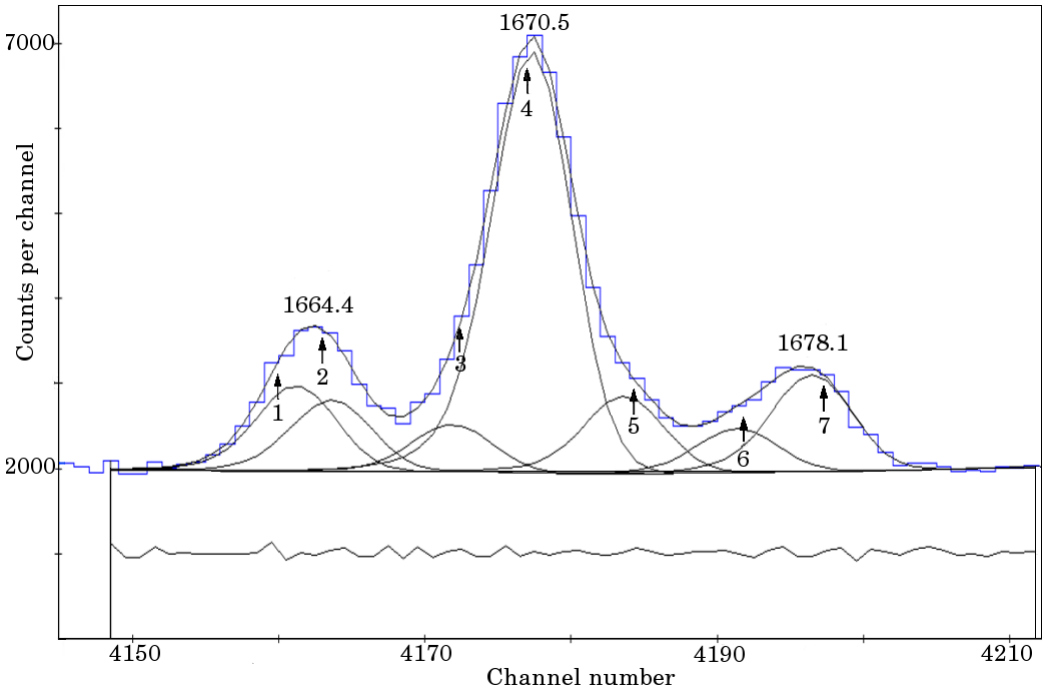

Figure 29: The fit of a multiplet in the 345 keV gated spectrum in *gf3*.

The individual peaks, the summed fit, and the residual counts compared with the data are displayed for visual comparison in *gf3*. Peak centroids and widths, and the uncertainties in these values are saved to disk by the program for further analysis.

5.4.2 Energy (Calibration and Analysis)

Before the experiment, the well known energies of γ rays emitted during the β decay of ^{60}Co and ^{207}Bi were used to set the detector amplifier gains. During the offline sorting,

the centroids (position/energy) of strong peaks in the spectra were compared with the adopted values of transitions in ^{156}Dy and ^{156}Er [1]. A linear calibration of 0.4 keV/channel was determined to provide the best resolution which allowed the full energy range for all detectors.

A more detailed calibration was performed during the analysis, using the strong transitions of adopted energies in [1]. A linear fit to the known energies of 34 lines, shown in the Figure 30, indicates that a 0.4 keV/channel calibration works well. However, the plotted differences with adopted energies, shown in Figure 31 indicates that there are nonlinear effects in the amplifier gains which must be addressed.

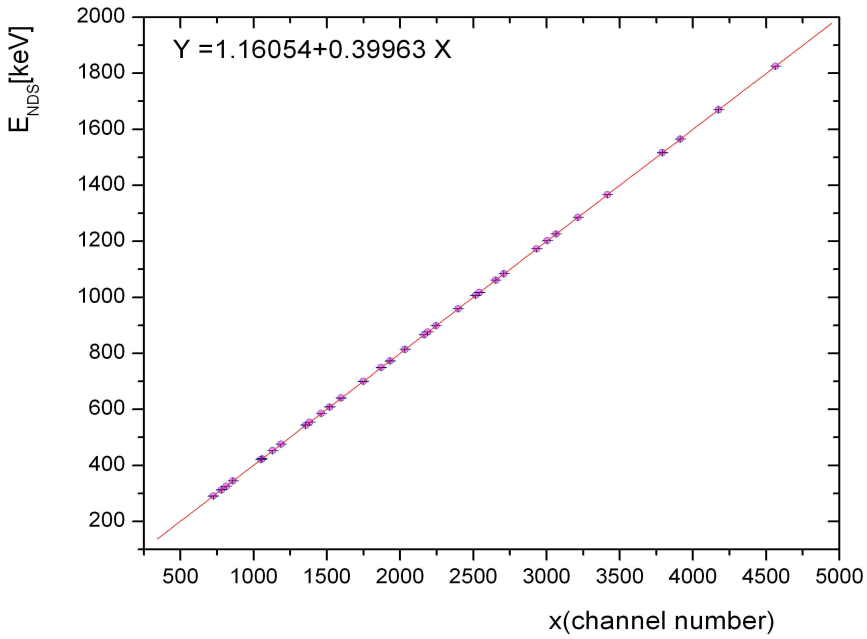

Figure 30: The linear correction of the data set. The NDS adopted energy data were used as a reference to extract the linear parameters.

The polynomial third-order least-squares fit of energy differences, shown in the Figure 31, is the lowest-order correction for the deduced energies in the exhibited energy range. The error bars of the difference of newly measured and existing γ-ray energies are shown. Only

a few of the error bars lie outside of the graph. This third-order correction was added to the linear calibration to calculate the peak energies below ∼1800 keV. Due to the lack of known energies in the literature [1] above 1800 keV (see Figure 31), only the linear calibration was used for this range.

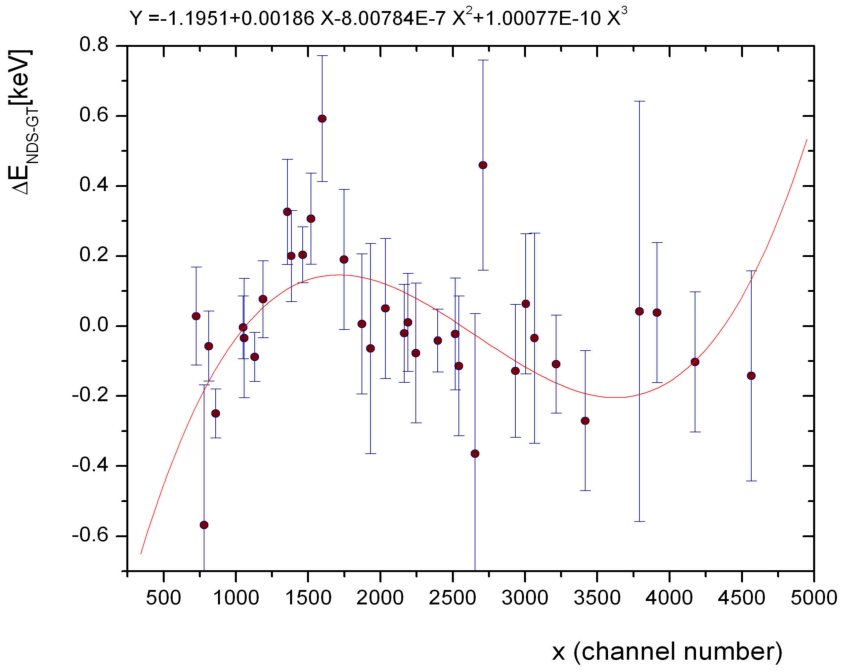

Figure 31: The plot of energy difference vs. channel number. The set of third-order polynomial parameters was calculated with the least squares fit.

5.4.2.1 The Uncertainty of the Energies

The measured energies of γ-ray transitions with energies $\leq$1800 keV were compared with the adopted values [1]. Differences between calculated and adopted energies are plotted in Figure 32. The systematic error (the energy separation between measured and adopted values as a function of measured energy) was deduced to be 0.14 keV for this region.

The systematic error for γ-ray transitions with energies $\gtrsim$1800 keV was calculated using both the Ritz combinations of the γ rays originating from the level and the energy of the ground state γ ray transition. The level energy (calculated using the Ritz combinations

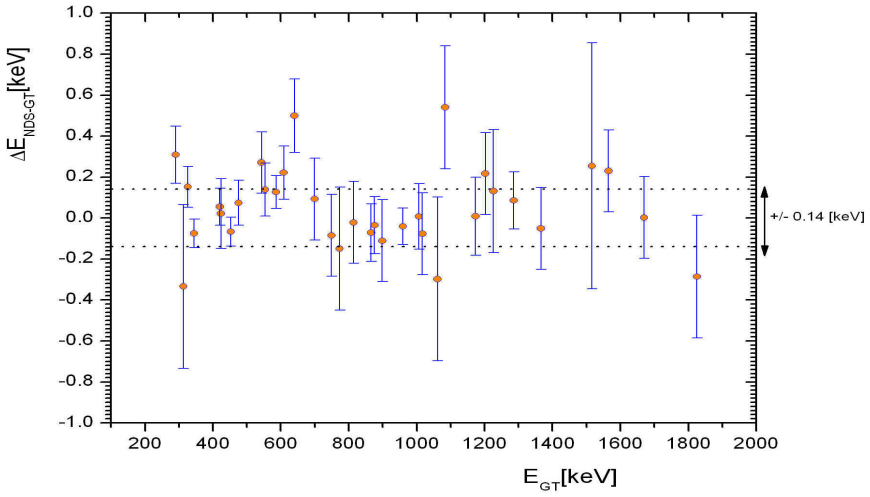

Figure 32: The plot of the measured energy vs. the difference between the measured energies (after the polynomial correction) and the adopted energies. The systematic error of the data set below 1800 keV is shown in the Figure.

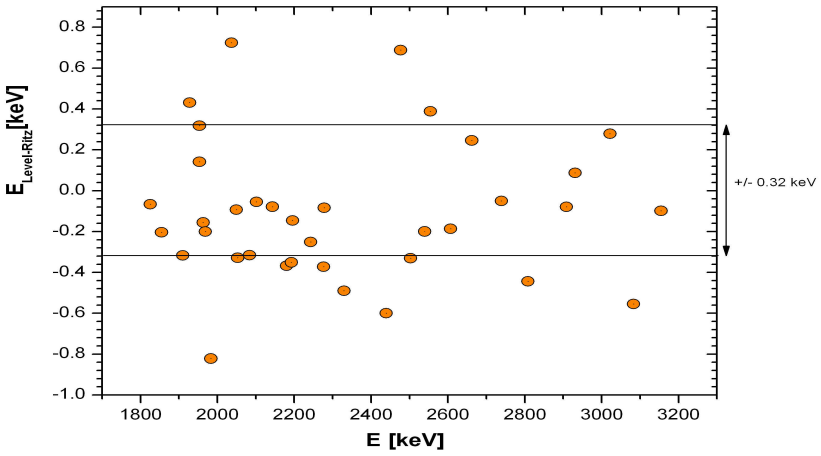

Figure 33: The plot of the difference between the level energies (calculated using the Ritz combinations of γ rays of $\leq$1800 keV) and the linearly-corrected energies of transitions $\gtrsim$1800 keV vs. the γ-ray energy. The systematic error of the data set above 1800 keV is shown.

of γ rays with energies $\leq$1800 keV) was subtracted from the linearly corrected energies for transitions $\gtrsim$1800 keV. This energy separation was plotted as a function of linearly corrected γ-ray energies as shown in Figure 33. The systematic error for this region was deduced to be 0.32 keV. The fit error of centroids, the weighted errors of Ritz combinations, and systematic errors were added to obtain the total uncertainty for all γ-ray transitions.

5.4.3 Efficiency Calibration

Gamma-ray intensity, I_γ, is one of the important experimental results of γ-ray spectrometry. The intensity of a γ ray is a measure of the probability of the transition between two nuclear states. The intensities of γ-rays can simply be calculated using the formula

$$I_\gamma = \frac{A_\gamma}{\epsilon_\gamma} \tag{30}$$

where A_γ is the fitted area of a γ ray, and ϵ_γ is the calculated efficiency of the corresponding peak.

The relative detection efficiency of a γ ray in a single Ge detector is a function of the energy of the transition. If the relative efficiency curve is known, then γ-ray intensities can be calculated from fitted peak areas using Equation 30. However, in complex spectra such as encountered in this study (see Figure 28) singles measurements cannot sufficiently resolve individual peaks and weak transitions. Weak transitions are difficult to observe in singles. Instead, coincidence spectroscopy must be used to properly determine γ-ray intensity and transition placement in the level scheme.

An iterative method developed by Kulp [49, 50] was followed to determine the coincidence efficiencies in this study. This method is based on a relation similar to Equation 30 which accounts for the detection of a cascade of γ-ray transitions in a nucleus. The equation [45],

$$A = \Omega I_{\gamma_1} \epsilon_{\gamma_1} B_{\gamma_2} \epsilon_{\gamma_2} \tag{31}$$

relates the fitted peak area, A, to Ω, a normalization constant for the whole data set; $I_{\gamma 1}$, the intensity of the feeding γ ray; ϵ_1 and ϵ_2, the detector efficiencies for corresponding energies; and $B_{\gamma 2}$, the branching ratio for the draining γ ray.

The primary step in the efficiency calibration is to calculate a common value of Ω (see Equation 31) for whole data set. The strong peaks feeding the 345, 798 and 930 keV levels were chosen to see the first response of Ω. Two of these levels (345 and 798 keV) have only a single γ-ray transition depopulating the level, simplifying Equation 31, because $B_\gamma \sim 1$ for these draining transitions.

For the draining transitions (γ_2 in Equation 31), the branching ratio was calculated using

$$B_\gamma = \frac{I_\gamma}{\sum_i (1+\alpha) I_{\gamma i}} \tag{32}$$

where I_γ is the intensity, and α is the internal conversion coefficient for each transition. The values 0.046, 0.0214, and ~0.0112 in reference [1] were used for the 345, 453, and 586 keV transitions depopulating the 345, 798, and 930 keV levels, respectively. The adopted intensities for strong γ rays feeding the 345, 453, and 586 keV transitions were then used to determine the $\epsilon_{\gamma 1}$ and $\epsilon_{\gamma 2}$ values at the corresponding energies.

Complementary gated spectra for each of the strong peaks were also measured to verify A (area), the coincidence peak counts by measuring the areas of the 345, 453, and 586 keV γ rays in the strong peak gates. An energy vs. normalization constant (Ω) plot, Figure 34, shows the result of the first iteration. The different lines represent a self-consistently fitted peak, and single normalization constant for each depopulating transition.

Using adopted energies of the strong populating transitions (γ_1) and the tabulated branching fractions [1] of the corresponding depopulating transitions (γ_2), a first $log(\epsilon_\gamma)$ vs. $log(E_\gamma)$ plot was made. The parameters of the 4th order polynomial fit to these data were used to determine the new set of coincidence efficiency values as a function of energy. These new efficiency (ϵ_γ) values were then used in subsequent iterations for determining new average Ω values, and new $log(\epsilon_\gamma)$ values.

By conducting this process iteratively, a self-consistent coincidence efficiency curve was formed, see Figure 35. The parameters of this curve and the final average value of the normalization constant (Ω) were used to calcuate the relative intensities of the γ rays. During

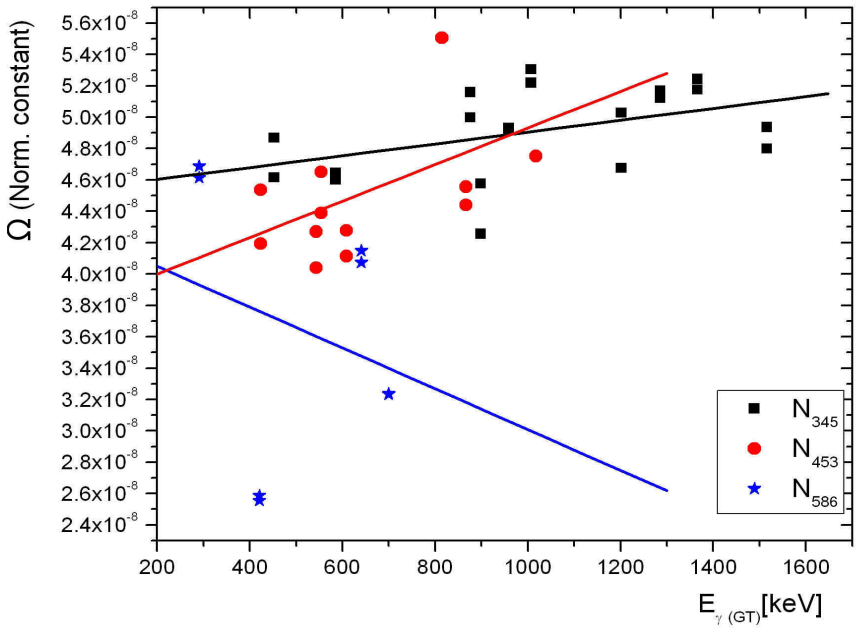

Figure 34: The systematics of the normalization constant for different gates. Strong peaks were chosen in the 345, 453, and 586 keV gates. For each gate, a different normalization line was produced showing that the necessity of a self-consistent one smooth line.

the iterative process, multiplets and transitions which are close in energy to transitions of other nuclei in the source were removed from the analysis.

Since ^{156}Er does not have strong peaks in the low-energy region, a few of the strong peaks in ^{156}Dy and ^{156}Tm were used to determine the response of the efficiency curve in the low-energy region. These data were appropriately scaled to the ^{156}Er data to achieve the 4th order polynomial fit of $log(\epsilon_\gamma)$ as a function of $log(E_\gamma)$ shown in Figure 35.

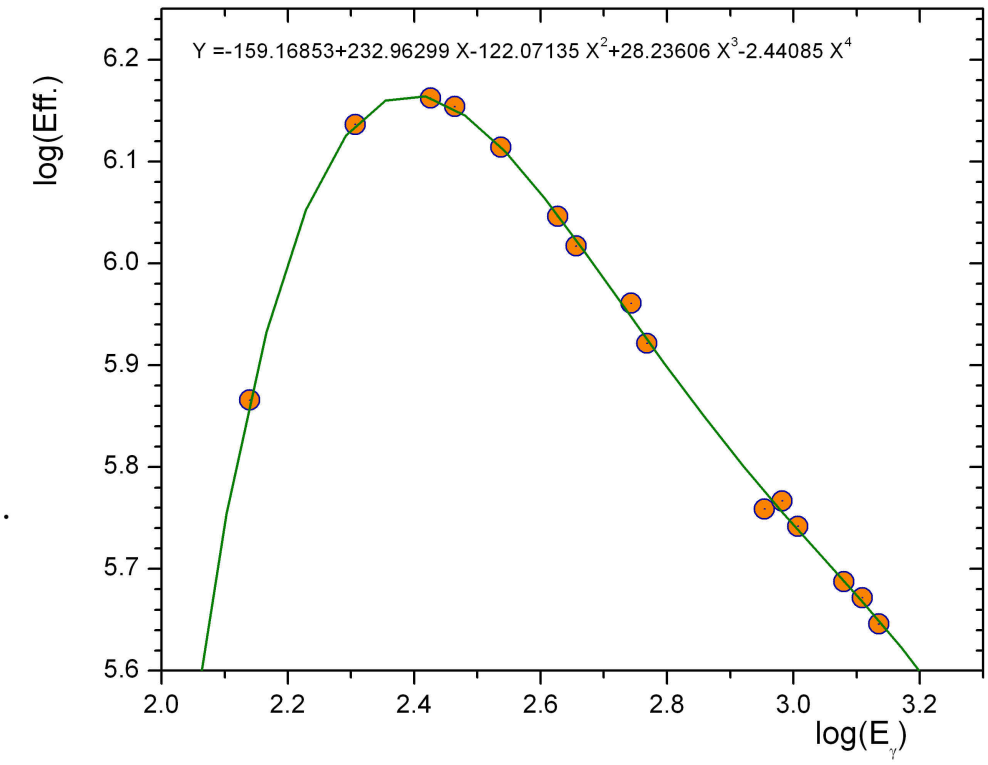

Figure 35: The 4^{th} order polynomial efficiency curve for the coincidence data. The final parameters are placed on the plot.

5.5 Levels and γ-Ray Placement

Coincidence spectroscopy techniques were used to determine the placement of γ rays in between the levels of ^{156}Er. Every possible gate corresponding to a peak in the coincidence projection spectrum was pulled. In each gate, every γ ray was analyzed to construct the decay scheme.

5.5.1 Coincidence Gates

The observed spectrum constructed from summing channels extracted from the γ-γ matrix in a selected range (gated) is commonly called a "gated" spectrum. "Pulling a gate" means determining the γ ray, peak region, and the corresponding background region in the projection spectrum using *gf3*, creating a γ-gated spectrum from this projection spectrum using *slice*, and subtracting the suitably of a scaled background spectrum. In this process, a suitable channel range for the peak is chosen; and preferably, at the left and right of this peak, a suitable background at equal width in sum to the peak slice is chosen to run them in *slice*, as shown in Figure 36 for the 959 keV peak in the coincidence-projection spectrum.

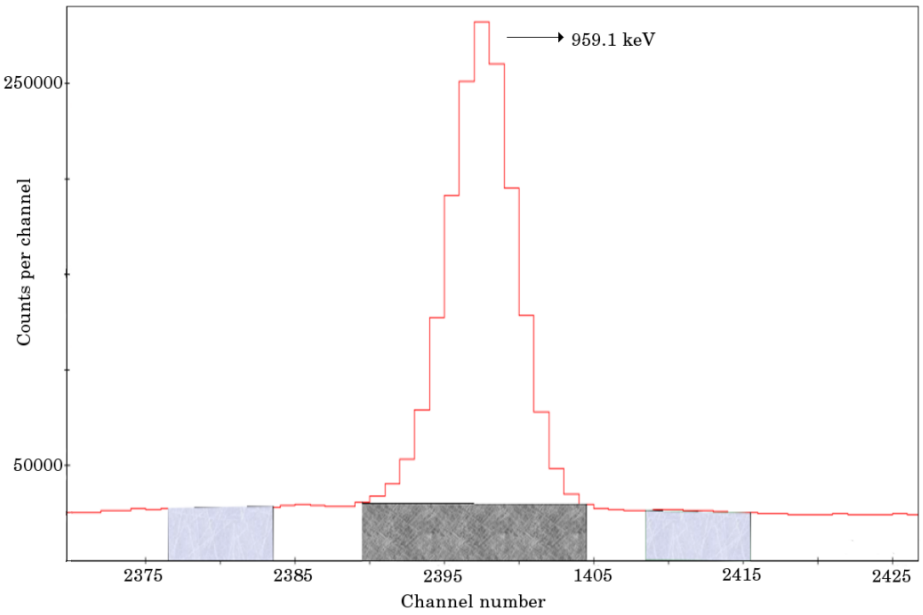

Figure 36: One of the strong peaks (959 keV) in the coincidence spectrum. The dark grey region is the sliced peak, and the light grey regions at the left and the right are sliced backgrounds of equal width in sum to the peak slice.

The necessity of "pulling a running gate" emerged in some cases to resolve close multiplets. This meant slicing a peak into a small, equal number of channels instead of slicing it as a whole peak and then subtracting the background spectrum from each small peak spectrum. In analysis, this method provided a great help in placing the coincident γ rays, and the separation the γ rays of different isobars in the same spectrum, when close in energy.

5.5.2 Level Scheme Construction

A step-by-step procedure was implemented in constructing the level scheme. For each strong peak, all of the coincident γ rays were identified. This process started with the 345 keV gate and was followed by the 453 keV and 586 keV gates. It then continued to higher excitation energies. All γ rays feeding a particular level were identified using this technique. Even very weak γ rays feeding levels at more than 2000 keV excitation energy were placed in the level scheme this way.

The Ritz combination of γ ray energies was used to determine the energy of an excited state. Starting off with the ground level, a weighted average of energy for each level was calculated based on the summing of energies of the γ rays below the level. Each calculated level was then used as a new basis of Ritz combinations for γ rays depopulating the higher levels. The uncertainties coming from the fit of each γ ray energy were used in the calculation of the level uncertainty.

5.6 γ-Ray Intensities

A schematic representation of several different types of analysis used in the experiment to determine the intensities of γ rays is shown in Figure 37. For lower levels, e.g., 345 (see Figure 37.a) and 798 keV (see Figure 37.b), there is only one draining γ ray. A simple α (conversion coefficient) value is sufficient for the branching ratio. In most cases, this could be neglected since it is too small to make a difference in B_γ. However, adopted values [1] or BRICC [53, 54] results were used if the multipoles of the transition are known or can be determined.

For most levels, e.g., 1243 keV (see Figure 37.c), more than one γ ray depopulates the level. In this case, the strongest one, e.g., 899 keV, was picked and the branching ratio of that γ ray was calculated using the intensities of some strong γ rays feeding the level. Intensities for γ rays feeding the level were then determined using the branching ratio of the strong transition and any other appropriate parameters explained in section 5.4.3.

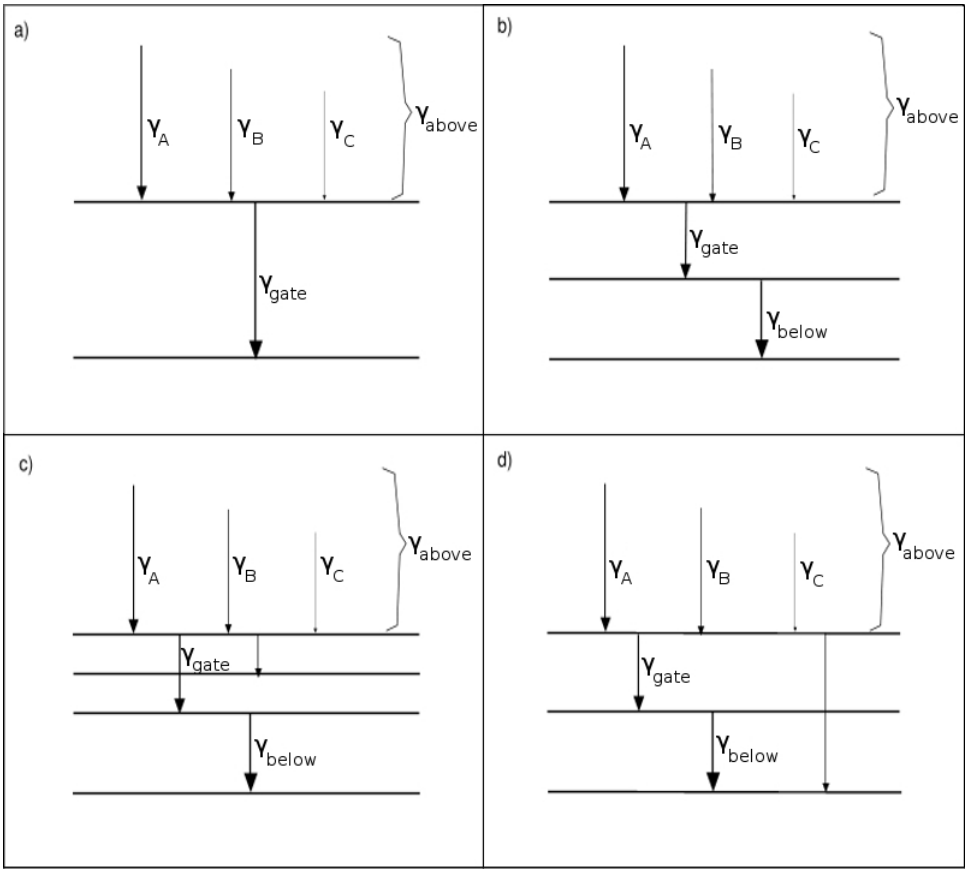

Figure 37: Coincidence intensity analysis for different cases. The schematic representation of the 345 keV level is in a, of 798 keV level is in b, of 1243 keV type levels is in c, and of 930 keV, 1221 keV type levels is in d.

For levels from which a γ-ray transition decays directly to the 0^+ ground level, e.g. 1221 keV (see Figure 37.d), the relative intensities measured through strong γ rays feeding these levels were used to assign the branching ratios of γ rays depopulating the level. The α values were neglected due to their smallness. A reliable branching ratio for 876 keV (which is a very strong transition depopulating the level) was calculated, which eventually results in

computing all γ rays feeding the level. As a second byproduct of this method, the intensity of the 1221 keV γ ray was calculated using the branching ratios and other appropriate parameters explained, in section 5.4.3.

5.6.0.1 The Uncertainty of Intensities

The measured intensity vs. the percent difference in the intensity, $(I_{GT} - I_{NDS})/I_{GT}$, graph is plotted in the Figure 38. For weak intensities ($I_\gamma \leq 2$ where $I_\gamma(345) \equiv 100$), a systematic uncertainty of 8% was determined for γ-ray intensities. Above $I_\gamma > 2$, a systematic uncertainty of 4% was determined. The fit error for areas of peaks and the systematic uncertainties were added to find the total uncertainty for all intensities.

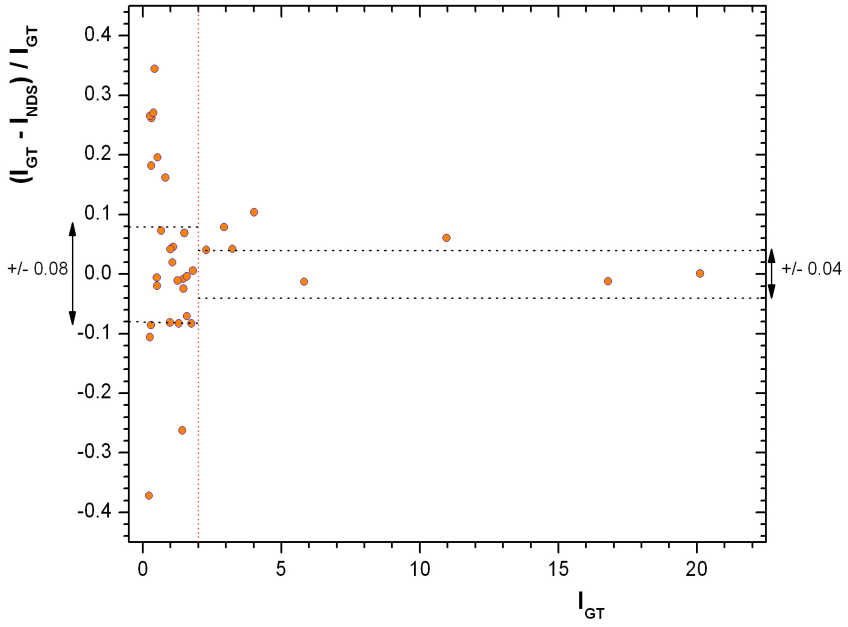

Figure 38: The systematic deviation of intensities in the data set compared to adopted values [1]. For γ rays with intensities $\leq 2\%$ of the strongest γ-ray intensity(=100) it is 0.08, and for stronger transitions it is 0.04.

CHAPTER VI

RESULTS

The population of excited states of ^{156}Er has been carried out by EC/β decay of ^{156}Tm ($T_{\frac{1}{2}} = 83.8sec$). Around 700 γ ray transitions (including 55 previously successfully-assigned transitions) are placed between known or newly established levels. This resulted in a scheme with 261 levels. The number of previously-assigned levels was 26, most of which are located below 2 MeV. The levels which have only one depopulating γ ray have lower confidence at higher energy.

The β decay of ^{156}Tm to ^{156}Er has a high Q-value ($\sim$7380 keV), and the highest γ-ray energy observed in the spectrum is 3276 keV. The contribution of the γ rays beyond that energy is insignificant to the structural understanding of this nucleus. The spin-parity of the parent nucleus, ^{156}Tm, is 2^- [1]. The highest assigned spin for a state in ^{156}Er is 6^+. It is reasonable to suppose that the spin assignments of observed levels should be less than 8 for ^{156}Er. This inference is based on the non-observation of a well-known 8^+ ground-band level at 1959 keV and possible spin assignments of the levels.

In Table 1, the level comparison is shown between our study and two major studies [21, 22] performed previously on this nucleus. Aguer *et al*. failed to observe the 1243, 1518, 1611, 1664, 1711, 1815, 1861, 1909 and 2170 keV levels that Zolnowski *et al*. observed. And Zolnowski *et al*. did not observe the 1341, 1381 and 1836 keV levels that Aguer *et al*. observed. This study added many levels, even in the low-energy region, to the structure; and it also offered some spin changes. The 1304.9 and 2249.9 keV levels (placed by Aguer *et al*.) are removed because of the misplacements of γ rays. In previous ^{156}Tm to ^{156}Er β-decay studies, the highest assigned level was 2249.9 keV. In our study, we were able to assign levels up to $\sim$4600 keV. It is reasonable to stop the comparison around the $\sim$2250 keV level in the Table 1 because of the lack of any previously-assigned levels above this

range.

Table 1: The list of ^{156}Er levels (energies in keV) and spin-parities determined in this study are shown in the first column. In column 2 and column 3, the levels and spin-parities determined by Aguer *et al.* and Zolnowski *et al.*, respectively, are given. The comparison ends at the 2254 keV level because of the lack of any previously-assigned level above this energy.

E_{GT}	J^π	E_{Aguer}	J^π	$E_{Zolnowski}$	J^π
0	0^+	0	0^+	0	0^+
344.59	2^+	344.6	2^+	344.5	2^+
797.53	4^+	797.5	4^+	797.3	4^+
929.99	0^+	930.5	0^+	930.4	0^+
930.44	2^+	930.5	2^+	930.4	2^+
1220.89	2^+	1221.0	2^+	1220.7	2^+
1243.24	3^+			1243.0	(3^+)
1303.68	3^-	1303.6	2^-,3^-	1303.5	3^-
		1304.9			
1340.81	6^+	1341.0	6^+		
1351.42	4^+	1351.4		1351.2	4^+
1380.46	0^+	1382.0			
1406.14	$(2^+, 4^+)$	1406.2		1405.9	(2^+)
1517.95	1^-			1517.9	(1^-)
1546.64	4^+	1546.8	4^+	1546.4	4^+
1570.63	2^+	1570.8	2^+	1570.6	2^+
1611.89	5^-			1611.4	(5^-)
1630.56	$(2^-, 5^+)$	1630.6		1630.4	(2^-)
1663.73	$(2^+, 5^+)$			1663.5	(5^+)
1710.65	2^+			1710.5	(4^+)
1759.53					

Table 1 – continued from previous page

E_{GT}	J^π	E_{Aguer}	J^π	$E_{Zolnowski}$	J^π
1814.74	4^-			1814.5	(4^-)
1836.16	4^+	1836.3			
1860.61				1860.8	(3^+)
1886.34	(6^+)				
1909.46				1909.5	(3^-)
1917.86	(3^+)				
1939.18					
1957.90	4^+				
2014.55	$(2^+, 3^-)$	2014.8		2014.4	
2016.54	2^+				
2022.35	(4^+)				
2070.33	2^+				
2082.94	4^+				
2105.43					
2132.94					
2169.82				2169.8	
2174.67					
2176.88					
2199.35	(4^+)				
2202.21					
2204.71					
2221.95					
		2249.9			
2231.24					
2254.11	2^+				

6.1 The Levels

The high statistics that the 8π detector array system provides, enables one to remove spurious levels from the structure and to add new levels to the known structure of ^{156}Er. A total number of 261 levels have been assigned; 235 new level assignments have been made. An overview of levels up to 1759.5 keV and the γ-ray transitions associated with these levels are given in Figure 39.

Offering a level removal requires reassignments of γ rays associated with the level to other levels. Some γ rays might have been reported by a mistake, or they have been reported due to a containment of other nuclei present in the spectrum, or they may be due to peaks which have not been noticed. Extreme caution has to be implemented in an analysis to obey these rules. The added, removed, and troublesome levels will be discussed in the following sections. A level-by-level approach will be used to discuss the levels.

In Table 2, the results of the β decay of ^{156}Tm to ^{156}Er are shown in terms of levels and corresponding γ-ray transitions. The levels are given in bold type in the far left column of the table. The initial and final energy levels, with their assigned spin-parities, the γ-ray energies, the relative intensities, I_{r_1} (normalized to $I_{344.6}$=100), and relative intensities, I_{r_2} (normalized to the strongest γ ray out of the corresponding level) along with the uncertainties are shown.

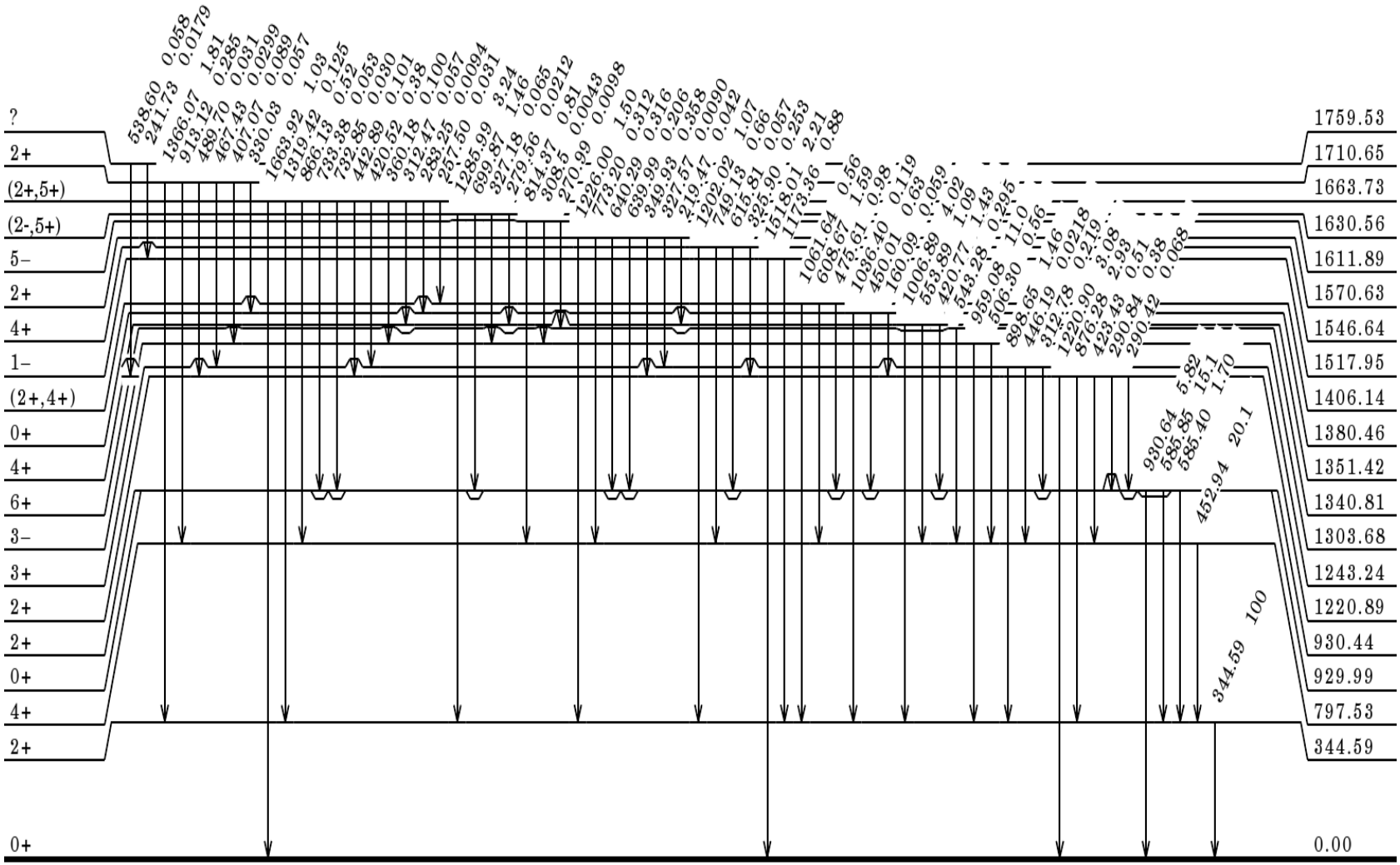

Figure 39: The low-lying levels of ^{156}Er. The transitions between the levels, intensities, and spin-parity assignments (discussed later) are indicated.

Table 2: The observed γ-ray energies (in keV), listed as transitions in ^{156}Er between assigned levels. The assigned spin-parities for some levels are given. The initial level energies (in bold), the final level energies, and the γ-ray energies, along with estimated uncertainties are shown. The relative intensities, I_{r_1}, normalized to ($I_{344.6}$=100) along with their uncertainties are shown in the subsequent columns. The intensities of γ rays depopulating a particular level, I_{r_2}, are normalized (I_γ=100) to the strongest γ ray out of each level.

E_i	dE_i	J_i^π	E_f	J_f^π	E_γ	dE_γ	I_{r_1}	dI_{r_1}	I_{r_2}	dI_{r_2}
344.59	*14*	2^+	0	0^+	344.59	*14*	100	*0*	100	*0*
797.53	*14*	4^+	344.59	2^+	452.94	*14*	20.1	*8*	100	*4*
929.99	*14*	0^+	344.59	2^+	585.40	*14*	1.70	*14*	100	*8*
930.44	*14*	2^+	344.59	2^+	585.85	*14*	15.1	*6*	100	*4*
			0	0^+	930.64	*14*	5.82	*23*	38.6	*15*
1220.89	*14*	2^+	930.44	2^+	290.42	*15*	0.068	*6*	2.21	*21*
			929.99	0^+	290.84	*14*	0.38	*3*	12.4	*10*
			797.53	4^+	423.43	*14*	0.51	*4*	16.5	*13*
			344.59	2^+	876.28	*14*	2.93	*12*	95	*4*
			0	0^+	1220.90	*14*	3.08	*12*	100	*4*
1243.24	*14*	3^+	930.44	2^+	312.78	*14*	0.219	*18*	14.9	*12*
			797.53	4^+	446.19	*16*	0.0218	*26*	1.49	*18*
			344.59	2^+	898.65	*14*	1.46	*12*	100	*8*
1303.68	*14*	3^-	797.53	4^+	506.30	*14*	0.56	*5*	5.1	*4*
			344.59	2^+	959.08	*14*	11.0	*4*	100	*4*
1340.81	*14*	6^+	797.53	4^+	543.28	*14*	0.295	*24*	100	*8*
1351.42	*14*	4^+	930.44	2^+	420.77	*14*	1.43	*11*	35.5	*28*
			797.53	4^+	553.89	*14*	1.09	*9*	27.1	*22*
			344.59	2^+	1006.89	*14*	4.02	*16*	100	*4*
1380.46	*14*	0^+	1220.89	2^+	160.09	*15*	0.059	*6*	9.3	*10*
			930.44	2^+	450.01	*14*	0.63	*5*	100	*8*

Table 2 – continued from previous page

E_i	dE_i	J_i^π	E_f	J_f^π	E_γ	dE_γ	I_{r_1}	dI_{r_1}	I_{r_2}	dI_{r_2}
			344.59	2^+	1036.40	*17*	0.119	*13*	18.8	*21*
1406.14	*14*	$(2^+, 4^+)$	930.44	2^+	475.61	*14*	0.98	*8*	62	*5*
			797.53	4^+	608.67	*14*	1.59	*13*	100	*8*
			344.59	2^+	1061.64	*15*	0.56	*5*	35	*3*
1517.95	*14*	1^-	344.59	2^+	1173.36	*14*	0.88	*7*	40	*3*
			0	0^+	1518.01	*15*	2.21	*9*	100	*4*
1546.64	*14*	4^+	1220.89	2^+	325.90	*14*	0.253	*21*	23.6	*20*
			930.44	4^+	615.81	*14*	0.057	*6*	5.3	*5*
			797.53	4^+	749.13	*14*	0.66	*5*	61	*5*
			344.59	2^+	1202.02	*14*	1.07	*9*	100	*8*
1570.63	*14*	2^+	1351.42	4^+	219.47	*15*	0.042	*4*	2.79	*28*
			1243.24	3^+	327.57	*19*	0.0090	*14*	0.60	*9*
			1220.89	2^+	349.93	*14*	0.358	*29*	23.8	*19*
			930.44	2^+	639.99	*15*	0.206	*18*	13.7	*12*
			929.99	0^+	640.29	*14*	0.316	*26*	21.0	*17*
			797.53	4^+	773.20	*14*	0.312	*25*	20.7	*17*
			344.59	2^+	1226.00	*14*	1.50	*12*	100	*8*
1611.89	*14*	5^-	1340.81	6^+	270.99	*15*	0.0098	*9*	1.21	*12*
			1303.68	3^-	308.5	*4*	0.0043	*19*	0.53	*23*
			797.53	4^+	814.37	*14*	0.81	*7*	100	*8*
1630.56	*14*	$(2^-, 5^+)$	1351.42	4^+	279.56	*16*	0.0212	*25*	0.65	*8*
			1303.68	3^-	327.18	*14*	0.065	*6*	2.02	*18*
			930.44	2^+	699.87	*14*	1.46	*12*	45	*4*
			344.59	2^+	1285.99	*14*	3.24	*13*	100	*4*
1663.73	*14*	$(2^+, 5^+)$	1406.14	$(2^+, 4^+)$	257.50	*15*	0.031	*3*	6.0	*6*
			1380.46	0^+	283.25	*16*	0.0094	*12*	1.81	*23*
			1351.42	4^+	312.47	*14*	0.057	*5*	11.0	*10*

Table 2 – continued from previous page

E_i	dE_i	J_i^π	E_f	J_f^π	E_γ	dE_γ	I_{r_1}	dI_{r_1}	I_{r_2}	dI_{r_2}
			1303.68	3^-	360.18	*14*	0.100	*8*	19.3	*16*
			1243.24	3^+	420.52	*14*	0.38	*3*	74	*6*
			1220.89	2^+	442.89	*14*	0.101	*9*	19.4	*17*
			930.44	2^+	732.85	*22*	0.030	*5*	5.7	*10*
			929.99	0^+	733.38	*15*	0.053	*6*	10.2	*12*
			797.53	4^+	866.13	*14*	0.52	*4*	100	*8*
			344.59	2^+	1319.42	*16*	0.125	*12*	24.1	*24*
			0	0^+	1663.92	*16*	1.03	*8*	198	*16*
1710.65	*14*	2^+	1380.46	0^+	330.03	*14*	0.057	*5*	3.14	*26*
			1303.68	3^-	407.07	*14*	0.089	*8*	4.9	*4*
			1243.24	3^+	467.43	*15*	0.0299	*27*	1.65	*15*
			1220.89	2^+	489.70	*16*	0.031	*4*	1.74	*20*
			797.53	4^+	913.12	*14*	0.285	*23*	15.8	*13*
			344.59	2^+	1366.07	*14*	1.81	*15*	100	*8*
1759.53	*15*		1517.95	1^-	241.73	*17*	0.0179	*22*	31	*4*
			1220.89	2^+	538.60	*15*	0.058	*6*	100	*10*
1814.74	*14*	4^-	797.53	4^+	1017.22	*14*	1.26	*10*	100	*8*
1836.16	*14*	4^+	1406.14	$(2^+, 4^+)$	430.06	*14*	0.162	*13*	37	*3*
			1351.42	4^+	484.68	*22*	0.43	*4*	100	*8*
			1340.81	6^+	494.97	*20*	0.030	*5*	6.9	*12*
			930.44	2^+	905.83	*14*	0.179	*15*	41	*3*
			797.53	4^+	1038.49	*14*	0.170	*14*	39	*3*
1860.61	*14*		1630.56	$(2^-, 5^+)$	230.53	*20*	0.0086	*16*	0.67	*12*
			1303.68	3^-	556.89	*14*	0.075	*6*	5.8	*5*
			930.44	2^+	929.98	*14*	1.25	*10*	97	*8*
			797.53	4^+	1063.14	*14*	0.323	*26*	25.0	*20*
			344.59	2^+	1516.06	*14*	1.29	*10*	100	*8*

Table 2 – continued from previous page

E_i	dE_i	J_i^π	E_f	J_f^π	E_γ	dE_γ	I_{r_1}	dI_{r_1}	I_{r_2}	dI_{r_2}
1886.34	*16*	(6^+)	1406.14	$(2^+,4^+)$	480.40	*21*	0.0121	*19*	100	*15*
			1340.81	6^+	545.48	*16*	0.0066	*8*	55	*6*
1909.46	*14*	$(1^-,2^+)$	930.44	2^+	978.80	*17*	0.046	*5*	2.6	*3*
			344.59	2^+	1564.88	*14*	1.75	*15*	100	*8*
			0	0^+	1909.9	*3*	0.173	*16*	9.9	*9*
1917.86	*14*	(3^+)	1630.56	$(2^-,5^+)$	287.33	*17*	0.0153	*21*	3.3	*4*
			1570.63	2^+	346.88	*14*	0.181	*16*	39	*3*
			1546.64	4^+	371.22	*15*	0.030	*3*	6.5	*7*
			1303.68	3^-	614.25	*17*	0.0218	*27*	4.7	*6*
			1220.89	2^+	697.05	*14*	0.112	*10*	24.1	*22*
			930.44	2^+	987.12	*16*	0.130	*12*	27.9	*3*
			797.53	4^+	1120.47	*14*	0.281	*23*	60	*5*
			344.59	2^+	1573.33	*15*	0.46	*4*	100	*10*
1939.18	*14*		930.44	2^+	1008.74	*14*	0.152	*12*	100	*8*
1957.90	*14*	4^+	1570.63	2^+	387.30	*15*	0.054	*5*	20.7	*20*
			1546.64	4^+	411.34	*15*	0.045	*4*	17.6	*17*
			1406.14	$(2^+,4^+)$	551.47	*15*	0.038	*4*	14.6	*14*
			1340.81	6^+	616.86	*16*	0.0073	*8*	2.8	*3*
			1220.89	2^+	736.95	*26*	0.024	*4*	9.2	*15*
			930.44	2^+	1027.07	*15*	0.068	*7*	26.1	*26*
			797.53	4^+	1160.48	*14*	0.259	*21*	100	*8*
2014.55	*14*	$(2^+,3^-)$	1630.56	$(2^-,5^+)$	384.04	*18*	0.0132	*19*	0.83	*12*
			1517.95	1^-	496.53	*22*	0.0153	*28*	0.96	*18*
			1351.42	4^+	662.91	*15*	0.051	*5*	3.2	*3*
			930.44	2^+	1083.90	*14*	0.306	*26*	19.2	*16*
			344.59	2^+	1670.00	*14*	1.59	*13*	100	*8*
2016.54	*14*	2^+	1546.64	4^+	469.88	*16*	0.0157	*20*	8.1	*10*

Table 2 – continued from previous page

E_i	dE_i	J_i^π	E_f	J_f^π	E_γ	dE_γ	I_{r_1}	dI_{r_1}	I_{r_2}	dI_{r_2}
			1380.46	0^+	635.42	*19*	0.0094	*14*	4.9	*7*
			1351.42	4^+	665.28	*17*	0.031	*4*	16	*19*
			1303.68	3^-	712.88	*14*	0.115	*10*	60	*5*
			1220.89	2^+	795.79	*17*	0.036	*5*	18.5	*24*
			930.44	2^+	1086.07	*15*	0.155	*14*	81	*7*
			0	0^+	2016.7	*4*	0.193	*20*	100	*10*
2022.35	*14*	(4^+)	1710.65	2^+	312.36	*20*	0.0124	*19*	3.2	*5*
			1663.73	$(2^+,5^+)$	358.60	*16*	0.044	*5*	11.4	*13*
			1611.89	5^-	410.71	*17*	0.0071	*9*	1.85	*24*
			1546.64	4^+	475.77	*15*	0.0273	*29*	7.1	*9*
			1406.14	$(2^+,4^+)$	616.00	*16*	0.036	*4*	9.4	*10*
			797.53	4^+	1224.84	*14*	0.171	*15*	45	*4*
			344.59	2^+	1677.67	*15*	0.38	*3*	100	*9*
2070.33	*14*	2^+	1663.73	$(2^+,5^+)$	406.60	*15*	0.063	*6*	28.5	*29*
			1570.63	2^+	500.02	*18*	0.0170	*26*	7.6	*12*
			1351.42	4^+	718.81	*14*	0.122	*11*	55	*5*
			1243.24	3^+	827.17	*14*	0.088	*8*	40	*3*
			930.44	2^+	1139.64	*21*	0.053	*7*	24	*3*
			0	0^+	2070.8	*3*	0.223	*23*	100	*10*
2082.94	*14*	4^+	1351.42	4^+	731.43	*18*	0.025	*3*	5.9	*8*
			1340.81	6^+	742.00	*15*	0.0237	*22*	5.5	*5*
			1303.68	3^-	779.24	*16*	0.028	*3*	6.5	*7*
			1220.89	2^+	861.97	*17*	0.035	*4*	8.2	*10*
			797.53	4^+	1285.48	*16*	0.068	*7*	16.0	*16*
			344.59	2^+	1738.54	*15*	0.43	*4*	100	*9*
2105.43	*14*		1630.68	$(2^-,5^+)$	474.59	*16*	0.0230	*26*	4.3	*5*
			1380.81	0^+	724.58	*17*	0.0160	*19*	3.0	*4*

Table 2 – continued from previous page

E_i	dE_i	J_i^π	E_f	J_f^π	E_γ	dE_γ	I_{r_1}	dI_{r_1}	I_{r_2}	dI_{r_2}
			1220.88	2^+	884.25	*20*	0.040	*5*	7.5	*9*
			930.44	2^+	1174.69	*22*	0.061	*9*	11.5	*17*
			344.59	2^+	1760.87	*14*	0.53	*4*	100	*8*
2132.94	*15*		1546.64	4^+	586.74	*15*	0.034	*4*	27.2	*29*
			1220.89	2^+	911.70	*15*	0.124	*11*	100	*9*
2169.82	*14*		1611.89	5^-	557.88	*15*	0.0141	*15*	1.42	*15*
			1303.68	3^-	865.86	*16*	0.033	*4*	3.4	*4*
			797.53	4^+	1372.33	*14*	0.230	*19*	23.2	*19*
			344.59	2^+	1825.3	*3*	0.99	*8*	100	*8*
2174.67	*15*		1611.89	5^-	562.69	*15*	0.0192	*19*	2.53	*25*
			1220.89	2^+	953.91	*16*	0.070	*7*	9.2	*9*
			344.59	2^+	1830.5	*3*	0.76	*6*	100	*8*
2176.88	*14*		1630.56	$(2^-, 5^+)$	546.10	*16*	0.039	*4*	22.3	*22*
			1611.89	5^-	564.99	*15*	0.0283	*26*	16.0	*15*
			1406.14	$(2^+, 4^+)$	770.73	*14*	0.140	*12*	79	*7*
			1351.42	4^+	825.48	*14*	0.176	*15*	100	*8*
			1303.68	3^-	873.23	*15*	0.081	*7*	46	*4*
			797.53	4^+	1379.44	*16*	0.070	*7*	40	*4*
2199.35	*14*	(4^+)	1710.65	2^+	488.80	*16*	0.0170	*20*	4.2	*5*
			1351.42	4^+	847.88	*17*	0.032	*4*	8.0	*10*
			1220.89	2^+	978.61	*17*	0.048	*5*	11.8	*13*
			930.44	2^+	1268.74	*15*	0.211	*18*	52	*4*
			344.59	2^+	1854.9	*3*	0.41	*3*	100	*9*
2202.21	*14*		797.53	4^+	1404.68	*14*	0.344	*28*	63	*5*
			344.59	2^+	1857.6	*3*	0.55	*5*	100	*8*
2204.71	*16*		1340.81	6^+	863.90	*16*	0.0122	*13*	100	*10*
2221.95	*15*		930.44	2^+	1291.48	*15*	0.206	*18*	32.2	*28*

Table 2 – continued from previous page

E_i	dE_i	J_i^π	E_f	J_f^π	E_γ	dE_γ	I_{r_1}	dI_{r_1}	I_{r_2}	dI_{r_2}
			797.53	4^+	1424.53	*16*	0.085	*8*	13.3	*13*
			344.59	2^+	1877.7	*3*	0.64	*5*	100	*8*
2231.24	*15*		1836.16	4^+	395.7	*5*	0.027	*3*	45	*5*
			1611.89	5^-	619.21	*16*	0.0108	*13*	17.9	*21*
			1406.14	$(2^+, 4^+)$	825.05	*15*	0.061	*6*	100	*10*
			797.53	4^+	1434.00	*17*	0.054	*6*	89	*9*
2254.11	*14*	2^+	1710.65	2^+	543.67	*15*	0.0225	*24*	11.1	*12*
			1663.73	$(2^+, 5^+)$	590.61	*18*	0.027	*4*	13.4	*18*
			1517.95	1^-	736.10	*16*	0.039	*4*	19.4	*21*
			1380.46	0^+	873.31	*15*	0.0287	*28*	14.1	*14*
			1351.42	4^+	902.74	*22*	0.017	*3*	8.5	*15*
			1220.89	2^+	1033.26	*15*	0.138	*12*	68	*6*
			930.44	2^+	1323.59	*18*	0.057	*7*	28	*4*
			797.53	4^+	1456.80	*18*	0.046	*5*	22.5	*26*
			344.59	2^+	1909.8	*3*	0.203	*19*	100	*9*
2261.21	*15*		1630.56	$(2^-, 5^+)$	630.49	*18*	0.0223	*29*	2.6	*3*
			1517.95	1^-	743.27	*17*	0.025	*3*	3.0	*4*
			930.44	2^+	1330.80	*15*	0.285	*25*	33.9	*29*
			344.59	2^+	1916.9	*3*	0.84	*7*	100	*8*
2266.92	*16*		1611.89	5^-	654.88	*18*	0.0072	*10*	2.6	*4*
			1546.64	4^+	720.37	*17*	0.0220	*27*	7.9	*10*
			1220.89	2^+	1046.06	*21*	0.025	*4*	9.1	*14*
			344.59	2^+	1922.4	*3*	0.279	*24*	100	*9*
2271.40	*19*		930.44	2^+	1340.96	*19*	0.052	*7*	100	*13*
2286.59	*15*		1611.89	5^-	674.60	*17*	0.0097	*12*	19.9	*24*
			1340.81	6^+	945.78	*15*	0.0210	*20*	43	*4*
			797.53	4^+	1489.21	*19*	0.049	*6*	100	*12*

Table 2 – continued from previous page

E_i	dE_i	J_i^π	E_f	J_f^π	E_γ	dE_γ	I_{r_1}	dI_{r_1}	I_{r_2}	dI_{r_2}
2298.64	*14*		1814.74	4^-	483.92	*16*	0.0113	*13*	3.5	*4*
			1570.63	2^+	727.99	*17*	0.023	*3*	7.2	*10*
			1303.68	3^-	994.83	*16*	0.043	*4*	13.1	*13*
			930.44	2^+	1367.70	*20*	0.069	*9*	21.2	*26*
			797.53	4^+	1501.24	*15*	0.104	*9*	31.8	*29*
			344.59	2^+	1954.2	*3*	0.33	*4*	100	*12*
2315.34	*14*	2^+	1630.56	$(2^-, 5^+)$	684.73	*17*	0.0202	*25*	18.3	*23*
			1517.95	1^-	797.51	*19*	0.0201	*29*	18.2	*26*
			1380.46	0^+	934.20	*17*	0.0175	*21*	15.8	*19*
			1243.24	3^+	1072.18	*14*	0.077	*7*	70	*6*
			930.44	2^+	1385.03	*19*	0.065	*8*	58	*7*
			344.59	2^+	1971.0	*3*	0.111	*13*	100	*11*
2325.60	*16*		1611.89	5^-	713.46	*17*	0.0094	*12*	4.6	*6*
			797.53	4^+	1528.42	*19*	0.21	*4*	100	*18*
2326.72	*14*		1630.56	$(2^-, 5^+)$	696.54	*17*	0.0185	*24*	6.8	*9*
			1406.14	$(2^+, 4^+)$	920.90	*16*	0.032	*3*	11.9	*13*
			1351.42	4^+	975.12	*14*	0.271	*23*	100	*8*
			1303.68	3^-	1023.37	*15*	0.066	*6*	24.3	*23*
			1220.89	2^+	1106.12	*15*	0.085	*8*	31	*3*
			930.44	2^+	1396.56	*20*	0.057	*7*	20.9	*27*
			797.53	4^+	1529.70	*18*	0.24	*4*	88	*14*
			344.59	2^+	1983.0	*3*	0.079	*12*	29	*5*
2334.22	*19*		1340.81	6^+	993.41	*19*	0.0063	*9*	100	*14*
2342.67	*15*		1611.89	5^-	730.93	*17*	0.0099	*12*	14.7	*18*
			1546.64	4^+	796.02	*21*	0.0127	*21*	19	*3*
			1406.14	$(2^+, 4^+)$	936.42	*16*	0.035	*4*	51	*6*
			1351.42	4^+	991.48	*23*	0.018	*3*	27	*5*

Table 2 – continued from previous page

E_i	dE_i	J_i^π	E_f	J_f^π	E_γ	dE_γ	I_{r_1}	dI_{r_1}	I_{r_2}	dI_{r_2}
			1303.68	3^-	1038.85	*20*	0.021	*3*	31	*4*
			797.53	4^+	1545.29	*21*	0.068	*10*	100	*14*
2348.55	*15*		1517.95	1^-	830.60	*15*	0.052	*5*	100	*10*
2357.94	*14*		1303.68	3^-	1054.25	*14*	0.38	*3*	100	*8*
			1220.89	2^+	1136.95	*22*	0.025	*4*	6.7	*11*
			797.53	4^+	1560.50	*15*	0.202	*17*	54	*5*
2360.28	*15*		1570.63	2^+	790.27	*20*	0.021	*3*	27	*4*
			1406.14	$(2^+, 4^+)$	954.08	*15*	0.076	*7*	100	*9*
2363.11	*16*		1351.42	4^+	1011.81	*20*	0.024	*4*	17.6	*26*
			1303.68	3^-	1059.61	*19*	0.023	*3*	16.8	*23*
			930.44	2^+	1432.42	*19*	0.049	*6*	37	*5*
			344.59	2^+	2018.77	*16*	0.134	*14*	100	*10*
2371.35	*14*		1710.65	2^+	660.92	*16*	0.025	*3*	35	*4*
			1630.56	$(2^-, 5^+)$	740.68	*15*	0.072	*7*	100	*9*
			1517.95	1^-	853.70	*17*	0.031	*4*	43	*5*
			1380.46	0^+	991.01	*24*	0.0079	*16*	11.0	*22*
			1220.89	2^+	1150.42	*25*	0.020	*4*	27	*5*
			930.44	2^+	1441.0	*4*	0.0092	*25*	13	*3*
			929.99	0^+	1441.25	*16*	0.042	*5*	58	*7*
2372.78	*15*	4^+	1611.89	5^-	760.76	*16*	0.0162	*17*	11.5	*12*
			1340.81	6^+	1032.07	*15*	0.0169	*17*	12.0	*12*
			344.59	2^+	2027.5	*3*	0.141	*14*	100	*10*
2388.74	*15*		1710.65	2^+	677.73	*18*	0.0140	*19*	24	*3*
			1570.63	2^+	817.87	*19*	0.023	*3*	40	*6*
			1351.42	4^+	1037.48	*16*	0.058	*6*	100	*10*
			1243.24	3^+	1145.58	*16*	0.029	*3*	49	*5*
			1220.89	2^+	1167.90	*19*	0.035	*5*	61	*8*

Table 2 – continued from previous page

E_i	dE_i	J_i^π	E_f	J_f^π	E_γ	dE_γ	I_{r_1}	dI_{r_1}	I_{r_2}	dI_{r_2}
2396.87	*14*		1220.89	2^+	1176.12	*17*	0.048	*6*	21.8	*26*
			929.99	0^+	1466.86	*14*	0.222	*18*	100	*8*
			344.59	2^+	2052.6	*3*	0.116	*12*	52	*6*
2402.83	*15*		1406.14	$(2^+, 4^+)$	996.52	*20*	0.0175	*26*	10.0	*15*
			797.53	4^+	1605.34	*16*	0.175	*16*	100	*9*
2409.82	*27*		1611.89	5^-	797.93	*27*	0.0040	*9*	100	*22*
2411.48	*15*		1303.68	3^-	1107.80	*15*	0.057	*6*	17.7	*17*
			344.59	2^+	2067.2	*3*	0.324	*28*	100	*9*
2428.13	*15*		1814.74	4^-	613.34	*16*	0.0132	*15*	6.9	*8*
			1351.42	4^+	1076.63	*15*	0.070	*7*	37	*4*
			1303.68	3^-	1124.20	*23*	0.0164	*28*	8.6	*15*
			797.53	4^+	1630.91	*17*	0.062	*6*	33	*3*
			344.59	2^+	2083.9	*3*	0.190	*20*	100	*10*
2433.34	*16*		797.53	4^+	1635.81	*16*	0.077	*7*	100	*10*
2444.06	*18*		1243.24	3^+	1200.82	*18*	0.0164	*21*	100	*13*
2449.74	*15*		1406.14	$(2^+, 4^+)$	1043.32	*19*	0.0209	*28*	26	*3*
			1303.68	3^-	1145.90	*21*	0.021	*3*	27	*4*
			797.53	4^+	1652.35	*16*	0.081	*8*	100	*10*
2461.50	*14*		1351.42	4^+	1109.66	*22*	0.022	*4*	4.5	*7*
			797.53	4^+	1663.98	*14*	0.50	*4*	100	*8*
			344.59	2^+	2116.7	*3*	0.253	*22*	51	*4*
2469.38	*17*		1517.95	1^-	951.43	*16*	0.039	*4*	100	*11*
2481.29	*14*		1860.61		620.71	*25*	0.015	*3*	9.5	*21*
			1814.74	4^-	666.60	*15*	0.0294	*28*	19.2	*18*
			1630.56	$(2^-, 5^+)$	850.59	*20*	0.0151	*23*	9.9	*15*
			1611.89	5^-	869.07	*19*	0.0120	*17*	7.9	*11*
			1351.42	4^+	1129.70	*20*	0.028	*4*	18.0	*26*

Table 2 – continued from previous page

E_i	dE_i	J_i^π	E_f	J_f^π	E_γ	dE_γ	I_{r_1}	dI_{r_1}	I_{r_2}	dI_{r_2}
			1303.68	3^-	1177.62	*14*	0.153	*13*	100	*8*
2482.8	*3*		344.59	2^+	2138.2	*3*	0.287	*25*	100	*9*
2490.86	*23*		1860.61		629.32	*23*	0.017	*3*	100	*20*
2491.12	*15*		1611.89	5^-	879.20	*19*	0.0081	*12*	9.4	*14*
			1303.68	3^-	1187.26	*16*	0.052	*5*	61	*6*
			797.53	4^+	1693.78	*16*	0.086	*8*	100	*9*
2496.97	*14*		1351.42	4^+	1145.55	*17*	0.044	*5*	12.5	*14*
			930.44	2^+	1566.54	*15*	0.36	*3*	100	*8*
2512.68	*15*		1860.61		651.88	*20*	0.024	*4*	52	*8*
			1517.95	1^-	995.03	*18*	0.034	*4*	75	*9*
			1406.14	$(2^+, 4^+)$	1106.20	*28*	0.0104	*23*	23	*5*
			1340.81	6^+	1171.73	*19*	0.0078	*10*	17.1	*22*
			797.53	4^+	1715.13	*19*	0.045	*5*	100	*12*
2524.22	*15*		930.44	2^+	1593.41	*22*	0.101	*16*	62	*10*
			797.53	4^+	1726.74	*15*	0.119	*11*	74	*7*
			344.59	2^+	2180.0	*3*	0.161	*19*	100	*12*
2532.55	*16*		1303.68	3^-	1228.87	*16*	0.061	*6*	29.5	*29*
			344.59	2^+	2187.9	*3*	0.205	*19*	100	*9*
2536.71	*14*		2014.55		521.98	*23*	0.0103	*19*	3.2	*6*
			1836.16	4^+	700.50	*16*	0.0210	*23*	6.5	*7*
			1814.74	4^-	722.06	*17*	0.0106	*14*	3.3	*4*
			1663.73	$(2^+, 5^+)$	873.15	*18*	0.035	*5*	10.9	*15*
			1570.63	2^+	966.06	*22*	0.039	*5*	12.1	*16*
			1303.68	3^-	1232.91	*19*	0.028	*4*	8.7	*11*
			930.44	2^+	1606.28	*15*	0.203	*18*	63	*5*
			344.59	2^+	2192.5	*3*	0.324	*28*	100	*9*
2552.85	*17*		1611.89	5^-	940.96	*17*	0.0118	*14*	100	*12*

Table 2 – continued from previous page

E_i	dE_i	J_i^π	E_f	J_f^π	E_γ	dE_γ	I_{r_1}	dI_{r_1}	I_{r_2}	dI_{r_2}
2554.32	*14*	2^+	1630.56	$(2^-,5^+)$	923.78	*16*	0.034	*4*	23.4	*26*
			1517.95	1^-	1036.38	*15*	0.067	*6*	46	*5*
			1243.24	3^+	1311.06	*16*	0.030	*3*	20.6	*22*
			929.99	0^+	1624.31	*15*	0.144	*13*	100	*9*
			344.59	2^+	2209.4	*4*	0.059	*9*	41	*6*
2564.77	*15*		797.53	4^+	1767.25	*15*	0.113	*10*	100	*9*
2571.10	*14*		1351.42	4^+	1219.61	*16*	0.058	*6*	15.9	*17*
			930.44	2^+	1640.68	*15*	0.36	*3*	100	*8*
2574.82	*17*		1303.68	3^-	1271.13	*17*	0.043	*5*	28	*3*
			1220.89	2^+	1354.02	*27*	0.021	*4*	13.9	*27*
			344.59	2^+	2230.6	*4*	0.154	*15*	100	*10*
2576.54	*14*		1836.16	4^+	740.15	*16*	0.0252	*26*	59	*6*
			1814.74	4^-	761.87	*15*	0.043	*4*	100	*9*
			1406.14	$(2^+,4^+)$	1170.46	*20*	0.0197	*29*	46	*7*
2577.97	*16*		1303.68	3^-	1274.28	*26*	0.0152	*29*	10.3	*20*
			797.53	4^+	1780.44	*16*	0.147	*15*	100	*10*
			344.59	2^+	2233.8	*4*	0.106	*13*	72	*9*
2582.27	*17*		1611.89	5^-	970.37	*17*	0.0127	*16*	100	*12*
2587.12	*15*		1630.56	$(2^-,5^+)$	956.57	*16*	0.046	*5*	20.7	*21*
			1303.68	3^-	1283.62	*23*	0.020	*3*	8.9	*15*
			930.44	2^+	1656.48	*21*	0.041	*6*	18.6	*26*
			344.59	2^+	2242.8	*5*	0.223	*23*	100	*10*
2599.0	*3*		1351.42	4^+	1247.5	*3*	0.014	*3*	7.3	*17*
			797.53	4^+	1801.91	*20*	0.041	*5*	20.4	*27*
			344.59	2^+	2254.7	*4*	0.199	*19*	100	*9*
2599.98	*16*		1611.89	5^-	988.09	*16*	0.0241	*24*	100	*10*
2604.79	*15*		1630.56	$(2^-,5^+)$	973.8	*0*	0.0084	*21*	5.3	*13*

Table 2 – continued from previous page

E_i	dE_i	J_i^π	E_f	J_f^π	E_γ	dE_γ	I_{r_1}	dI_{r_1}	I_{r_2}	dI_{r_2}
			1546.64	4^+	1058.09	*17*	0.035	*4*	21.9	*25*
			1406.14	$(2^+,4^+)$	1198.72	*19*	0.026	*3*	16.0	*20*
			1303.68	3^-	1301.31	*18*	0.037	*4*	23.1	*27*
			1220.89	2^+	1384.04	*20*	0.076	*12*	48	*7*
			930.44	2^+	1673.75	*23*	0.159	*22*	100	*14*
2607.16	*15*	2^+	1517.95	1^-	1089.21	*25*	0.040	*5*	42	*5*
			1243.24	3^+	1363.72	*16*	0.035	*4*	37	*4*
			1220.89	2^+	1386.1	*0*	0.030	*11*	32	*11*
			929.99	0^+	1677.13	*22*	0.095	*17*	100	*18*
			344.59	2^+	2262.7	*4*	0.081	*11*	85	*12*
2623.90	*15*		1836.16	4^+	787.68	*25*	0.031	*3*	32	*3*
			1814.74	4^-	809.11	*16*	0.0214	*22*	22.0	*23*
			1546.64	4^+	1077.11	*22*	0.0155	*25*	16	*3*
			1406.14	$(2^+,4^+)$	1218.17	*22*	0.022	*3*	23	*3*
			1351.42	4^+	1272.65	*27*	0.018	*3*	18	*4*
			797.53	4^+	1826.7	*3*	0.098	*8*	100	*9*
2625.6	*3*		344.59	2^+	2281.0	*4*	0.106	*12*	100	*11*
2633.36	*15*		2014.55		618.75	*16*	0.0219	*24*	43	*5*
			1814.74	4^-	818.84	*17*	0.0117	*15*	23.2	*29*
			1406.14	$(2^+,4^+)$	1226.9	*4*	0.0190	*28*	37	*6*
			1351.42	4^+	1281.81	*17*	0.051	*6*	100	*11*
			1303.68	3^-	1329.77	*19*	0.037	*4*	73	*9*
2642.98	*17*		1611.84		1030.91	*25*	0.0113	*14*	12.4	*16*
			1517.98	1^-	1125.14	*20*	0.035	*4*	38	*5*
			1303.75	3^-	1339.16	*26*	0.022	*4*	24	*4*
			797.53	4^+	1844.91	*17*	0.092	*9*	100	*10*
2657.37	*15*		2261.36		395.92	*16*	0.0151	*18*	37	*5*

Table 2 – continued from previous page

E_i	dE_i	J_i^π	E_f	J_f^π	E_γ	dE_γ	I_{r_1}	dI_{r_1}	I_{r_2}	dI_{r_2}
			2014.55		642.87	*16*	0.040	*4*	100	*10*
			1630.56	$(2^-, 5^+)$	1026.78	*23*	0.0133	*25*	33	*6*
2661.52	*15*		1406.14	$(2^+, 4^+)$	1255.53	*22*	0.080	*7*	30.1	*2*
			1220.89	2^+	1440.62	*21*	0.049	*6*	18.5	*23*
			930.44	2^+	1731.06	*16*	0.161	*15*	60	*6*
			344.59	2^+	2317.6	*3*	0.267	*23*	100	*9*
2662.92	*18*		1611.89	5^-	1051.03	*18*	0.0169	*19*	15.8	*18*
			797.53	4^+	1866.0	*3*	0.107	*10*	100	*9*
2673.40	*15*		1546.64	4^+	1126.86	*23*	0.0154	*27*	11.5	*20*
			1351.42	4^+	1322.0	*3*	0.027	*6*	20	*4*
			1220.89	2^+	1452.62	*17*	0.060	*7*	45	*5*
			930.44	2^+	1742.86	*16*	0.092	*9*	68	*7*
			344.59	2^+	2329.3	*3*	0.135	*14*	100	*11*
2679.09	*15*		1836.16	4^+	842.82	*18*	0.0151	*20*	39	*5*
			1814.74	4^-	864.48	*16*	0.0164	*19*	42	*5*
			1406.14	$(2^+, 4^+)$	1272.66	*22*	0.0190	*29*	48	*8*
			1351.42	4^+	1327.55	*19*	0.039	*5*	100	*13*
			1303.68	3^-	1375.59	*19*	0.031	*4*	78	*10*
2681.5	*4*		797.53	4^+	1883.9	*4*	0.038	*5*	100	*14*
2686.61	*15*	$(2^+, 3^-)$	1630.56	$(2^-, 5^+)$	1056.02	*15*	0.069	*7*	45	*4*
			1517.95	1^-	1168.71	*16*	0.062	*6*	40	*4*
			1351.42	4^+	1335.20	*20*	0.032	*5*	20.5	*29*
			930.44	2^+	1756.12	*22*	0.089	*12*	58	*8*
			344.59	2^+	2342.4	*4*	0.155	*19*	100	*12*
2688.32	*15*		1909.46	$(1^-, 2^+)$	778.57	*23*	0.0158	*20*	13.6	*17*
			1243.24	3^+	1445.2	*4*	0.052	*5*	45	*4*
			1220.89	2^+	1467.41	*16*	0.101	*10*	87	*9*

Table 2 – continued from previous page

E_i	dE_i	J_i^π	E_f	J_f^π	E_γ	dE_γ	I_{r_1}	dI_{r_1}	I_{r_2}	dI_{r_2}
			930.44	2^+	1758.25	*22*	0.116	*17*	100	*14*
			797.53	4^+	1890.6	*3*	0.078	*7*	68	*6*
2689.72	*16*		1303.68	3^-	1386.05	*16*	0.049	*5*	100	*11*
2698.13	*15*		1351.42	4^+	1346.67	*17*	0.052	*6*	28	*3*
			1220.89	2^+	1477.52	*20*	0.031	*5*	16.7	*26*
			930.44	2^+	1767.65	*16*	0.187	*17*	100	*9*
2708.80	*16*		1611.89	5^-	1096.91	*16*	0.0185	*20*	99	*11*
			1303.68	3^-	1405.07	*26*	0.019	*3*	100	*18*
2714.92	*17*		1351.42	4^+	1363.50	*17*	0.053	*6*	100	*11*
2716.5	*3*		344.59	2^+	2371.9	*3*	0.53	*5*	100	*10*
2718.45	*15*		1351.42	4^+	1367.09	*27*	0.017	*4*	19	*4*
			1303.68	3^-	1414.74	*15*	0.093	*8*	100	*9*
			1220.89	2^+	1497.54	*22*	0.038	*5*	41	*6*
			930.44	2^+	1788.36	*24*	0.043	*6*	46	*7*
2721.29	*16*		1340.81	6^+	1380.48	*16*	0.0138	*15*	100	*11*
2722.75	*20*		1611.89	5^-	1110.86	*20*	0.0097	*15*	14.9	*22*
			797.53	4^+	1925.6	*3*	0.065	*7*	100	*11*
2732.58	*16*	$(1^-, 2^+)$	1380.46	0^+	1351.87	*18*	0.0227	*26*	35	*4*
			1303.68	3^-	1429.31	*29*	0.065	*6*	100	*10*
			1220.89	2^+	1511.88	*18*	0.043	*6*	66	*9*
			929.99	0^+	1802.7	*4*	0.043	*5*	66	*8*
2736.12	*17*		1814.74	4^-	921.50	*19*	0.0107	*15*	11.1	*16*
			1406.14	$(2^+, 4^+)$	1329.81	*21*	0.020	*3*	21	*3*
			797.53	4^+	1938.9	*3*	0.096	*9*	100	*9*
2744.39	*29*		1630.56	$(2^-, 5^+)$	1113.83	*29*	0.0167	*27*	8.7	*14*
			344.59	2^+	2400.0	*3*	0.192	*18*	100	*10*
2753.5	*3*		797.53	4^+	1956.0	*3*	0.085	*8*	100	*10*

Table 2 – continued from previous page

E_i	dE_i	J_i^π	E_f	J_f^π	E_γ	dE_γ	I_{r_1}	dI_{r_1}	I_{r_2}	dI_{r_2}
2757.65	*22*		1303.68	3^-	1453.98	*22*	0.028	*4*	100	*14*
2760.49	*15*	$(2^+,3^-)$	1814.74	4^-	945.48	*16*	0.0185	*20*	22.8	*25*
			1546.64	4^+	1213.61	*21*	0.039	*5*	48	*6*
			1517.95	1^-	1242.45	*24*	0.018	*3*	22	*4*
			1351.42	4^+	1408.96	*22*	0.028	*4*	34	*5*
			1303.68	3^-	1457.08	*16*	0.081	*8*	100	*9*
			797.53	4^+	1963.1	*4*	0.046	*6*	57	*7*
2761.75	*17*		1630.56	$(2^-,5^+)$	1131.18	*18*	0.024	*3*	10.5	*14*
			1570.63	2^+	1191.13	*22*	0.034	*5*	14.7	*20*
			344.59	2^+	2417.6	*3*	0.231	*21*	100	*9*
2773.3	*3*		797.53	4^+	1975.83	*18*	0.083	*8*	51	*5*
			344.59	2^+	2428.71	*20*	0.163	*17*	100	*11*
2775.04	*22*		1630.56	$(2^-,5^+)$	1144.50	*25*	0.012	*2*	5.7	*11*
			1303.68	3^-	1471.3	*3*	0.015	*3*	7.4	*16*
			344.59	2^+	2431.10	*22*	0.208	*24*	100	*12*
2783.18	*16*		1860.61		922.60	*25*	0.022	*4*	11.4	*23*
			1611.89	5^-	1171.27	*25*	0.0077	*13*	4.0	*7*
			1303.68	3^-	1479.50	*16*	0.060	*6*	32	*3*
			797.53	4^+	1985.8	*3*	0.092	*9*	48	*5*
			344.59	2^+	2439.3	*3*	0.191	*19*	100	*10*
2787.52	*16*		1303.68	3^-	1483.71	*19*	0.035	*4*	65	*8*
			1220.89	2^+	1566.76	*19*	0.054	*7*	100	*13*
2792.56	*15*		1630.56	$(2^-,5^+)$	1161.98	*15*	0.093	*8*	47	*4*
			1570.63	2^+	1221.95	*18*	0.050	*6*	24.8	*28*
			1517.95	1^-	1274.62	*23*	0.020	*3*	9.8	*16*
			1220.89	2^+	1571.92	*29*	0.022	*5*	10.8	*23*
			930.44	2^+	1862.3	*3*	0.200	*17*	100	*9*

Table 2 – continued from previous page

E_i	dE_i	J_i^π	E_f	J_f^π	E_γ	dE_γ	I_{r_1}	dI_{r_1}	I_{r_2}	dI_{r_2}
2795.56	*16*		1814.74	4^-	980.82	*16*	0.0188	*21*	100	*11*
2797.21	*19*		1570.63	2^+	1226.58	*19*	0.032	*4*	67	*9*
			797.53	4^+	2000.1	*4*	0.048	*6*	100	*12*
2801.37	*20*		344.59	2^+	2456.8	*3*	0.093	*11*	100	*12*
2820.14	*18*		1303.68	3^-	1516.46	*18*	0.038	*4*	20.1	*24*
			344.59	2^+	2476.0	*3*	0.189	*18*	100	*9*
2830.45	*16*		1243.24	3^+	1587.25	*18*	0.0219	*27*	24	*3*
			1220.89	2^+	1609.51	*18*	0.064	*7*	70	*8*
			930.44	2^+	1900.4	*3*	0.091	*9*	100	*10*
2832.96	*16*		2222.15		611.22	*18*	0.0119	*16*	74	*10*
			1814.74	4^-	1017.88	*17*	0.0160	*20*	100	*12*
2841.2	*5*		344.59	2^+	2496.7	*5*	0.093	*14*	100	*15*
2842.4	*3*		1351.42	4^+	1491.0	*3*	0.023	*5*	100	*20*
2844.81	*24*		1303.68	3^-	1541.13	*24*	0.022	*4*	14.6	*24*
			930.44	2^+	1915.0	*3*	0.149	*14*	100	*9*
2846.94	*17*		1710.65	2^+	1136.55	*19*	0.0189	*27*	12.6	*18*
			1630.56	$(2^-, 5^+)$	1216.09	*20*	0.023	*3*	15.1	*21*
			797.53	4^+	2049.5	*7*	0.039	*16*	26	*11*
			344.59	2^+	2502.7	*4*	0.150	*16*	100	*11*
2853.25	*16*		1303.68	3^-	1549.58	*16*	0.054	*6*	36	*4*
			344.59	2^+	2509.0	*3*	0.150	*15*	100	*10*
2855.49	*24*		1406.14	$(2^+, 4^+)$	1449.35	*24*	0.0174	*29*	28	*5*
			797.53	4^+	2058.6	*4*	0.063	*7*	100	*12*
2859.28	*16*		1630.56	$(2^-, 5^+)$	1228.72	*16*	0.046	*5*	59	*6*
			344.59	2^+	2515.4	*5*	0.078	*12*	100	*16*
2865.6	*4*		797.53	4^+	2068.1	*4*	0.077	*10*	100	*13*
2868.25	*21*		1220.89	2^+	1647.36	*21*	0.042	*6*	49	*7*

Table 2 – continued from previous page

E_i	dE_i	J_i^π	E_f	J_f^π	E_γ	dE_γ	I_{r_1}	dI_{r_1}	I_{r_2}	dI_{r_2}
			930.44	2^+	1937.8	*3*	0.063	*7*	74	*9*
			344.59	2^+	2523.4	*4*	0.086	*11*	100	*13*
2871.44	*18*		1303.68	3^-	1567.76	*18*	0.046	*5*	64	*7*
			344.59	2^+	2527.4	*4*	0.073	*11*	100	*15*
2879.38	*24*		1406.14	$(2^+,4^+)$	1473.24	*24*	0.018	*3*	100	*17*
2883.84	*15*		1630.56	$(2^-,5^+)$	1253.51	*21*	0.0173	*27*	13.9	*22*
			1517.95	1^-	1365.67	*17*	0.048	*5*	38	*4*
			1303.68	3^-	1580.53	*20*	0.032	*4*	26	*3*
			1220.89	2^+	1662.89	*17*	0.068	*8*	55	*6*
			930.44	2^+	1953.3	*4*	0.035	*7*	28	*6*
			929.99	0^+	1953.5	*3*	0.029	*5*	23	*4*
			344.59	2^+	2539.5	*3*	0.124	*14*	100	*11*
2891.53	*15*		1406.14	$(2^+,4^+)$	1485.39	*15*	0.079	*7*	100	*9*
			1351.42	4^+	1540.16	*22*	0.030	*4*	38	*6*
2895.90	*22*		1303.68	3^-	1592.22	*22*	0.025	*4*	73	*11*
			930.44	2^+	1965.0	*4*	0.034	*6*	100	*18*
2898.90	*19*		1611.89	5^-	1287.03	*20*	0.0098	*14*	6.5	*10*
			1570.63	2^+	1328.2	*3*	0.013	*3*	8.9	*22*
			930.44	2^+	1968.7	*4*	0.062	*8*	41	*5*
			797.53	4^+	2101.4	*4*	0.034	*5*	23	*3*
			344.59	2^+	2553.9	*3*	0.151	*15*	100	*10*
2911.81	*18*		1303.68	3^-	1608.13	*18*	0.036	*4*	24.4	*29*
			344.59	2^+	2567.9	*4*	0.149	*22*	100	*15*
2915.46	*22*		1351.42	4^+	1564.04	*22*	0.031	*5*	100	*15*
2918.42	*16*		1380.46	0^+	1538.1	*3*	0.0071	*19*	16	*4*
			1243.24	3^+	1675.18	*16*	0.045	*5*	100	*10*
2921.5	*6*		1303.68	3^-	1617.8	*6*	0.0072	*29*	29	*12*

Table 2 – continued from previous page

E_i	dE_i	J_i^π	E_f	J_f^π	E_γ	dE_γ	I_{r_1}	dI_{r_1}	I_{r_2}	dI_{r_2}
			797.53	4^+	2123.6	*4*	0.024	*4*	100	*18*
2926.48	*16*		1546.64	4^+	1379.87	*17*	0.048	*5*	90	*10*
			1351.42	4^+	1575.03	*18*	0.053	*6*	100	*11*
			1303.68	3^-	1622.5	*4*	0.018	*4*	33	*8*
2928.6	*4*		1303.68	3^-	1625.0	*4*	0.017	*4*	11.7	*29*
			797.53	4^+	2130.8	*4*	0.028	*5*	19	*3*
			344.59	2^+	2583.3	*3*	0.149	*14*	100	*10*
2933.4	*4*		344.59	2^+	2588.8	*4*	0.062	*10*	100	*16*
2936.14	*15*		1814.74	4^-	1121.40	*15*	0.033	*3*	100	*10*
2937.74	*15*		1517.95	1^-	1419.95	*16*	0.066	*7*	100	*10*
			1303.68	3^-	1633.87	*16*	0.061	*6*	93	*9*
2941.4	*3*		797.53	4^+	2143.8	*3*	0.112	*10*	71	*6*
			344.59	2^+	2596.9	*3*	0.156	*16*	100	*10*
2942.37	*24*		1303.68	3^-	1638.69	*24*	0.024	*4*	100	*16*
2945.7	*3*		344.59	2^+	2601.1	*3*	0.130	*14*	100	*11*
2949.46	*18*		1611.89	5^-	1337.57	*18*	0.0151	*19*	100	*12*
2951.17	*18*		1814.74	4^-	1136.48	*19*	0.0118	*17*	15.5	*22*
			1406.14	$(2^+, 4^+)$	1544.94	*22*	0.020	*3*	26	*4*
			344.60	2^+	2606.8	*4*	0.076	*11*	100	*15*
2955.85	*17*		1630.56	$(2^-, 5^+)$	1325.20	*22*	0.0174	*28*	49	*8*
			1517.95	1^-	1437.95	*19*	0.036	*5*	100	*13*
2960.0	*4*		797.53	4^+	2162.5	*4*	0.026	*4*	100	*17*
2967.80	*18*		1406.14	$(2^+, 4^+)$	1561.50	*21*	0.022	*3*	40	*6*
			1303.68	3^-	1664.28	*21*	0.055	*6*	100	*11*
			930.44	2^+	2036.6	*4*	0.038	*6*	68	*11*
2969.2	*4*		344.59	2^+	2624.6	*4*	0.089	*12*	100	*14*
2975.70	*23*		1630.56	$(2^-, 5^+)$	1345.14	*23*	0.0161	*27*	17.9	*3*

Table 2 – continued from previous page

E_i	dE_i	J_i^π	E_f	J_f^π	E_γ	dE_γ	I_{r_1}	dI_{r_1}	I_{r_2}	dI_{r_2}
2976.46	*15*		1710.65	2^+	1265.96	*16*	0.037	*4*	41	*4*
			1351.42	4^+	1624.73	*16*	0.078	*8*	87	*9*
			1303.68	3^-	1672.99	*18*	0.043	*5*	47	*5*
			1220.89	2^+	1755.97	*25*	0.026	*5*	29	*5*
			930.44	2^+	2046.2	*3*	0.090	*9*	100	*10*
2978.2	*3*		797.53	4^+	2180.7	*3*	0.061	*7*	100	*11*
2980.42	*19*		1814.74	4^-	1165.68	*19*	0.0122	*17*	20.3	*28*
			344.60	2^+	2636.0	*4*	0.060	*10*	100	*17*
2988.31	*18*		1611.89	5^-	1376.53	*18*	0.0143	*18*	83	*10*
			1303.68	3^-	1684.22	*27*	0.017	*3*	100	*20*
2993.82	*18*		1243.24	3^+	1750.59	*18*	0.035	*4*	100	*10*
2997.29	*18*		1406.14	$(2^+, 4^+)$	1591.15	*18*	0.038	*4*	100	*11*
3006.63	*16*		1814.74	4^-	1191.98	*18*	0.0143	*18*	13.6	*17*
			1630.56	$(2^-, 5^+)$	1376.12	*20*	0.022	*3*	21	*3*
			1351.42	4^+	1654.9	*3*	0.030	*4*	28	*4*
			1303.68	3^-	1702.66	*28*	0.017	*3*	16	*3*
			344.59	2^+	2661.8	*3*	0.105	*12*	100	*11*
3008.0	*5*		797.53	4^+	2210.5	*5*	0.016	*4*	100	*28*
3015.76	*15*		1406.14	$(2^+, 4^+)$	1609.41	*20*	0.050	*5*	41	*4*
			1303.68	3^-	1712.15	*16*	0.083	*8*	69	*7*
			930.44	2^+	2085.4	*4*	0.032	*6*	27	*5*
			797.53	4^+	2218.6	*3*	0.121	*11*	100	*9*
			344.59	2^+	2671.0	*4*	0.115	*14*	96	*11*
3023.9	*4*		344.59	2^+	2679.3	*4*	0.090	*12*	100	*13*
3033.8	*3*		1220.89	2^+	1812.4	*4*	0.037	*5*	35	*5*
			930.44	2^+	2103.3	*3*	0.022	*3*	21	*3*
			929.99	0^+	2104.2	*4*	0.033	*3*	32	*3*

Table 2 – continued from previous page

E_i	dE_i	J_i^π	E_f	J_f^π	E_γ	dE_γ	I_{r_1}	dI_{r_1}	I_{r_2}	dI_{r_2}
			344.59	2^+	2689.6	*4*	0.106	*13*	100	*13*
3034.94	*17*		1517.95	1^-	1517.14	*19*	0.035	*4*	100	*13*
			1303.68	3^-	1731.07	*20*	0.032	*4*	91	*12*
3038.27	*20*		1611.89	5^-	1426.31	*25*	0.0070	*13*	13.9	*26*
			1406.14	$(2^+, 4^+)$	1632.20	*25*	0.0166	*28*	33	*6*
			930.44	2^+	2108.0	*4*	0.050	*7*	100	*13*
3041.55	*17*		1860.61		1181.02	*21*	0.039	*6*	58	*9*
			1303.68	3^-	1737.83	*18*	0.043	*5*	62	*7*
			344.59	2^+	2697.6	*5*	0.068	*11*	100	*17*
3043.88	*15*		2357.94		685.76	*17*	0.0167	*21*	63	*8*
			2202.21		842.02	*20*	0.0134	*22*	51	*8*
			1710.65	2^+	1333.25	*18*	0.027	*3*	100	*12*
3062.97	*17*		1351.42	4^+	1711.56	*17*	0.063	*7*	59	*6*
			344.59	2^+	2718.9	*4*	0.106	*14*	100	*13*
3073.76	*14*		2357.94		715.50	*16*	0.0241	*27*	7.3	*8*
			2326.72		746.28	*18*	0.035	*5*	10.7	*15*
			2169.85		903.59	*24*	0.0072	*15*	2.2	*5*
			2014.55		1059.40	*16*	0.043	*5*	13.0	*14*
			1836.16	4^+	1237.21	*16*	0.034	*4*	10.3	*11*
			1814.74	4^-	1259.04	*15*	0.061	*5*	18.5	*17*
			1710.65	2^+	1363.14	*16*	0.050	*5*	15.4	*15*
			1630.56	$(2^-, 5^+)$	1442.75	*17*	0.045	*5*	13.6	*15*
			1546.64	4^+	1527.22	*15*	0.086	*8*	26.3	*25*
			1406.14	$(2^+, 4^+)$	1667.52	*15*	0.141	*12*	43	*4*
			1351.42	4^+	1722.50	*14*	0.328	*28*	100	*8*
			1303.68	3^-	1770.55	*17*	0.055	*6*	16.6	*18*
			930.44	2^+	2143.4	*4*	0.061	*8*	18.7	*25*

Table 2 – continued from previous page

E_i	dE_i	J_i^π	E_f	J_f^π	E_γ	dE_γ	I_{r_1}	dI_{r_1}	I_{r_2}	dI_{r_2}
			797.53	4^+	2276.6	*4*	0.068	*7*	20.6	*22*
3074.9	*3*		1243.24	3^+	1831.5	*3*	0.0199	*25*	25	*3*
			1220.89	2^+	1854.0	*3*	0.068	*8*	86	*10*
			344.59	2^+	2730.9	*4*	0.079	*12*	100	*15*
3078.69	*22*		1611.89	5^-	1466.80	*22*	0.0092	*14*	100	*15*
3080.3	*4*		344.59	2^+	2735.7	*4*	0.103	*13*	100	*13*
3083.5	*4*		1351.42	4^+	1732.50	*27*	0.024	*5*	42	*8*
			1303.68	3^-	1779.54	*25*	0.022	*4*	37	*6*
			344.59	2^+	2739.0	*5*	0.059	*11*	100	*19*
3091.75	*22*		1406.14	$(2^+, 4^+)$	1685.62	*22*	0.023	*3*	100	*15*
3093.71	*17*		1351.42	4^+	1742.30	*17*	0.062	*7*	56	*6*
			930.44	2^+	2162.9	*4*	0.110	*12*	100	*11*
3094.61	*15*		1546.64	4^+	1547.86	*16*	0.060	*6*	18.3	*19*
			1303.68	3^-	1791.10	*17*	0.050	*5*	15.1	*16*
			1220.89	2^+	1873.8	*3*	0.063	*7*	19.1	*22*
			797.53	4^+	2297.4	*3*	0.330	*27*	100	*8*
			344.59	2^+	2750.8	*4*	0.122	*14*	37	*4*
3103.07	*21*		1351.42	4^+	1751.65	*21*	0.034	*5*	67	*9*
			929.99	0^+	2173.2	*4*	0.020	*4*	39	*8*
			344.59	2^+	2759.3	*4*	0.052	*10*	100	*19*
3105.79	*26*		1630.56	$(2^-, 5^+)$	1475.23	*26*	0.0152	*28*	21	*4*
			1303.68	3^-	1803.0	*3*	0.072	*7*	100	*10*
3114.74	*21*		1630.56	$(2^-, 5^+)$	1484.18	*21*	0.022	*3*	98	*14*
			1303.68	3^-	1811.3	*4*	0.022	*4*	100	*16*
3119.6	*4*		344.60	2^+	2775.0	*4*	0.101	*12*	100	*12*
3124.91	*18*		1611.89	5^-	1513.02	*18*	0.0155	*19*	100	*12*
3128.89	*19*		1710.65	2^+	1418.42	*22*	0.0150	*23*	50	*8*

Table 2 – continued from previous page

E_i	dE_i	J_i^π	E_f	J_f^π	E_γ	dE_γ	I_{r_1}	dI_{r_1}	I_{r_2}	dI_{r_2}
			1351.42	4^+	1777.28	*23*	0.030	*5*	100	*15*
3133.0	*4*		1243.24	3^+	1889.7	*4*	0.0141	*24*	100	*17*
3134.5	*4*		1303.68	3^-	1830.8	*4*	0.023	*4*	100	*18*
3138.10	*21*		1570.63	2^+	1567.46	*21*	0.028	*4*	19.1	*29*
			1303.68	3^-	1834.8	*3*	0.049	*5*	34	*4*
			344.59	2^+	2794.3	*4*	0.145	*22*	100	*15*
3150.6	*5*		344.59	2^+	2806.0	*4*	0.088	*19*	100	*22*
3158.13	*23*		1630.56	$(2^-, 5^+)$	1527.57	*23*	0.027	*4*	45	*6*
			344.59	2^+	2814.4	*4*	0.061	*10*	100	*17*
3164.91	*20*		1611.89	5^-	1553.01	*20*	0.0125	*17*	100	*13*
3174.00	*3*		1303.68	3^-	1870.3	*3*	0.038	*5*	82	*10*
			344.59	2^+	2829.3	*5*	0.046	*9*	100	*20*
3184.18	*19*		1710.65	2^+	1473.62	*22*	0.0153	*25*	69	*11*
			1630.56	$(2^-, 5^+)$	1553.50	*24*	0.0167	*29*	75	*13*
			1303.68	3^-	1880.9	*4*	0.022	*4*	100	*17*
3191.9	*4*		344.59	2^+	2847.3	*4*	0.063	*10*	100	*16*
3194.1	*4*		1570.63	2^+	1623.48	*22*	0.030	*5*	80	*12*
			797.53	4^+	2396.7	*4*	0.038	*5*	100	*14*
3203.0	*4*		1303.68	3^-	1899.3	*4*	0.022	*4*	100	*17*
3205.47	*18*		1814.74	4^-	1390.72	*18*	0.0222	*26*	43	*5*
			797.53	4^+	2406.6	*4*	0.051	*6*	100	*12*
3221.5	*5*		344.59	2^+	2876.9	*5*	0.045	*9*	100	*21*
3229.1	*3*		1406.14	$(2^+, 4^+)$	1822.4	*4*	0.0133	*26*	6.5	*13*
			1351.42	4^+	1878.0	*4*	0.019	*4*	9.2	*19*
			797.53	4^+	2431.2	*4*	0.042	*6*	20.9	*28*
			344.59	2^+	2884.8	*4*	0.203	*20*	100	*10*
3243.62	*16*		1917.86		1325.85	*19*	0.038	*5*	67	*9*

Table 2 – continued from previous page

E_i	dE_i	J_i^π	E_f	J_f^π	E_γ	dE_γ	I_{r_1}	dI_{r_1}	I_{r_2}	dI_{r_2}
			1570.63	2^+	1672.91	*18*	0.056	*6*	100	*11*
3249.67	*16*		2202.21		1047.18	*18*	0.024	*3*	61	*8*
			1630.56	$(2^-, 5^+)$	1619.27	*24*	0.021	*3*	53	*8*
			1546.64	4^+	1703.28	*18*	0.040	*5*	100	*12*
			1220.89	2^+	2028.3	*4*	0.022	*5*	54	*11*
3250.79	*21*		1517.95	1^-	1732.84	*21*	0.032	*4*	100	*13*
3253.0	*3*		1351.42	4^+	1901.6	*4*	0.028	*4*	19	*3*
			344.59	2^+	2908.5	*3*	0.147	*15*	100	*10*
3260.0	*3*		1303.68	3^-	1956.5	*4*	0.020	*3*	14.6	*24*
			797.53	4^+	2463.0	*4*	0.027	*4*	19	*3*
			344.59	2^+	2915.3	*3*	0.139	*14*	100	*10*
3275.41	*20*		1909.46	$(1^-, 2^+)$	1365.95	*20*	0.0183	*25*	18.0	*24*
			797.53	4^+	2477.2	*4*	0.038	*5*	37	*5*
			344.59	2^+	2930.7	*4*	0.102	*12*	100	*12*
3276.16	*15*		2222.15		1054.01	*15*	0.058	*6*	26.5	*26*
			1517.95	1^-	1758.20	*16*	0.071	*7*	33	*3*
			1351.42	4^+	1925.6	*4*	0.022	*4*	10.2	*19*
			1303.68	3^-	1973.0	*4*	0.021	*3*	9.5	*16*
			930.44	2^+	2345.8	*3*	0.217	*20*	100	*9*
3289.0	*4*		1351.42	4^+	1937.4	*4*	0.025	*4*	28	*5*
			930.44	2^+	2358.5	*3*	0.092	*10*	100	*11*
			344.59	2^+	2944.5	*4*	0.073	*11*	80	*12*
3292.14	*21*		1570.63	2^+	1721.50	*21*	0.032	*5*	100	*14*
3296.21	*25*		1546.64	4^+	1749.57	*25*	0.017	*3*	13.1	*23*
			1303.68	3^-	1992.3	*3*	0.057	*6*	43	*4*
			344.59	2^+	2952.1	*3*	0.132	*14*	100	*11*
3313.7	*3*		797.53	4^+	2516.7	*4*	0.047	*6*	38	*5*

Table 2 – continued from previous page

E_i	dE_i	J_i^π	E_f	J_f^π	E_γ	dE_γ	I_{r_1}	dI_{r_1}	I_{r_2}	dI_{r_2}
			344.59	2^+	2968.7	*3*	0.124	*14*	100	*11*
3318.5	*4*		797.53	4^+	2520.9	*4*	0.029	*5*	40	*7*
			344.59	2^+	2974.0	*4*	0.071	*11*	100	*15*
3338.1	*4*		1303.68	3^-	2034.4	*4*	0.021	*3*	100	*16*
3340.68	*22*		1611.89	5^-	1728.79	*22*	0.0100	*15*	41	*6*
			1517.95	1^-	1822.5	*4*	0.024	*4*	100	*16*
3373.3	*3*		797.53	4^+	2575.7	*3*	0.097	*9*	100	*10*
			344.59	2^+	3029.1	*4*	0.093	*12*	96	*12*
3386.8	*4*		1351.42	4^+	2035.4	*4*	0.024	*4*	100	*17*
3400.5	*3*		797.53	4^+	2602.9	*3*	0.057	*6*	62	*7*
			344.59	2^+	3056.0	*4*	0.092	*12*	100	*13*
3420.4	*4*		1517.95	1^-	1902.4	*4*	0.014	*3*	52	*11*
			1303.68	3^-	2116.7	*4*	0.028	*4*	100	*14*
3421.17	*24*		1630.56	$(2^-, 5^+)$	1790.61	*24*	0.019	*3*	36	*6*
			1351.42	4^+	2070.0	*4*	0.035	*5*	67	*9*
			930.44	2^+	2491.6	*4*	0.053	*7*	100	*13*
3437.5	*3*		1710.65	2^+	1726.9	*3*	0.0100	*21*	100	*22*
3453.5	*3*		344.59	2^+	3108.9	*3*	0.177	*17*	100	*10*
3467.4	*6*		344.59	2^+	3122.8	*6*	0.048	*13*	100	*27*
3485.2	*3*		1517.95	1^-	1967.2	*4*	0.027	*4*	100	*15*
			1303.68	3^-	2181.8	*4*	0.021	*3*	79	*12*
			797.53	4^+	2687.4	*5*	0.020	*4*	75	*17*
3498.8	*3*		1570.63	2^+	1927.8	*4*	0.021	*4*	21	*4*
			1303.68	3^-	2195.3	*4*	0.023	*3*	23	*3*
			1220.89	2^+	2278.0	*4*	0.024	*5*	24	*5*
			344.59	2^+	3154.3	*4*	0.099	*13*	100	*13*
3534.5	*4*		1303.68	3^-	2230.8	*4*	0.023	*3*	100	*15*

Table 2 – continued from previous page

E_i	dE_i	J_i^π	E_f	J_f^π	E_γ	dE_γ	I_{r_1}	dI_{r_1}	I_{r_2}	dI_{r_2}
3536.1	*4*		344.59	2^+	3191.5	*4*	0.074	*12*	100	*16*
3542.6	*4*		797.53	4^+	2745.1	*4*	0.028	*5*	100	*18*
3547.6	*3*		1351.42	4^+	2196.2	*4*	0.020	*4*	10	*19*
			344.59	2^+	3203.0	*3*	0.191	*19*	100	*10*
3597.9	*4*		1303.68	3^-	2293.9	*5*	0.0114	*29*	23	*6*
			930.44	2^+	2667.5	*4*	0.050	*7*	100	*15*
3606.9	*5*		1351.42	4^+	2255.5	*5*	0.017	*4*	100	*22*
3631.9	*3*		1710.65	2^+	1921.1	*3*	0.026	*3*	100	*13*
			1243.24	3^+	2388.9	*4*	0.0157	*25*	60	*9*
3668.3	*4*		1243.24	3^+	2425.1	*4*	0.0114	*21*	100	*18*
3693.2	*4*		797.53	4^+	2895.7	*4*	0.029	*5*	100	*18*
3718.9	*4*		930.44	2^+	2788.5	*4*	0.056	*8*	100	*14*
3783.7	*4*		1351.42	4^+	2432.3	*4*	0.025	*4*	100	*16*
3844.2	*4*		930.44	2^+	2913.7	*4*	0.044	*7*	100	*17*
3969.2	*4*		1630.56	$(2^-, 5^+)$	2338.7	*4*	0.019	*3*	100	*18*
4032.1	*5*		930.44	2^+	3101.7	*5*	0.036	*8*	100	*21*
4093.6	*5*		930.44	2^+	3163.2	*5*	0.039	*8*	100	*20*
4173.6	*4*		1630.56	$(2^-, 5^+)$	2543.1	*4*	0.017	*3*	100	*20*
4203.6	*5*		1220.89	2^+	2982.8	*5*	0.031	*7*	100	*22*
4210.8	*4*		1630.56	$(2^-, 5^+)$	2580.3	*4*	0.020	*4*	100	*18*
4234.7	*5*		1220.89	2^+	3013.8	*5*	0.034	*7*	100	*21*
4238.5	*4*		1517.95	1^-	2720.3	*4*	0.019	*4*	100	*22*
			1243.24	3^+	2995.8	*5*	0.0124	*27*	65	*14*
4263.9	*4*		1243.24	3^+	3020.6	*4*	0.020	*3*	100	*17*
4325.6	*4*		1517.95	1^-	2808.1	*4*	0.025	*5*	73	*14*
			1303.68	3^-	3021.7	*4*	0.034	*5*	100	*14*
			1243.24	3^+	3082.9	*6*	0.0095	*25*	28	*7*

Table 2 – continued from previous page

E_i	dE_i	J_i^π	E_f	J_f^π	E_γ	dE_γ	I_{r_1}	dI_{r_1}	I_{r_2}	dI_{r_2}
4346.4	*4*		1710.65	2^+	2635.7	*4*	0.022	*4*	100	*17*
4403.1	*4*		1303.68	3^-	3099.4	*4*	0.025	*4*	100	*17*
4412.0	*6*		1220.89	2^+	3191.1	*6*	0.027	*8*	100	*29*
4440.7	*4*		1630.56	$(2^-, 5^+)$	2810.4	*5*	0.018	*4*	77	*16*
			1517.95	1^-	2922.4	*5*	0.017	*4*	75	*18*
			1303.68	3^-	3137.1	*4*	0.023	*4*	100	*19*
4477.6	*5*		1630.56	$(2^-, 5^+)$	2847.1	*5*	0.016	*4*	100	*24*
4551.8	*5*		1630.56	$(2^-, 5^+)$	2921.2	*5*	0.019	*4*	100	*21*
4613.8	*5*		1710.65	2^+	2903.1	*5*	0.019	*4*	100	*21*

6.1.1 Two levels at 930 keV

One of the accomplishments of this study is the separation of the bandhead of the β band ($J^\pi = 0^+$) from the bandhead of the γ band ($J^\pi = 2^+$) at ∼930 keV. The bandhead of the β band is determined to be at 930.0 keV, and the bandhead of the γ band at 930.4 keV. The reported transitions (except a new 585.4 keV transition) and the total intensity out of the levels (before separation) are confirmed. The coincidence relations of γ rays depopulating the levels give sufficient information about the double character of the levels.

The 586 keV line is compared in the 700 (1630.6→930.4), 420 (1351.4→930.4), and 290 keV (depopulating the 1220.9 keV level) gated spectra as shown in Figure 40. Certainly, the 420.8 and 699.9 keV γ rays feed the 2^+_γ level at 930.4 keV. The centroid shift of the 586 keV line in the 290 keV gated spectrum, if compared to the 421 and 700 keV gated spectra, provides sufficient evidence that a 290 keV γ ray feeds a second level as well. The 699.9 and 420.8 keV γ rays are chosen in the figure intentionally because these γ rays feed only the 2^+_γ level.

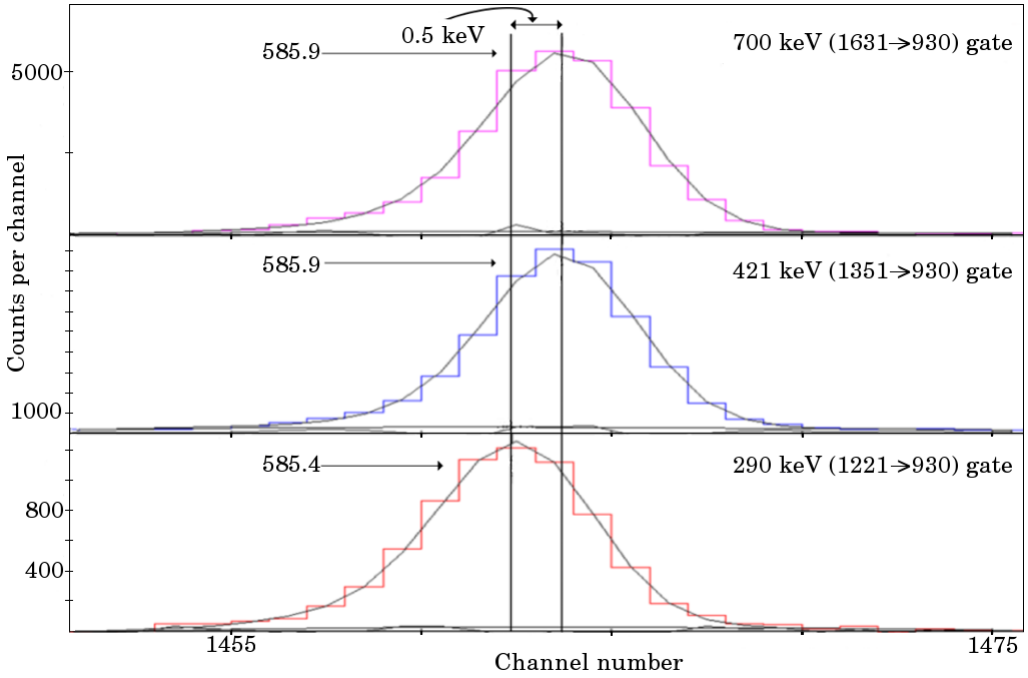

Figure 40: The 586 keV line observed in the 700, 421, and 290 keV (two separate transitions: 1220.9→930.4 and 1220.9→930.0) γ-ray gated γ-ray spectra. The centroid shift of the 586 keV line in the 290 keV gated spectrum provides evidence for a 585.4 keV transition.

In the 421 and 700 keV gated spectra, the intensity ratio of the 931 keV line to the 586 keV line appeared to be the same as opposed to the ratio in the 290 and 640 keV gated spectra, as shown in the Figure 41. The ratio in the 290 and 640 keV gated spectra appeared significantly less than the ratio in the former two. This is the second piece of evidence that these two γ-rays feed not only the 0^+_β level but also the 2^+_γ level. The centroid location of the 586 keV line in the 640 keV (1570.6→930) gated spectrum does not line up with the location in the 290 gated spectrum, as well as in the 420 and 700 keV gated spectra. It is found to be in between them. It can be inferred that the 640 keV transition populates both the 0^+_β and 2^+_γ levels. Also, the intensity ratio of the 931 keV line to the 586 keV line in the 640 gated spectrum is less than the ratio of the same lines in the 420 and 700 keV gated spectra, but it is higher than that in the 290 keV gated spectrum. This results in the intensity ratio of the 640 keV γ ray feeding 0^+_β level with respect to 640 keV γ ray feeding 2^+_γ level being less than the intensity ratio of 290 keV γ ray feeding the same levels. The energies and intensities for 290 keV transitions are found to be 290.4 keV

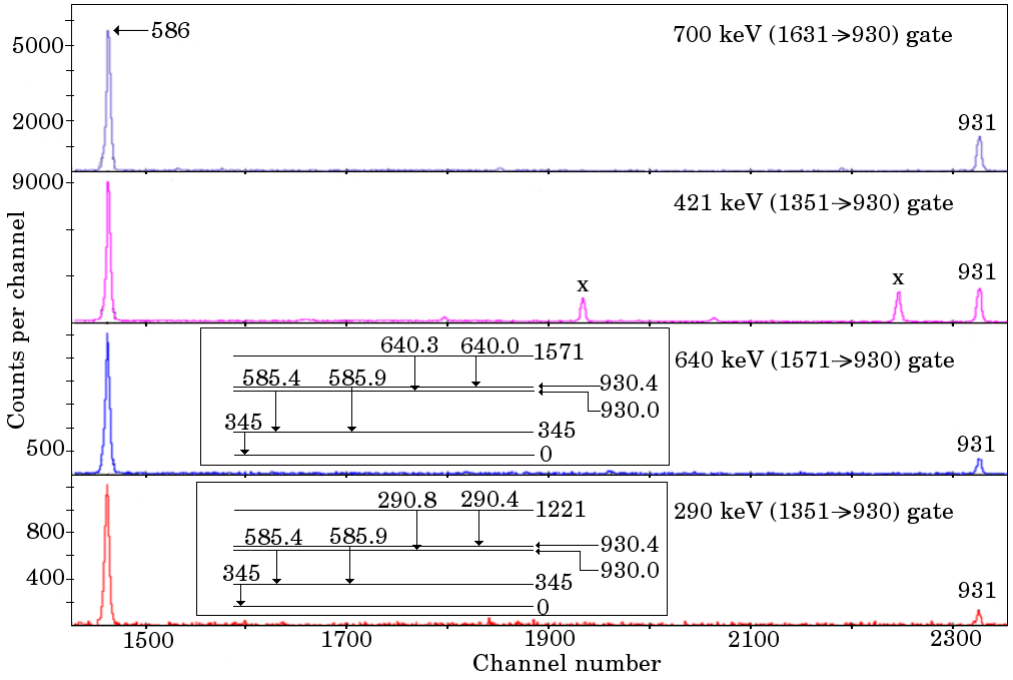

Figure 41: The intensity ratio of the 586 keV line to the 930.6 keV line is observed to be the same in the 700 and 420 keV gated spectra. In the 640 and 290 keV gated spectra, the ratio is considerably higher. The 420.8 and 699.9 keV γ rays feed directly the 930.4 keV level, whereas the 290 and 640 keV lines have portions feeding both the 930.0 and 930.4 keV levels. In the 421 keV gated spectrum, the lines which are not of interest are shown with $\times$.

(1220.9→930.4) with $I_\gamma = 0.068(6)$ and 290.8 keV (1220.9→930.0) with $I_\gamma = 0.38(3)$, and for 640 keV transitions to be as 640.0 keV (1570.6→930.4) with $I_\gamma = 0.206(18)$ and 640.3 keV (1570.6→930.0) with $I_\gamma = 0.316(26)$.

The γ rays at 290.4, 640.0, 732.9, 1441.0, 1953.3, and 2103.3 keV are observed to feed the 930.4 keV, 2^+_γ level, and the γ rays at 290.8, 640.3, 733.4, 1441.3, 1953.5, 2104.2 keV to feed the 930.0 keV, 0^+_β level with different intensity ratios. The 1466.9, 1624.3, 1677.1, 1802.7, and 2173.2 keV γ rays feed only the 0^+_β level. The inference that they only feed the 0^+_β level is made by the non-existence of a 930.6 keV line and the centroid shift of the 586 keV in the corresponding gated spectra. The expectation is that the number of γ rays feeding the 0^+_β level has to be significantly less than the number of γ rays feeding the 2^+_γ level, which is confirmed in our study.

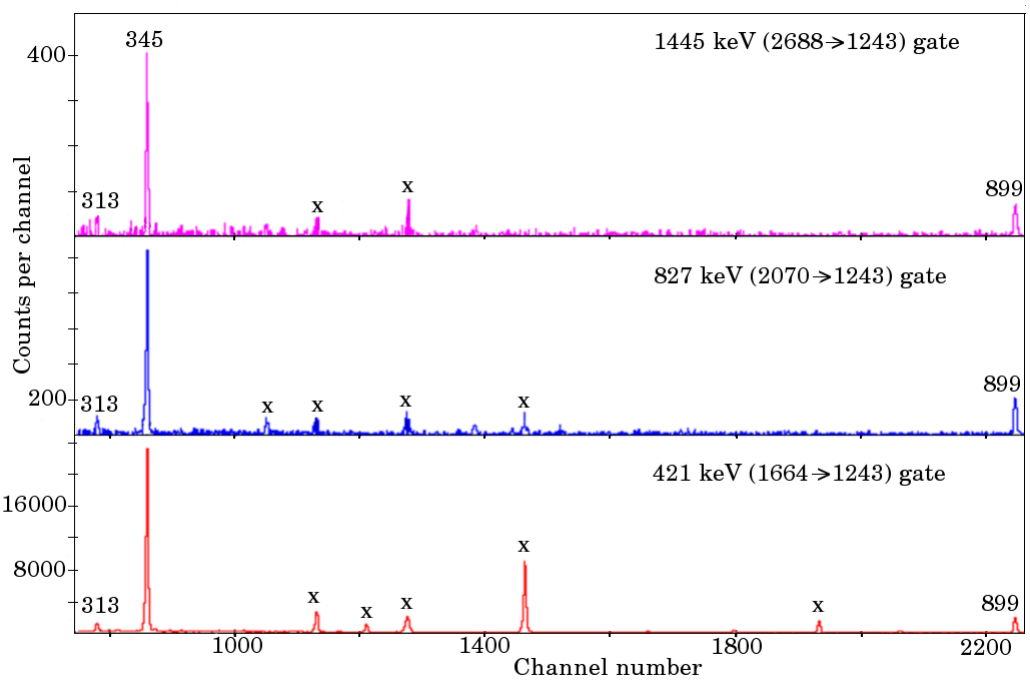

Figure 42: The 313 and 899 keV lines are shown in the 1445 (2688.3→1243.2), 827 (2070.3→1243.2), and 421 keV (1663.7→1243.2) gated spectra. Both the 312.8 and 898.7 keV γ rays line up in all of the spectra proving that they depopulate the same level. Gamma rays not of interest are shown with $\times$.

6.1.2 The 1243.2 keV level

The 898.7 keV γ ray to the 2_g^+ level is confirmed, and the tentative assignment of the 312.8 keV γ ray in the adopted data [1], with $I_\gamma = 0.219(18)$, to the 2_γ^+ level is confirmed also. A third γ ray, at 446.2 keV, with $I_\gamma = 0.0218(26)$, to the 4_g^+ state, is observed depopulating the level weakly. In the 453 keV gated spectrum, it is hard to observe the weak 446.2 keV γ ray, yet the 446 keV gated spectrum provides remarkably evidence for the existence of the 453 keV line. The transitions to the 2^+ levels and the expected band structure (the bands will be discussed later) suggest that this level has 3^+ spin-parity.

The 1445.2 ($I_\gamma = 0.053(5)$), 827.2 ($I_\gamma = 0.088(8)$) and 420.5 keV ($I_\gamma = 0.38(3)$) γ rays populate 1243.2 keV level. The intensity ratio of the 313 keV line to the 898 keV line is observed to be the same in Figure 42. Additionally, the exact same location of the 313 and 898 keV lines in the gated spectra, evidently, proves that they depopulate the 1243.2 keV

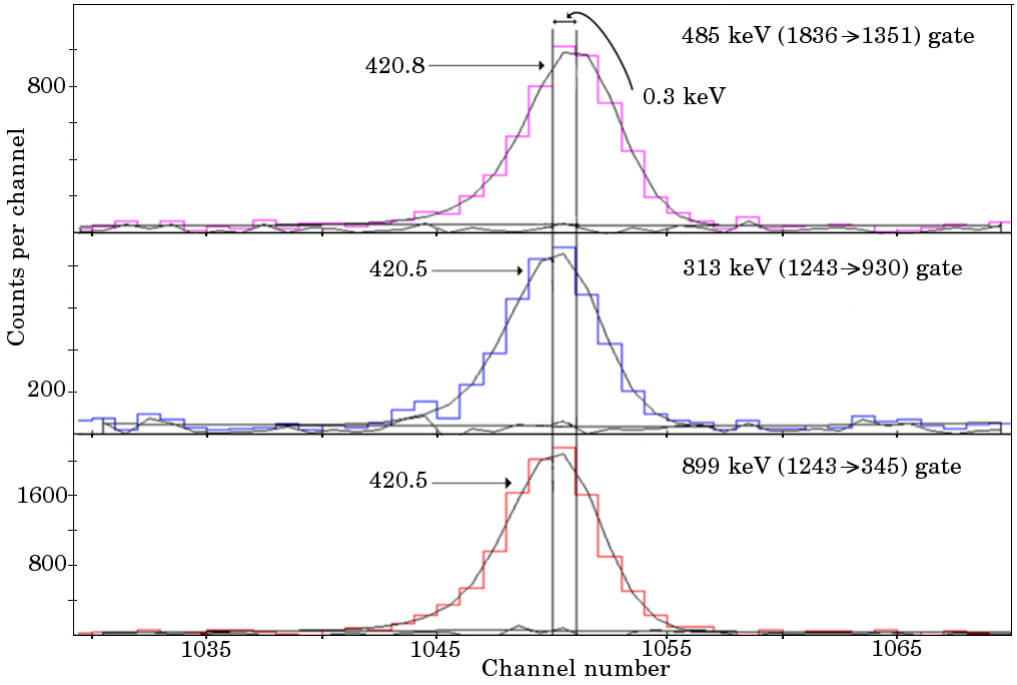

Figure 43: The 421 keV line is shown in the 485 (1836.2→1351.4), 313 (1243.2→930.4) and 899 keV (1243.2→344.6) gated spectra. The centroid shift of the 421 keV in the 485 keV gated spectrum confirms visibly more than one γ ray at 421 keV.

level.

The 484.7 keV ($I_\gamma = 0.43(4)$) γ ray depopulates the 1836.2 keV level. The 421 keV line emerges with a considerable amount of intensity, $I_\gamma = 0.38(3)$, in both the 313 and 898 keV gated spectra. Figure 43 shows evidence for two different transitions at this energy. A centroid shift for the 421 keV line in the 484 keV gated spectrum is observed, when compared with the other two spectra.

6.1.3 The 1303.7 keV level

Aguer *et al.* have previously proposed two different levels around 1303.6 and 1304.9 keV. That study proposed the 1303.6 keV level has a spin-parity of either 2^- or 3^-. On the other hand, Zolnowski *et al.* proposed that this level is 3^-. In the former study, a γ ray at 507.4 keV has been identified as feeding the 4_g^+ level at 797.5 keV. The statistics might have prevented them from resolving a closely-located peak to the 511 keV annihilation peak. Hence, they proposed that the 1304.8 keV level is a single level.

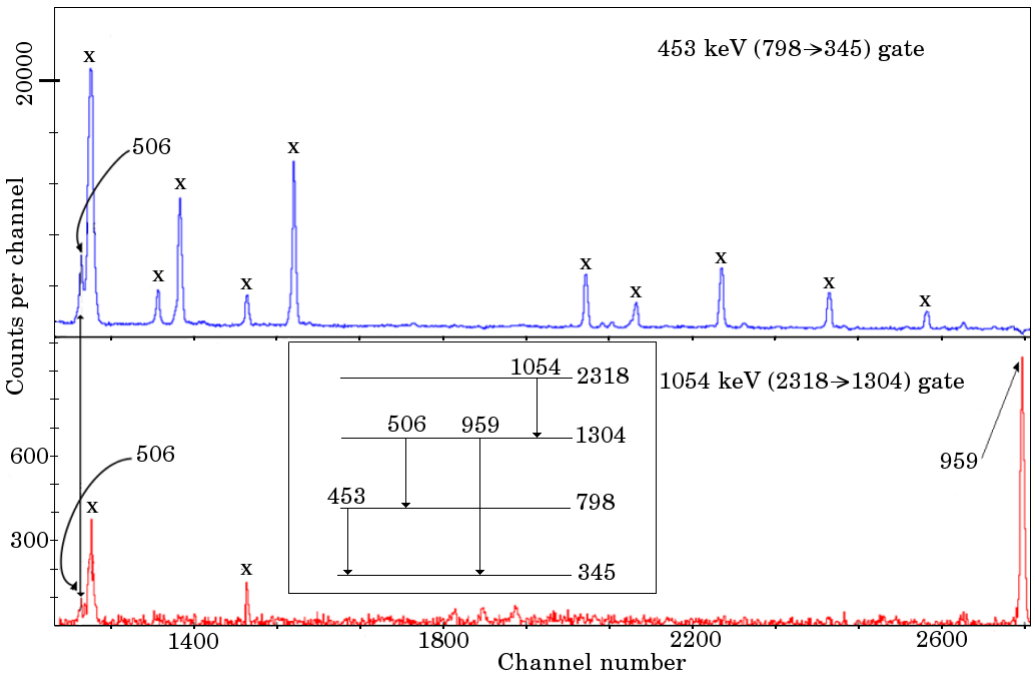

Figure 44: The 506 keV (1303.7→797.5) line in the 453 and 1054 keV gated spectra coincide perfectly. Both 506 and 959 keV γ rays depopulate the 1303.7 keV level. The lines represented with $\times$ are transitions which are not of interest.

Our study indicates that the aformentioned transition is actually a 506.3 keV (I_γ = 0.56(5)) γ ray and it depopulates the 3^- level at 1303.7 keV. The 959.1 keV ($I_\gamma = 11.0(4)$) γ ray is the strongest depopulating this level and feeding 2^+_g level, on the orther hand the 1054.3 keV ($I_\gamma = 0.38(3)$) γ ray is a strong one feeding the 1303.7 keV level. In the 1054 keV gated spectrum, the appearance of a 506.3 keV line along with a 959.1 keV line in the same gate provides sufficient coincidence information that supports the 506.3 and 959.1 keV γ rays depopulating the same level, see Figure 44. The non-existence of a previously reported 507.4 keV γ ray out of the 1304.8 keV level results in the removal of the 1304.8 keV level from the scheme. The E1 multipolarity [1] and the transitions to the 2^+_g and 4^+_g levels suggest the 3^- assignment for the level.

6.1.4 The 1380.5 keV level

This 1380.5 keV level has also been proposed as a new level by Aguer *et al.* even though Zolnowski *et al.* failed to observe it. Three γ rays are observed in our study to depopulate

the level, a 160.1 ($I_\gamma = 0.059(6)$) keV transition to the 2^+_β level, a 450.0 keV ($I_\gamma = 0.63(5)$) transition to the 2^+_γ level, and a 1036.4 keV ($I_\gamma = 0.119(13)$) transition to the 2^+_g level. Aguer *et al.* identified the second transition as 451.5 keV with an intensity of $I_\gamma < 0.15$. The measured intensity in our study is notably higher compared with that of the Aguer *et al.* study. The closeness of the γ ray to the strong 452.9 keV line in the spectrum might have resulted in them failing to find the exact energy of the transition. Our study successfully separates the 450.0 and 452.9 keV γ rays. The level has an energy of 1380.5 keV. The strongest γ-ray feeding the level is 330.0 keV ($I_\gamma = 0.057(5)$). Figure 45 confirms the existence of a previously unobserved weak 1036.4 keV transition to the 2^+_g level. The γ-ray transitions to only 2^+ levels and the expected structure suggest a possible 0^+ assignment for the level.

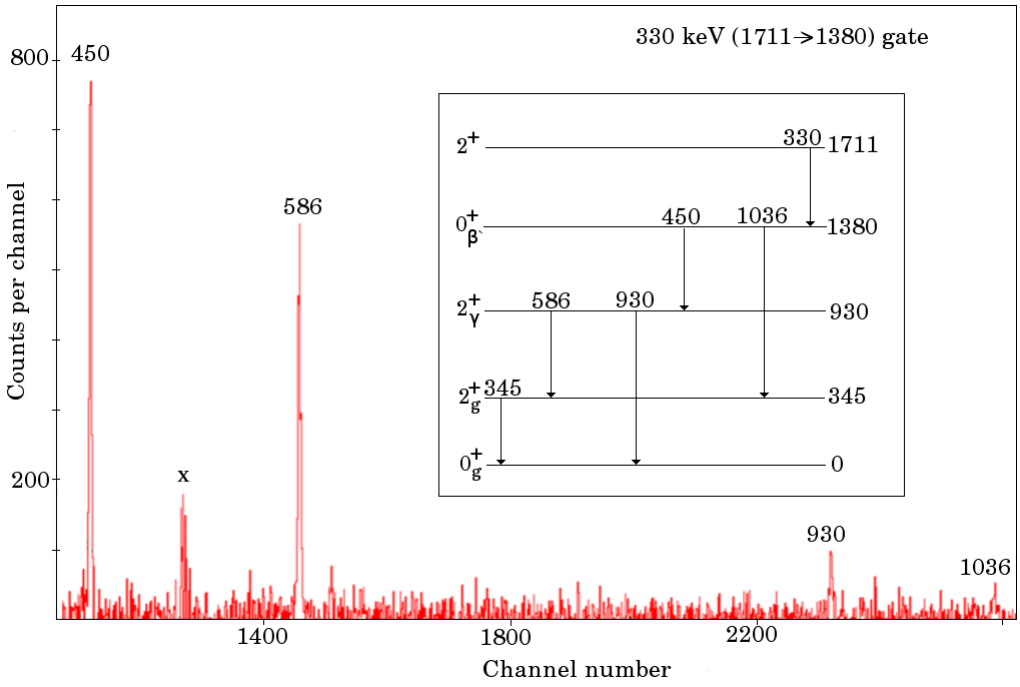

Figure 45: The 1036.4 and 450.0 keV lines are shown in the 330 keV gated spectrum. The 450.0 keV γ ray feeds the 2^+_γ level, and is in coincidence with 585.9 and 930.6 keV lines. The 1036.4 keV γ ray directly feeds the 2^+_g level. The annihilation peak is represented with $\times$.

6.1.5 The 1406.1 keV level

Zolnowski *et al.* have proposed that the 1406.1 keV level is a 2^+ level due to a strong 1405.0(5) keV transition, with intensity $I_\gamma = 0.5(2)$, to the 0^+_g level. However, our study has not observed this transition, as shown in the 430 keV gated spectrum in Figure 46. The 430 keV ($I_\gamma = 0.162(13)$) γ ray is the strongest transition feeding the level. The expected location and the intensity of 1406 keV line in the spectrum is shown with a dashed peak. The 1406 keV line in the spectrum is missing: and the expected intensity is not observed. The lack of a strong 1406 keV transition to the 0^+ ground level eliminates the certainty of this level having 2^+ spin-parity.

Our study confirms another 1404.7 keV ($I_\gamma = 0.344(28)$) γ ray feeding the 4^+_g level at 797.5 keV, as shown in the Figure 47. It directly feeds the 4^+_g level at 797.5 keV.

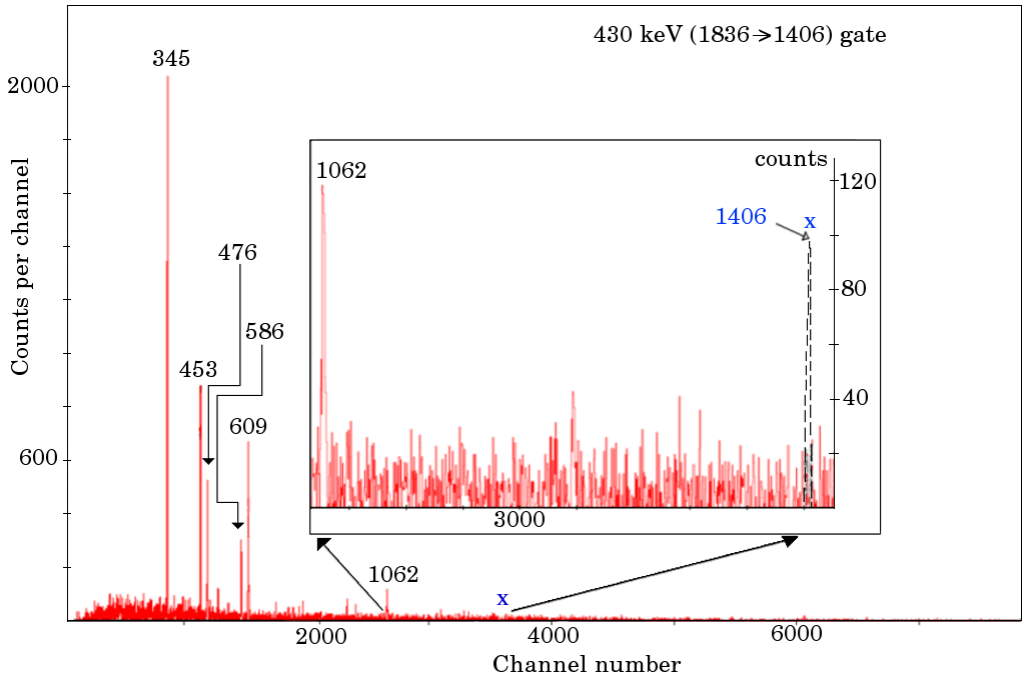

Figure 46: The expected location and the expected intensity of the 1406 keV line in the 430 keV (1836.2→1406.1) gated spectrum is shown with × and a dashed peak, respectively. The 475.6, 608.7 and 1061.6 keV transitions depopulate the 1406.1 keV level.

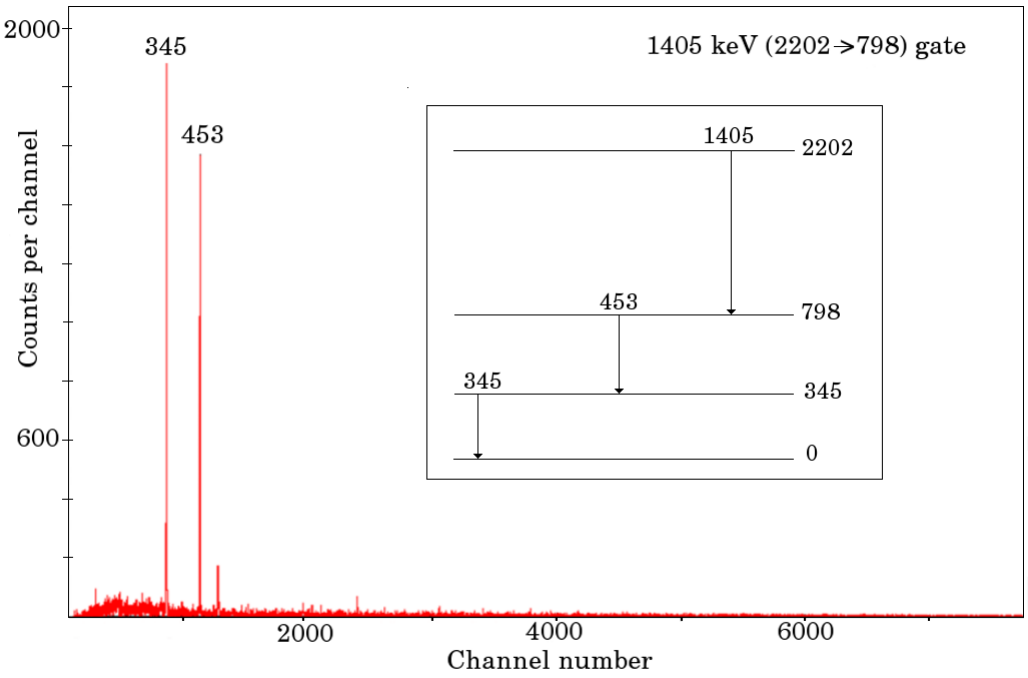

Figure 47: The 1405 keV gated spectrum shows the coincidence relation of the 1404.7 keV (2202.2→797.5) transition. The γ ray directly feeds the 4_g^+ level at 797.5 keV.

The usual procedure to test the statistical significance of a γ ray is setting an upper limit for the intensity. The existence of a direct transition to the 0_g^+ from the 1406.1 keV level can be tested by the method of Currie [55] which can be used to evaluate whether or not there is a γ ray present, see reference [49]. The method is applied simply by determining two functions, L_c (critical level) and if necessary an L_u (upper level). The critical level is defined as

$$L_c = 1.645[\sqrt{Q(1+\frac{u}{2t})}] \tag{33}$$

where u is the number of peak channesl, $u = FWHM + 1$, and 2t is the number of background channels set near the peak with the corresponding areas P and B, respectively, and $Q = uB/2t$ can be defined to scale the background counts to the peak counts. If the net area, A=P-Q, of the corresponding peak is greater than the critical level, it is safe to report the γ ray; if not, an L_u should be determined. The upper level is defined as

$$L_u = A + 1.645[\sqrt{A + Q(1 + \frac{u}{2t}}] \quad (34)$$

The change in the spin assignment of this level will drastically change the level structure. Thus a careful analysis of the 1405.0(5) keV transition 0.5(2) has to be carried out. The method described above is applied to the γ ray in the 430 keV gated spectrum to evaluate the statistical significance of the peak area. Several attempts to apply the procedure failed to give satisfactory results due to the weakness of the γ ray in the spectrum.

6.1.6 The 1476 keV level

This level is neither confirmed in our study nor in previous β-decay studies. The only assignment of this level in ^{156}Er was made by *Azgui* [56] in a heavy-ion evaporation study as a 5^- level. The systematics of other N=88 isotones with this assignment are not consistent. The 5^- spin-parity assignment is more likely for the 1611.9 keV level, based on the observed γ rays and the expected structure. The lack of any γ ray transitions out of the level or to the level in the present study are evidence for the non-existence of the level.

6.1.7 The 1570.6 keV level

Seven γ rays depopulate the 1570.6 keV level. The 640.0 and 640.3 keV transitions are observed to depopulate the level with intensities of 0.206(18) and 0.316(26), respectively (for further information on separating these doublets see section 6.1.1). A tentative assignment for the 1226.1 keV γ ray with an intensity of 1.40 was suggested to depopulate this level [1]. Our study confirms the existence of the transition firmly. A 640.3 keV transition to the 0^+_β level and a 773.2 keV transition to the 4^+_g level secure this level having 2^+ spin-parity. A 640.3 keV E0 contribution to the 2^+_γ [1] level and transitions to the 0^+_β and 2^+_β levels are notable.

6.1.8 The 1630.6 keV level

A previous (2^-) spin-parity assignment [1] does not seem probable based on the γ-ray transitions out of the level. The level energy is calculated using the corresponding Ritz

combinations along with the uncertainties of four γ rays. The placements and intensities of the 699.9 (1630.6$\rightarrow 2^+_\gamma$) and 1286.0 keV (1630.6$\rightarrow 2^+_g$) γ rays are in agreement with the reported values. However, the level energy calculated from the 279.6 keV ($I_\gamma = 0.0212(25)$) transition to the 1351.4 keV level and 327.2 keV ($I_\gamma = 0.065(6)$) transition to the 1303.7 keV 3^- level differs slightly from the level energy calculated using the 699.9 and 1286.0 keV γ rays. If the 279.6 and 327.2 keV transitions are assumed to depopulate the same level, the energy difference would be ~ 0.4 keV. If only the 279.6 keV γ ray depopulates one level and the other three γ rays depopulate the other level, the difference would be ~ 0.5 keV. If four of them are assumed to depopulate the same level, the level energy is calculated to be 1630.6 keV. The 1630.6 keV is used as a basis for Ritz combinations of γ rays feeding the level. Either the previous (2^-) spin-parity assignment is erroneous or a potential second level very close in energy should be considered.

6.1.9 The 1663.7 keV level

The 1663.7 keV level was proposed in the study of Zolnowski *et al.*. However, an unplaced 1663.9(4) keV γ ray with an intensity of $I_\gamma = 1.3(3)$ was reported by them along with the 1663.7 keV level. A 5^+ assignment was made in this study, yet reference [1] reports this level tentatively as (5^+). One γ ray, 866.1 keV is assigned to the decay of this level in the same reference. We add ten more. Eleven γ rays are found to depopulate the level in total. The existence of γ ray transitions to many 2^+ and 0^+ levels eliminates 5^+ spin-parity for this level. The level probably has a 2^+ spin-parity if there is not a possible doublet close in energy. If the previous spin-parity assignment is assumed to be true, a second level should be sought around this energy. If not, the only possible spin-parity assignment is 2^+, on the basis of transitions out of the level.

The 1663.9 keV ($I_\gamma = 1.03(8)$) γ ray to the 0^+_g level and 866.1 keV ($I_\gamma = 0.52(4)$) γ ray to the 4^+_g level, as shown in the Figure 48, indicate that the previous 5^+ spin-parity assignment is not correct. The strong 959 keV line in both the 358 and 407 keV gates in Figure 48, can be attributed to the 360.2 and 407.1 keV γ rays which are in coincidence with the 959.1 keV transition as indicated. The 406.6 keV γ ray feeds the 1663.9 keV level,

and 407 keV γ ray feeds the 1303.7 keV level, as indicated in Figure 49. A 2^+ spin-parity assignment, or the existence of second level at this energy are highly likely for the given coincidence results. A second 1664.0 keV ($I_\gamma = 0.50(4)$) transition to the 4^+_g level is also identified.

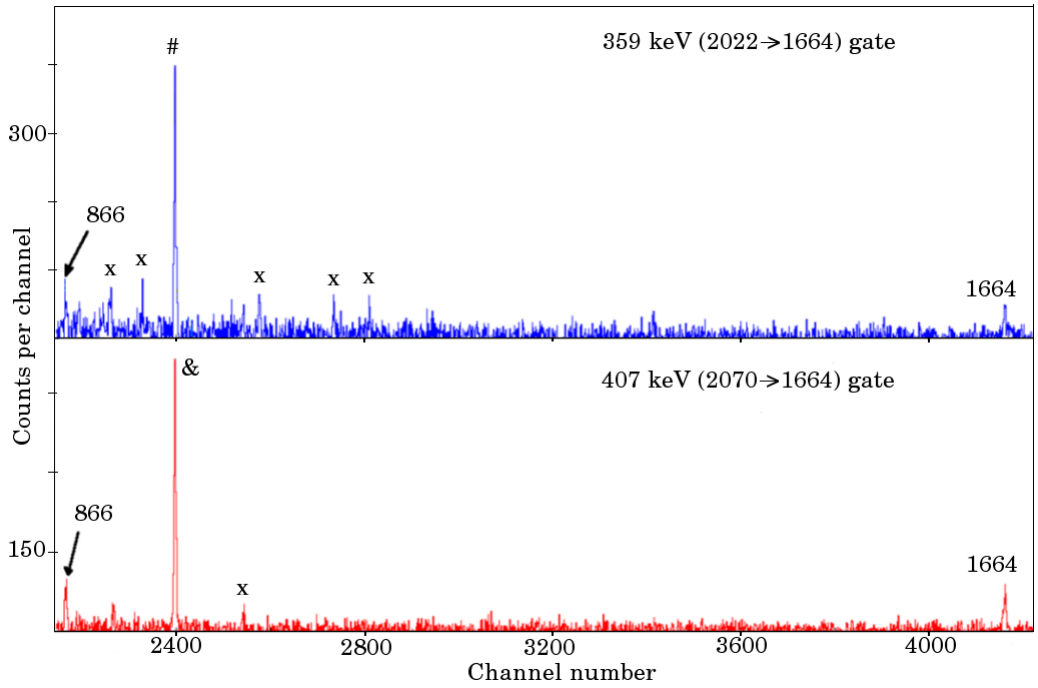

Figure 48: The 358.6 (2022.4→1663.9) and 406.6 keV (2070.3→1663.9) gated spectra. The 1663.9 (1663.9→0^+_g) and 866.1 keV (1663.9→4^+_g) lines in both spectra contradict the 5^+ spin-parity assignment. The lines which are represented by × are contaminant transitions, by # and & are the 959.1 keV γ ray in coincidence with 360.2, and 407.1 keV γ rays, respectively.

The strong 420.5 keV ($I_\gamma = 0.38(3)$) γ ray feeding the level at 1243.2 keV must be examined very carefully. The 1243.2 keV level is identified as 3^+_γ level, then the 1663.9 keV level should mostly likely be 5^+_γ. However, this contradicts with the confirmed γ-ray decays to the lower levels. .

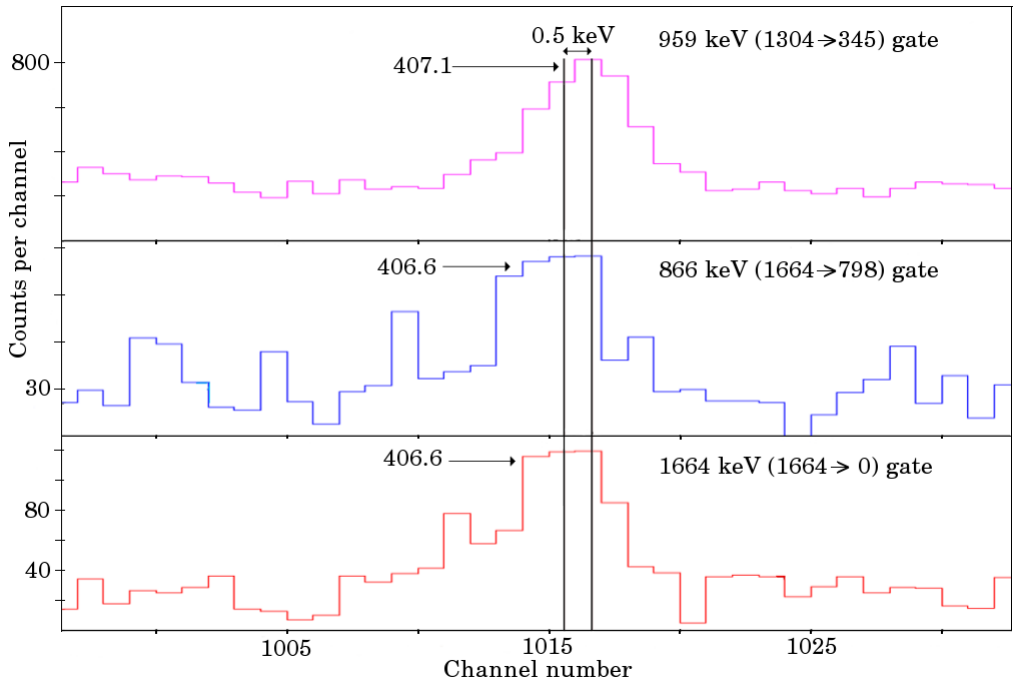

Figure 49: The centroid shift of the 407 keV line in the 959 keV γ-ray gated spectrum with respect to the 866 and 1664 keV γ-ray gated spectra is remarkable. This spectrum is shown to avoid a possible misassignment of a strong 959 keV γ-ray line in the 407 keV γ-ray gated spectrum in the previous figure.

6.1.10 The 1710.7 keV level

Zolnowski *et al.* assigned this level as a 4^+ level. However, the evaluation in reference [1] is a tentative (4^+) assignment. In our study, six γ rays are observed out of the level, a 330.0 ($I_\gamma = 0.057(5)$), a 407.1 ($I_\gamma = 0.089(8)$), a 467.4 ($I_\gamma = 0.0300(27)$), a 489.7 ($I_\gamma = 0.031(4)$), a 913.1 ($I_\gamma = 0.285(23)$), and a 1366.1 keV ($I_\gamma = 1.81(15)$) transition. The spin-parity assignments of the final levels populated by these γ rays extend from 0^+ to 4^+. It is necessary to assign the level as a 2^+ level.

6.1.11 The 1759.5 keV level

Two γ-rays are observed to depopulate this newly established level, a 241.73 ($I_\gamma = 0.0179(22)$) and a 538.6 keV ($I_\gamma = 0.058(6)$) transition. The spin-parities of final levels of the corresponding γ rays allow the level to have 0^+, 1^-, $2^\pm$ or 3^- spin-parity assignments. A transition to an octupole level is of note.

6.1.12 The 1836.2 keV level

The 484.7 keV ($I_\gamma = 0.43(4)$) transition from this level feeds the 1351.4 keV level. A placement was reported by Aguer *et al.*, yet the same assignment was converted to a tentative assignment in the reference [1]. The 420, 553 and 1007 keV gated spectra in Figure 50 provide evidence for a direct transition from the 1836.2 to the 1351.4 keV levels. The high intensity of the 484.7 keV line has to be taken into account in accordance with the band assignments.

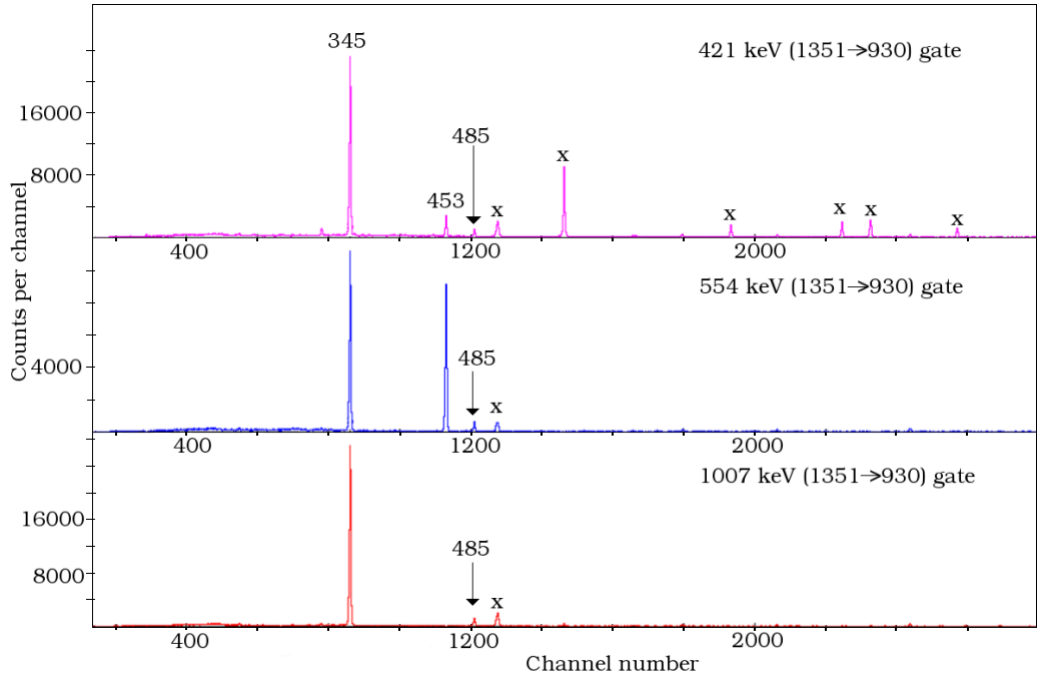

Figure 50: The 484.7 keV line is shown in a composite spectrum formed by 421 (1351.4→930.4), 554 (1351.4→797.5) and 1007 keV (1351.4→344.6) transitions. The existence of the 484.7 keV line in all gates provides the correct placement of the corresponding γ ray out of the 1836.2 keV level. The γ rays represented by $\times$ are not of interest.

6.1.13 The 1886.3 keV level

Only two γ-rays are observed out of the 1886.3 keV level, a 480.4 ($I_\gamma = 0.0121(19)$) and a 545.5 keV ($I_\gamma = 0.0066(8)$) transition. A transition to a high-spin level, 6^+_g, out of the level supports this level being also a high-spin level. The most probable assignment is 6^+ due to the expected band structure of the β band.

6.1.14 The 1909.5 keV level

The previous (3^-) assignment made in reference [1] is erroneous due to a newly observed 1909.9 keV transition from this level to the 0_g^+ level. A direct transition to the 0_g^+ level from this particular level is detected by comparing the peak intensities with the nearby γ-rays in the coincidence spectrum. Intensity differences are observed in the correponding peak; the corresponding line in the spectrum emerged with a high intensity.

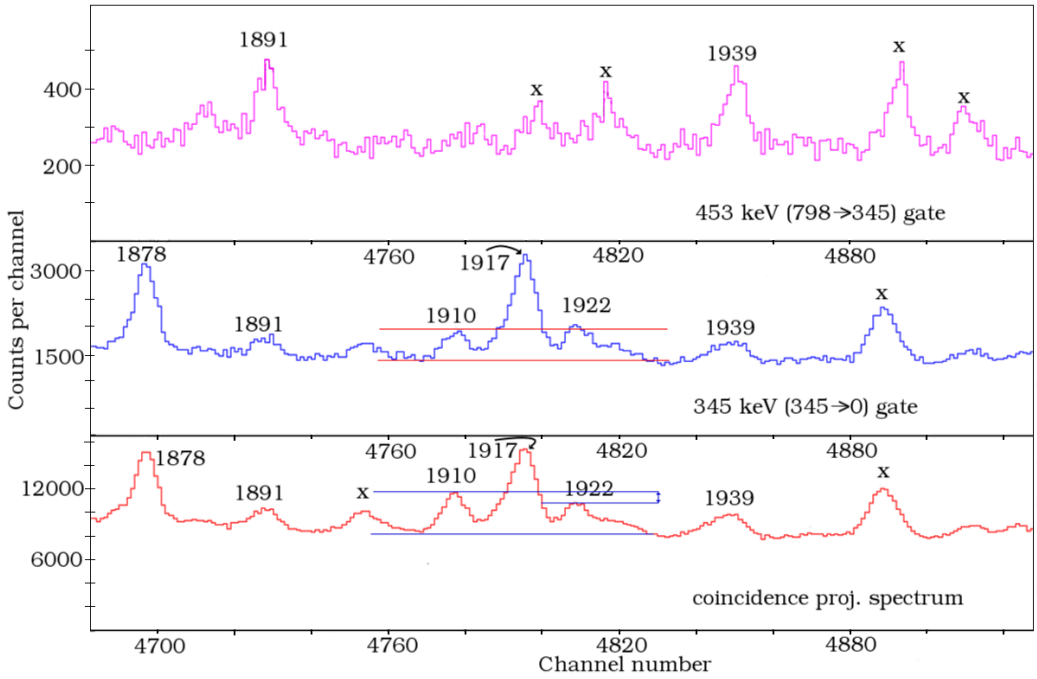

Figure 51: The composite spectrum of the coincidence-projection spectrum along with the 345 and 453 keV γ-ray gated spectra. The 1878, 1891, 1917, 1923, and 1939 keV lines are shown to make a similar comparison with respect to the intensities. Note the high intensity of the 1909.9 keV line. Due to the reasons (explained in the text), the 1909.9 keV line is a transition from the 1909.9 keV level to the 0_g^+ level. The lines which are not of interest are shown with $\times$.

The easiest way to confirm that there is a coincident γ ray is to see it in a gate from above. Only two weak γ rays feed the level, and 1909.9 keV transition lies in a region of low efficiency. As a result, it is not observed in the gates from above. Secondly, the ^{156}Dy and ^{156}Tm transitions are checked to see if a γ ray belonging to these nuclei is in coincidence with 1909.9 keV transition; none were found. It is found that the 1909.9 keV γ ray is one

of the ^{156}Er transitions due to the non-existence of any coincident γ ray to the 1909.9 keV transition in the ^{156}Dy and ^{156}Tm and the low Q-value of the corresponding nuclei. At the same time all important energy gates in ^{156}Er are checked to see whether the 1909.9 keV γ ray is in coincidence with any other γ ray; and none was found. It is therefore a direct transition to the 0^+_g level, see the Figure 51. (The same procedure is carried out for all levels not to miss any direct transition to the 0^+_g level.)

Three γ rays are found to depopulate the 1909.5 keV level, a 978.8 ($I_\gamma = 0.046(5)$), a 1564.9 ($I_\gamma = 1.75(15)$) and a 1909.9 keV ($I_\gamma = 0.173(16)$) transition. A reported 557.9 keV transition out of the level [1] is not confirmed. The γ rays to only 0^+ and 2^+ levels limit spin-parity and band assignments.

6.1.15 The 2249.9 keV level

A misjudgment of a strong 898.7 keV transition in the 420 keV gated spectrum led Auger *et al*. to propose this level to be a new level. Referring back to the Figure 42, it has been found to be two different transitions: a 420.8 (1351.4→930.4) and a 420.5 keV (1663.7→1243.2) transition. No evidence is found for a 898.7 keV transition feeding the 1351.4 keV level. It is unlikely that the 898.7 keV transition connects the 2249.9 keV level with 1351.4 keV level, despite the fact that it is seen in the 420 keV gated spectrum.

6.1.16 A secondary result of the spectrum analysis

During the analysis, a few strong low-lying ^{140}Nd γ-ray transitions are observed. The coincidence analysis indicates the existence of three γ rays, at 419.6, 773.7 and 1028.2 keV. They are not in coincidence with any of the γ rays from ^{156}Er. The 773.7 keV γ ray is associated with $2^+ \rightarrow 0^+$, the 1028.2 keV with $4^+ \rightarrow 2^+$, and 419.6 keV γ ray with $7^- \rightarrow 4^+$ in the ^{140}Nd. The coincidence gating technique explicitly shows the coincidence relation of these γ rays, shown in Figure 52. However, the placement and the spins are taken from the reference [57].

The existence of a few low-energy γ rays from ^{140}Nd in the projection spectrum is unexpected. This resulted from the β decay of ^{140}Pm to ^{140}Nd. The nucleus ^{140}Pm has 16 nucleons lower than A=156 nuclei. The chemical reaction of ^{140}Pm with the ^{16}O in the ion source to produce a monoxide of ^{140}Pm probably occurred during the experiment. Its β decay to ^{140}Nd is observed in this experiment due to its short half life ($T_{\frac{1}{2}} = 9.2$ s).

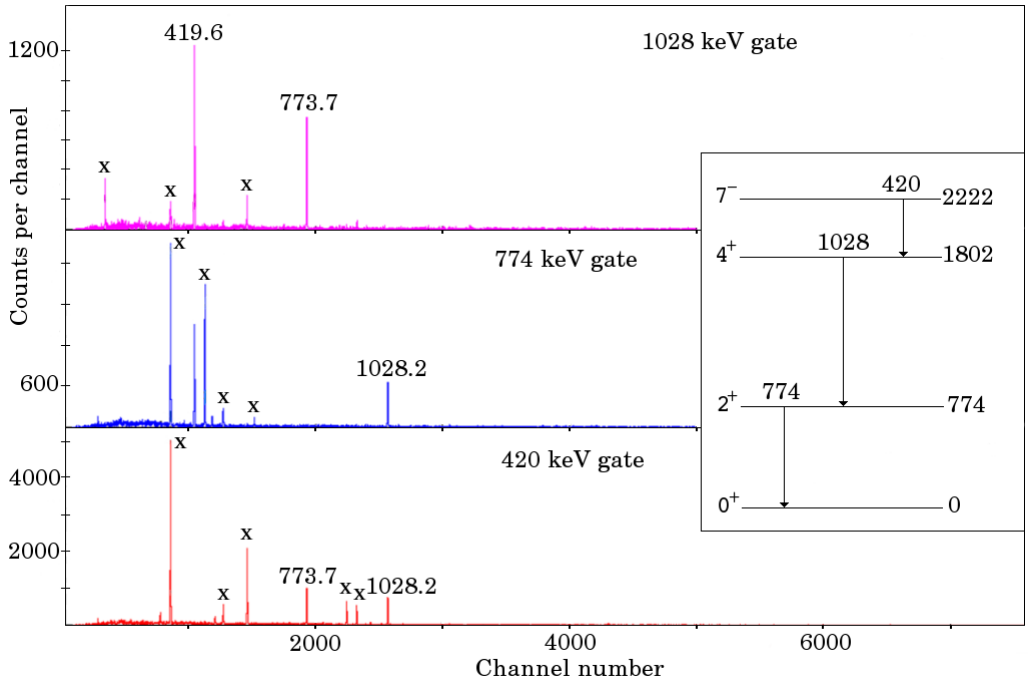

Figure 52: The 420, 774 and 1028 keV gated spectra are shown to illustrate the coincidence relations of the three γ rays. The spin-parity and the placement of γ rays can be found in reference [57]. The γ rays represented with $\times$ in these spectra are nearby transitions to the γ rays corresponding to ^{156}Er.

6.2 B(E2) Values

The reduced transition probabilities of electric quadrupole (B(E2) values) for nuclei can provide essential information about the structure of a nucleus. The comparison of the structure of the nucleus can be done comprehensibly due to the specific character of B(E2) values. The expectation is that the B(E2) values are strong in intraband transitions. In the same band even a weak γ ray corresponds to a high transition probability because of the E_γ^5 energy dependence of B(E2) values, see Equation 19 and 21. Secondly, the transitions to ground-state band members are usually preferred because they involve the annihilation

of just one phonon. The transition probabilities to other levels are not favored due to the requirement of creation and annihilation of phonons. However, the transitions in N=88 isotones do not totally obey these observations.

The half lives of nuclear levels are needed to determine the B(E2) values absolutely. Our study does not involve determining level half lives. Even the relative B(E2) values of transitions can provide crucial information about band assignments. Correct band assignments can be made for levels using relative B(E2) values. In Table 3, the relative B(E2) values are listed assuming that the γ ray carries pure E2 character. In the literature, there are not so many measured multipolarities for transitions in ^{156}Er. If a mixture of the multipolarities, i.e., (M1+E2), exists for a particular transition, it is not known.

Table 3: List of relative B(E2) values for transitions observed in this work. The relative intensities, I_{r_1}, normalized to ($I_{344.6}$=100) and the relative intensities of γ rays depopulating a particular level, I_{r_2}, normalized (I_γ=100) to the strongest γ ray out of the level are shown with the relative B(E2) values (normalized to the strongest B(E2) out of the level) in order to provide possible band assignments. The listing extends to the 2200 keV level.

E_i	E_γ	I_{r_1}	I_{r_2}	$B(E2)$
344.59	344.59	100	100	100
797.53	452.94	20.1	100	100
929.99	585.40	1.70	100	100
930.44	585.85	15.1	100	100
	930.64	5.82	38.6	3.82
1220.89	290.42	0.068	2.21	17.93
	290.84	0.38	12.4	100
	423.43	0.51	16.5	20.24
	876.28	2.93	95	3.08
	1220.90	3.08	100	0.62
1243.24	312.78	0.219	14.9	100

Table 3 – continued from previous page

E_i	E_γ	I_{r_1}	I_{r_2}	$B(E2)$
	446.19	0.0218	1.49	1.69
	898.65	1.46	100	3.42
1303.68	506.30	0.56	5.1	100
	959.08	11.0	100	80.2
1340.81	543.28	0.295	100	100
1351.42	420.77	1.43	35.5	100
	553.89	1.09	27.1	19.34
	1006.89	4.02	100	3.59
1380.46	160.09	0.059	9.3	100
	450.01	0.63	100	6.13
	1036.40	0.119	18.8	0.07
1406.14	475.61	0.98	62	100
	608.67	1.59	100	47.18
	1061.64	0.56	35	1.03
1517.95	1173.36	0.88	40	100
	1518.01	2.21	100	69.65
1546.64	325.90	0.253	23.6	100
	615.81	0.057	5.3	0.93
	749.13	0.66	61	4.05
	1202.02	1.07	100	0.62
1570.63	219.47	0.042	2.79	100
	327.57	0.0091	0.61	2.93
	349.93	0.358	23.8	82.79
	639.99	0.206	13.7	2.33
	640.29	0.316	21.0	3.57
	773.20	0.312	20.7	1.37
	1226.00	1.50	100	0.66

Table 3 – continued from previous page

E_i	E_γ	I_{r_1}	I_{r_2}	$B(E2)$
1611.89	270.99	0.0098	1.21	100
	308.5	0.0043	0.53	22.98
	814.37	0.81	100	33.82
1630.56	279.56	0.0212	0.65	70.95
	327.18	0.065	2.02	100
	699.87	1.46	45	49.73
	1285.99	3.24	100	5.27
1663.73	257.50	0.031	6.0	94.34
	283.25	0.0094	1.81	17.69
	312.47	0.057	11.0	65.85
	360.18	0.100	19.3	53.62
	420.52	0.38	74	100
	442.89	0.101	19.4	20.3
	732.85	0.030	5.7	0.48
	733.38	0.053	10.2	4.13
	866.13	0.52	100	3.66
	1319.42	0.125	24.1	0.11
	1663.92	1.03	198	0.28
1710.65	330.03	0.057	3.14	100
	407.07	0.089	4.9	54.87
	467.43	0.0300	1.66	9.25
	489.70	0.031	1.74	7.68
	913.12	0.285	15.8	3.09
	1366.07	1.81	100	2.62
1759.53	241.73	0.0179	31	100
	538.60	0.058	100	5.94
1814.74	1017.22	1.26	100	100

Table 3 – continued from previous page

E_i	E_γ	I_{r_1}	I_{r_2}	$B(E2)$
1836.16	430.06	0.162	37	68.17
	484.68	0.43	100	100
	494.97	0.030	6.9	6.22
	905.83	0.179	41	1.81
	1038.49	0.170	39	0.87
1860.61	230.53	0.0086	0.67	100
	556.89	0.075	5.8	10.53
	929.98	1.25	97	13.6
	1063.14	0.323	25.0	1.8
	1516.06	1.29	100	1.22
1886.34	480.40	0.0121	100	100
	545.48	0.0066	55	29
1909.46	978.80	0.046	2.6	27.24
	1564.88	1.75	100	100
	1909.9	0.173	9.9	3.64
1917.86	287.33	0.0153	3.3	21.68
	346.88	0.181	39	100
	371.22	0.030	6.5	11.9
	614.25	0.0218	4.7	0.69
	697.05	0.112	24.1	1.89
	987.12	0.130	27.9	0.38
	1120.47	0.281	60	0.44
	1573.33	0.46	100	0.13
1939.18	1008.74	0.152	100	100
1957.90	387.30	0.054	20.7	100
	411.34	0.045	17.6	62.72
	551.47	0.038	14.6	12

Table 3 – continued from previous page

E_i	E_γ	I_{r_1}	I_{r_2}	$B(E2)$
	616.86	0.0073	2.8	1.33
	736.95	0.024	9.2	1.77
	1027.07	0.068	26.1	0.96
	1160.48	0.259	100	2
2014.55	384.04	0.0132	0.83	100
	496.53	0.0153	0.96	31.97
	662.91	0.051	3.2	25.37
	1083.90	0.306	19.2	12.92
	1670.00	1.59	100	7.76
2016.54	469.88	0.0157	8.1	100
	635.42	0.0094	4.9	13.27
	665.28	0.031	16.0	34.55
	712.88	0.115	60	91.42
	795.79	0.036	18.5	16.29
	1086.07	0.155	81	15.04
	2016.7	0.193	100	0.84
2022.35	312.36	0.0124	3.2	56.67
	358.60	0.044	11.4	100
	410.71	0.0071	1.85	8.26
	475.77	0.0273	7.1	15.16
	616.00	0.036	9.4	5.52
	1224.84	0.171	45	0.84
	1677.67	0.38	100	0.39
2070.33	406.60	0.063	28.5	100
	500.02	0.0170	7.6	0.02
	718.81	0.122	55	11.16
	827.17	0.088	40	3.98

Table 3 – continued from previous page

E_i	E_γ	I_{r_1}	I_{r_2}	$B(E2)$
	1139.64	0.053	24	0.48
	2070.8	0.223	100	0.1
2082.94	731.43	0.025	5.9	100
	742.00	0.0237	5.5	87.19
	779.24	0.028	6.5	80.54
	861.97	0.035	8.2	61.24
	1285.48	0.068	16.0	16.08
	1738.54	0.43	100	22.28
2105.43	474.59	0.0230	4.3	100
	724.58	0.0160	3.0	8.39
	884.25	0.040	7.5	7.77
	1174.69	0.061	11.5	2.87
	1760.87	0.53	100	3.31
2132.94	586.74	0.034	27.2	100
	911.70	0.124	100	40.54
2169.82	557.88	0.0141	1.42	100
	865.86	0.033	3.4	26.41
	1372.33	0.230	23.2	18.15
	1825.3	0.99	100	18.79
2174.67	562.69	0.0192	2.53	100
	953.91	0.070	9.2	26.09
	1830.5	0.76	100	10.86
2176.88	546.10	0.039	22.3	100
	564.99	0.0283	16.0	60.67
	770.73	0.140	79	63.39
	825.48	0.176	100	56.89
	873.23	0.081	46	19.77

Table 3 – continued from previous page

E_i	E_γ	I_{r_1}	I_{r_2}	$B(E2)$
	1379.44	0.070	40	1.74
2199.35	488.80	0.0170	4.2	100
	847.88	0.032	8.0	12.11
	978.61	0.048	11.8	8.75
	1268.74	0.211	52	10.52
	1854.9	0.41	100	3.04

CHAPTER VII

DISCUSSION

7.1 Band Assignments

The band assignments along with the underlying model descriptions are explained in the subsequent sections starting from the ground-state band. The possible band assignments are exhibited up to 2000 keV excitation energy by assuming the bands obey rotational spacing, see Figure 53.

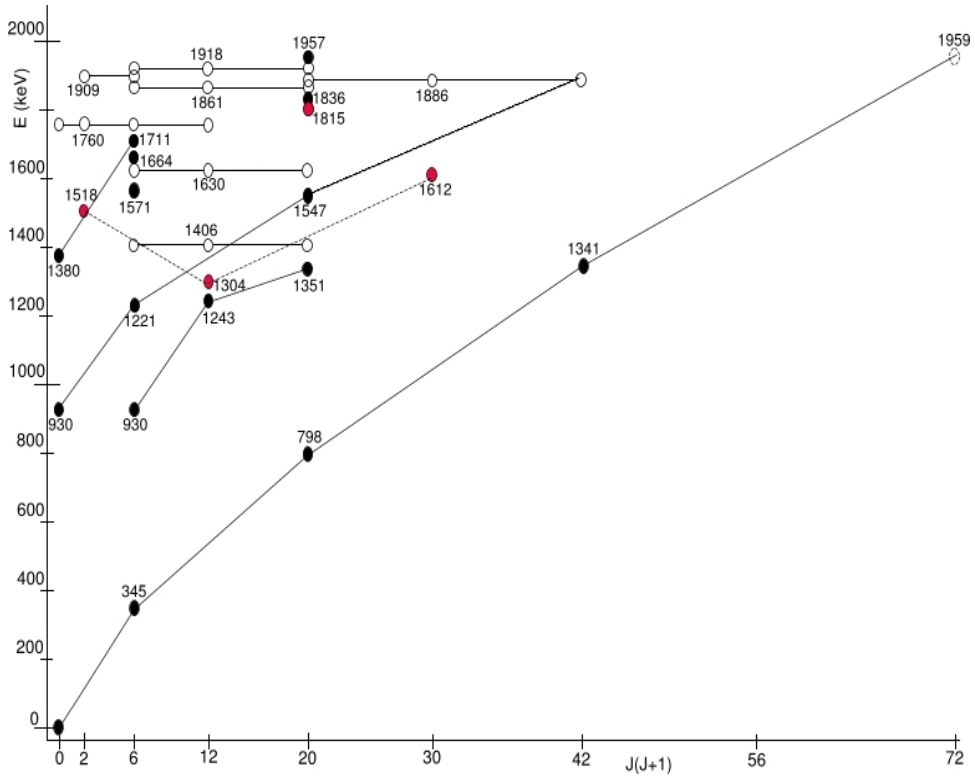

Figure 53: The band assignments of low-lying levels in ^{156}Er are shown. The uncertain spin assignments of levels are connected with thin horizontal lines and the levels are left as open circles. If levels are assigned to a particular band, they are connected with a "heavy" solid line within the band and the circles are colored. The negative-parity band is connected with a dashed line.

The coincidence relations of γ rays played an important role in organizing the levels into bands using the reduced B(E2) values of transitions. It is not expected to have levels with spin-parities higher than 6^+ in the current study. This result is supported by the non-observation of the 8^+ level in the ground-state band. It is also unlikely to have high-energy levels carrying a spin-parity assignment greater than 4^+ due to the 2^- spin-parity of the beta-decaying parent nucleus.

7.2 Positive-Parity Bands

In the following sections, the placement of the positive-parity bands will be explained. A detailed relation for the positive-parity states with the B(E2) transition probabilities (normalized to the largest B(E2) value from the level) are shown in Figure 61.

7.2.1 The Ground-state band

The only observed members of the ground-state band in our study are the 2^+, 4^+, and 6^+ levels whereas the known (from in-beam spectroscopy) 8^+ level at 1959 keV is not observed. The spacing of the levels of the band members are similar to the neighboring N=88 isotones. The band members in Figure 53 are connected with a solid line assuming that they obey a quasi-rotational level spacing.

7.2.2 The β band

Members for the β band are deduced: 0^+ at 930.0 keV, 2^+ at 1220.9 keV, 4^+ at 1546.6 keV, and a possible 6^+ at 1886.3 keV. If the 6^+ member of the band is observed in this study, it is most likely that it would be the 1886.3 keV level, see Figure 53. The energy difference of the 6^+ and 4^+ members of the β band of N=88 isotones appear at 373, 386, 407 keV for ^{150}Sm, ^{152}Gd and ^{154}Dy, respectively. The energy difference for ^{156}Er is 340 keV if the 1886.3 keV level is assumed to be the 6^+ member of the band. It is in agreement with the energy spacings of 6^+ and 4^+ levels in the neighboring N=88 isotones. The systematics for the β bands of the neighboring N=88 isotones is illustrated in Figure 54. Because the 6^+ member of the band is not determined with certainty, this spin-parity is left open in the Figure.

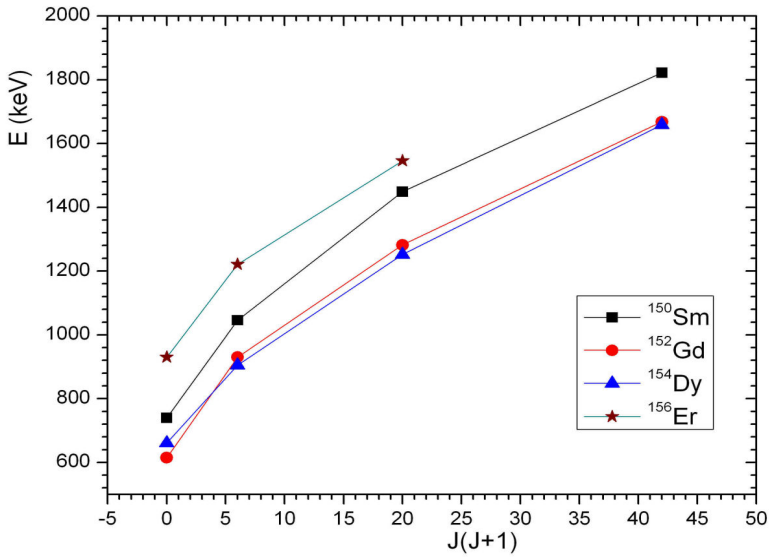

Figure 54: The β-band assignments of low-lying levels of N=88 isotones. The 6^+ band member is not displayed in the figure. It can be proposed that the expected band structure requires that the 6^+ state would be in the energy interval of 1880 keV to 1950 keV. (The data, except for ^{156}Er, are taken from *Nuclear Data Sheets* [3, 4, 5].)

The coincidence information of the β band member is shown explicitly in Figure 55. The 325.9 keV γ ray feeds the 2^+_β level at 1221 keV. The 0^+ member of the band is clearly identified in Section 6.1.1 as 930.0 keV level. The relative B(E2) values of γ rays out of the corresponding levels, shown in Table 3, exhibit the relation expected for the band members. The intense γ ray out of the 1220.9 keV level is 290.8 keV transition which has the highest B(E2) transition probability. The 325.9 keV γ-ray transition out of the 1546.6 keV has the highest B(E2) value. The E0+E2(+M1) multipolarity of 876.3 keV transition out of the 1220.9 keV level and the E0+M1+E2 multipolarity of 749.1 keV transition out of the 1546.6 keV level (multipolarities are from reference [1]) is another proof that these levels compose the same band. Additionally, the spacing between levels is in agreement with the neighboring N=88 isotones. .

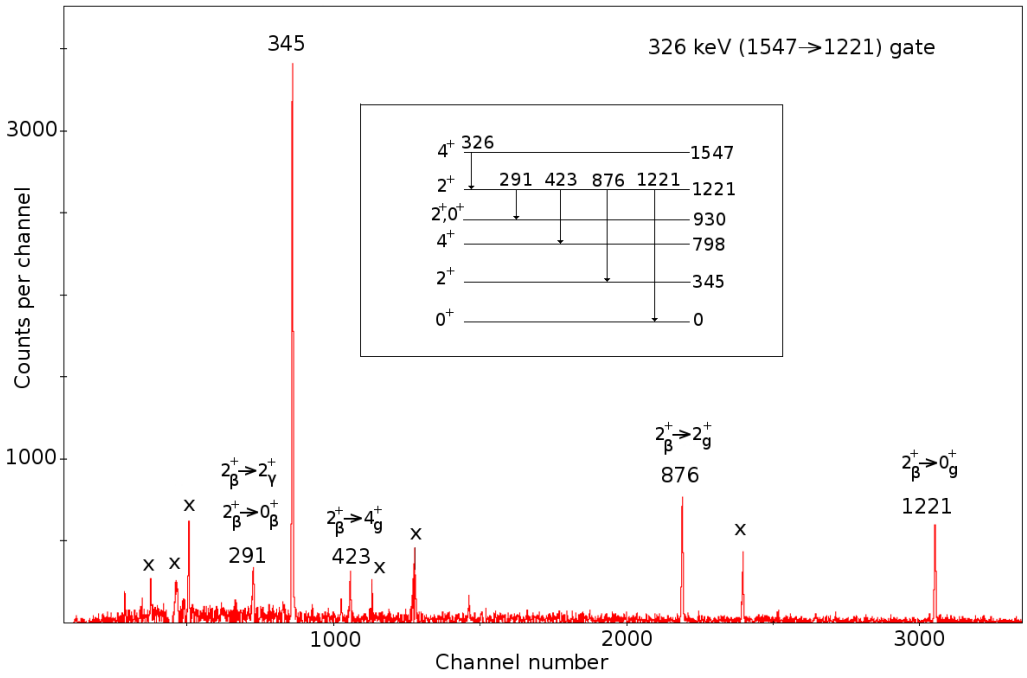

Figure 55: The 326 keV gated spectrum is shown to illustrate the coincidence relations of the β band members. The 325.9 keV γ ray connects the 4^+_β state with the 2^+_β state. Gamma rays not of interest are shown with $\times$.

7.2.3 The γ band

The collective nature of even-even nuclei supports a γ band with K=2. In ^{156}Er the band starts with a 2^+ level at 930.4 keV and continues with a 3^+ level at 1243.2 keV, a 4^+ level at 1351.4 keV, a 5^+ level possibly at 1631 keV or at 1663.7 keV (see Sections 6.1.8 and 6.1.9). In reference [22] it is proposed that the quasi-gamma band members of the N=88 isotones have energies that decrease to a minimum until ^{156}Er and exhibit an upturn for ^{158}Yb. Figure 56, showing rotational spacing, illustrates the decrease clearly.

The coincidence information of the γ band member is shown explicitly in Figure 57. The 420.5 keV γ ray feeds the 3^+_γ level at 1243 keV. Both 313 and 899 keV lines appear on the spectrum supporting the placement of the band members of the γ band. Section 6.1.1 explains the separation of the 0^+_β and 2^+_γ states at $\sim$ 930 keV. The high B(E2) transition probability of the 312.8 keV γ ray out of the 1243.2 keV level to the 930.4 keV level and the systematics seen in the neighboring nuclei support the 3^+ spin-parity assignment for

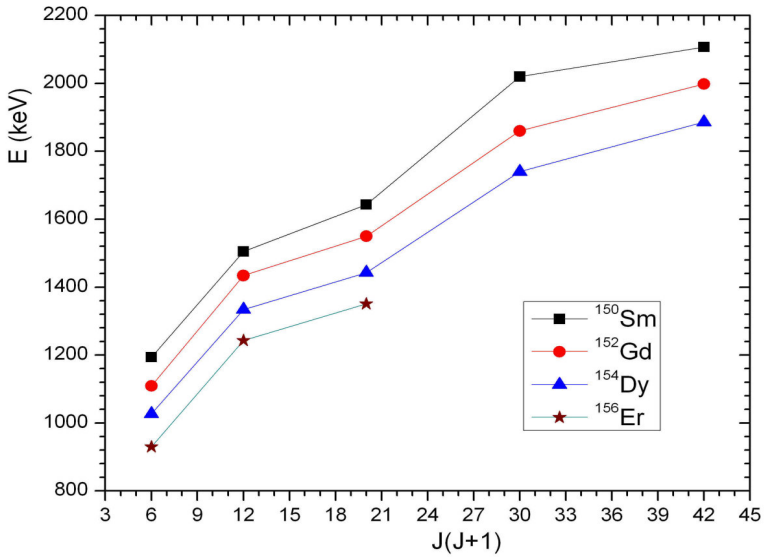

Figure 56: The γ band assignments of low-lying levels in the N=88 isotones. The 5^+ and 6^+ band members of ^{156}Er are not displayed in the figure. A possible band assignment of 5^+ is discussed in the text. The smooth quasi-rotational energy spacing in the bands is remarkable. (The data, except for ^{156}Er, are taken from *Nuclear Data Sheets* [3, 4, 5].)

the 1243.2 keV level. Possible 4^+ band members are the 1351.4 keV and 1406.1 keV levels due to the transitions to the 4^+ and 2^+ states and the high relative B(E2) values to the 2^+_γ level. However, the rotational band spacing between the 4^+ (if it is assumed to be the 1351.4 keV level) and 3^+ band members is in agreement with the neighboring isotones. The expected band structure confirms the 1351.4 keV level as being the 4^+ level of the γ band. The search for a 5^+ band member yields two possibilities, either a double level at 1630 keV or a double level at 1664 keV. If 1664 keV level is not assumed being as a double level, transitions to the 0^+ and 4^+ level restrict it only being a 2^+ level. A 6^+ level of the band around 1800 keV is expected based on the systematic information of the band, but it is unlikely that the level is observed.

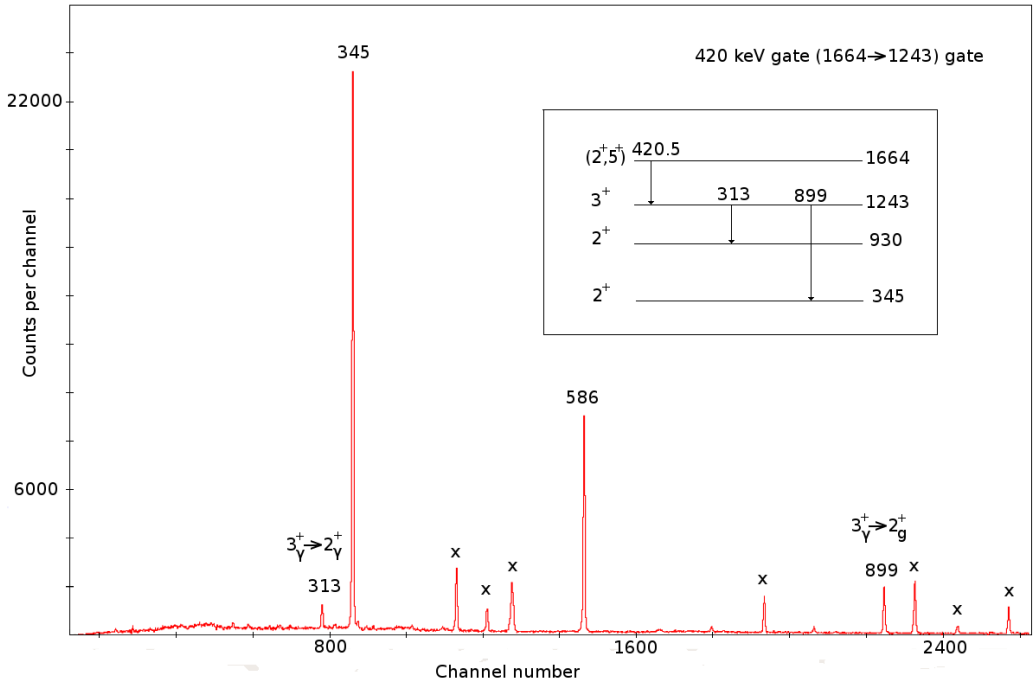

Figure 57: The 420 keV gated spectrum is shown to illustrate the coincidence relations of the γ band members. The 420.5 keV γ ray connects the 1664 keV state with the 3^+_γ state. Gamma rays not of interest are shown with $\times$.

7.2.4 The $\beta\gamma$ band

The literature [22] proposes for the N=88 isotones a $\beta\gamma$ band starting at about the sum of the bandheads of β and γ bands. For ^{156}Er, the sum would be around 1860 keV in energy. The coupling of one phonon of γ-vibration to one phonon of β-vibration constitutes the two-phonon $\beta\gamma$ bandhead. Additionally, the band members are expected to decay to the one-phonon bands with almost equal strength. The 1570.6 keV level is a good candidate with transitions to both one-phonon states with almost equal reduced strength (see Table 3), even though the level energy is lower than the expected energy range. The 3^+ member of the band would most likely be the 1917.9 keV level due to a 346.9 keV γ ray with a large B(E2) to the 1570.6 keV level. The energy difference is also in agreement with the energy differences of the lowest two members of the β and γ bands. There are a number of candidates above 2 MeV for higher members of the band.

7.2.5 The β' and other positive-parity bands

One of the accomplishments of this study is identifying a positive-parity band starting with the 0^+, 1380.5 keV level. Transitions to the lowest 2^+ levels from this level and the expected structure support the 0^+ spin-parity and that it is the head of β' band. The 2^+ member of the band may be 1710.7 keV level. The 330.0 keV γ ray de-exciting the 1710.7 keV level has the highest reduced transition probability among all γ rays depopulating the level. For the rest of the band, there are many candidates with uncertain spin parities above 2 MeV. The coincidence relation of the γ rays in the 330 keV gated spectrum is shown in Figure 45. The 330 keV γ ray connects the $2^+_{\beta'}$ state with the $0^+_{\beta'}$ state.

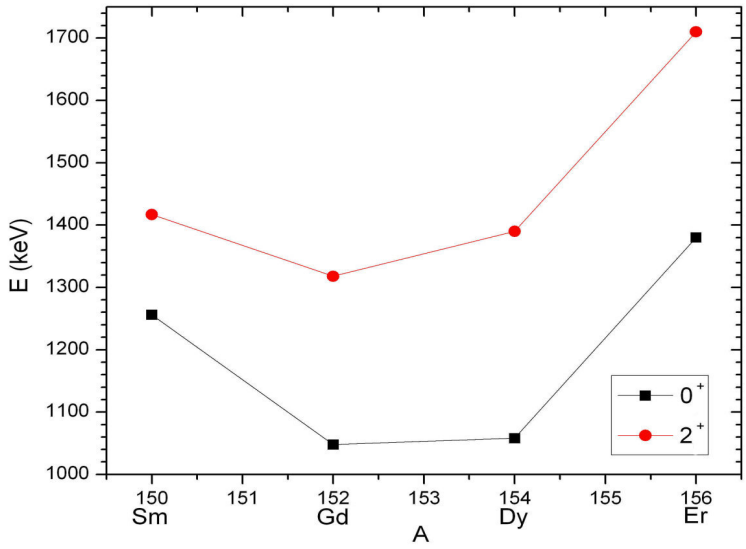

Figure 58: The 0^+ and 2^+ level systematics of β' band of the N=88 isotones. The upturn at ^{154}Dy is notable. The energy spacing of the members β' band of ^{156}Er are similar to the neighboring isotones. (The data, except for ^{156}Er, are taken from *Nuclear Data Sheets* [3, 4, 5].)

The energy spacings between band members of the β' band are similar to the positive-parity β-vibrational bands of ^{156}Er and the neighboring N=88 isotones. The systematics and the energy differences are shown in Figure 58. The band shows a similar pattern of the β vibrational band, a decrease in energy from ^{150}Sm, then a stable energy range for ^{152}Gd

and ^{154}Dy, and finally an increase for ^{156}Er. There is a lack of data for ^{158}Yb to make interpretations.

The 1406.1 keV level is either possibly a new positive-parity band member with the spin-parity 2^+ with an unobserved 0^+ level or a possible K=4 bandhead. If the first assumption is true, it is reasonable to suggest that the 0^+ level of this band is not observed. If the second assumption is true, there are many candidates for higher levels. The γ-ray transitions from this level to the 2^+ and 4^+ levels are notable in evaluation of the level and the systematics of the band. Additionally, the 475.6 keV γ ray from the level has the highest reduced transition probability.

7.3 Negative parity bands

In the following sections, the placement of the negative-parity bands will be explained. A detailed relation for the negative-parity states with the B(E2) transition probabilities (normalized to the largest B(E2) value from the level) are shown in Figure 62. The figure also involves the unplaced levels.

7.3.1 Negative parity odd-spin band

The bandhead is a 3^- level at 1303.7 keV followed by 1^- level at 1518.0 keV. The transitions from the 1303.7 keV level to the 2^+ and 4^+ levels and the transitions from the 1518.0 keV level to the 0^+ and 2^+ levels of ground-state band support the 3^- and 1^- assignments of the levels. The 5^- member is identified as the 1611.9 keV level. Transitions from the 1611.9 keV level to the 6^+ level, to the 4^+ level, and a weak transition to the 3^- level provide evidence for the 5^- nature of the 1611.9 keV level.

A recent in-beam spectroscopy study, [58], also confirms the 1611.9 keV level as 5^- spin-parity. They performed angular correlations and found a weak transition, a 417.3 keV γ ray which we have not observed, between the 7^- and 5^- levels of the band. The rotational spin-energy relations are shown in Figure 59.

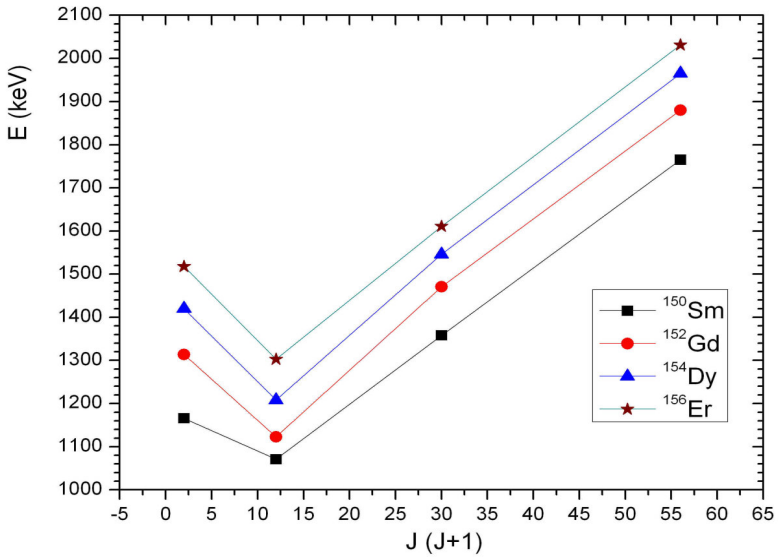

Figure 59: The negative-parity odd-spin band systematics of the N=88 isotones. A smooth decrease in all nuclei from the 3^- level to the 1^- level and a smooth increase afterwards are observed in all isotones. (The data are taken from *Nuclear Data Sheets* [3, 4, 5], except for ^{156}Er.)

7.3.2 Negative-parity even-spin band

The lowest member for a K-even band is expected to be a 2^- level. The best candidate for this level is the 1630.6 keV level. As explained in Section 6.1.8, the transition to the 4^+ level is forbidden which recalls a double state at or around 1630 keV. The degeneracy also explaines the ∼0.5 keV energy difference of the Ritz combination of the γ rays out of the level.

The 4^- level at 1814.7 keV in literature [1] is confirmed in our study. The newly observed intraband transition [58], the 390 keV γ ray from the 6^- to the 4^- level, which we have not observed, gives strength to our assesment that this level is a 4^- level. An intraband transition between the 4^- and 2^- levels is expected but not observed. The recent study [58] identified the 6^- level at 2203 keV in the corresponding band. We observed a 863.9 keV transition to the 6^+_g state from the same level. The rotational energy systematics of the negative-parity even-spin band for the N=88 isotones are shown in the Figure 60.

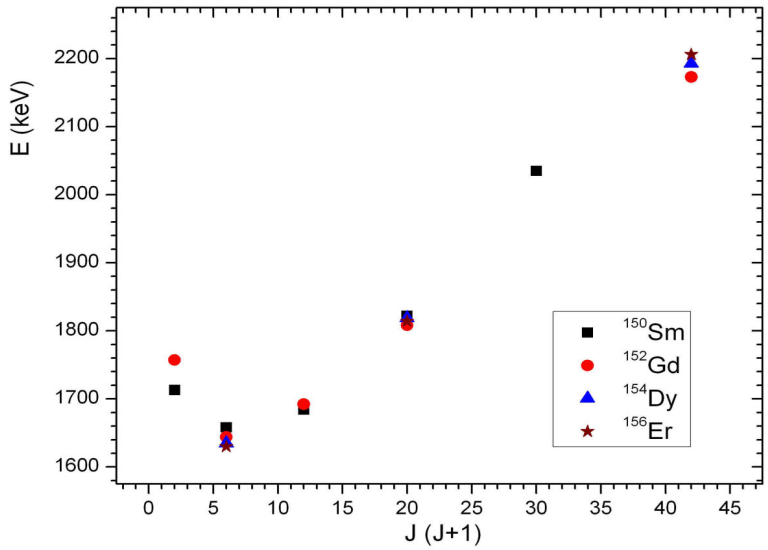

Figure 60: The negative-parity even-spin band systematics of the N=88 isotones. An overlap of energies for all isotones is evident. (The data are taken from *Nuclear Data Sheets* [3, 4, 5], except for ^{156}Er.)

7.4 Model Descriptions

7.4.1 Model Descriptions for Positive-Parity States

The transitional nature of the N=88 isotones makes it almost impossible to offer a specific model to explain the structure. If a nucleus is weakly deformed, it is often called a *soft rotor*. The leading property to examine is the ground-state band energy ratio $E_{4_1^+}/E_{2_1^+} \equiv R_4$. In a given nucleus, the ratio is 2.00 for the spherical-vibrational limit, and 3.33 for the rigid rotor limit.

A comparison of the ground-state bands of the Er isotopes provides information for elucidating the structure of the ground-state band. The ground-state band of ^{156}Er reveals the transitional nature of this nucleus, shown in Figure 63. The R_4 value ranges from 1.45 for ^{150}Er to 3.23 for ^{162}Er, where ^{156}Er lies in between with $R_4 = 2.31$, which is closer to the vibrational limit.

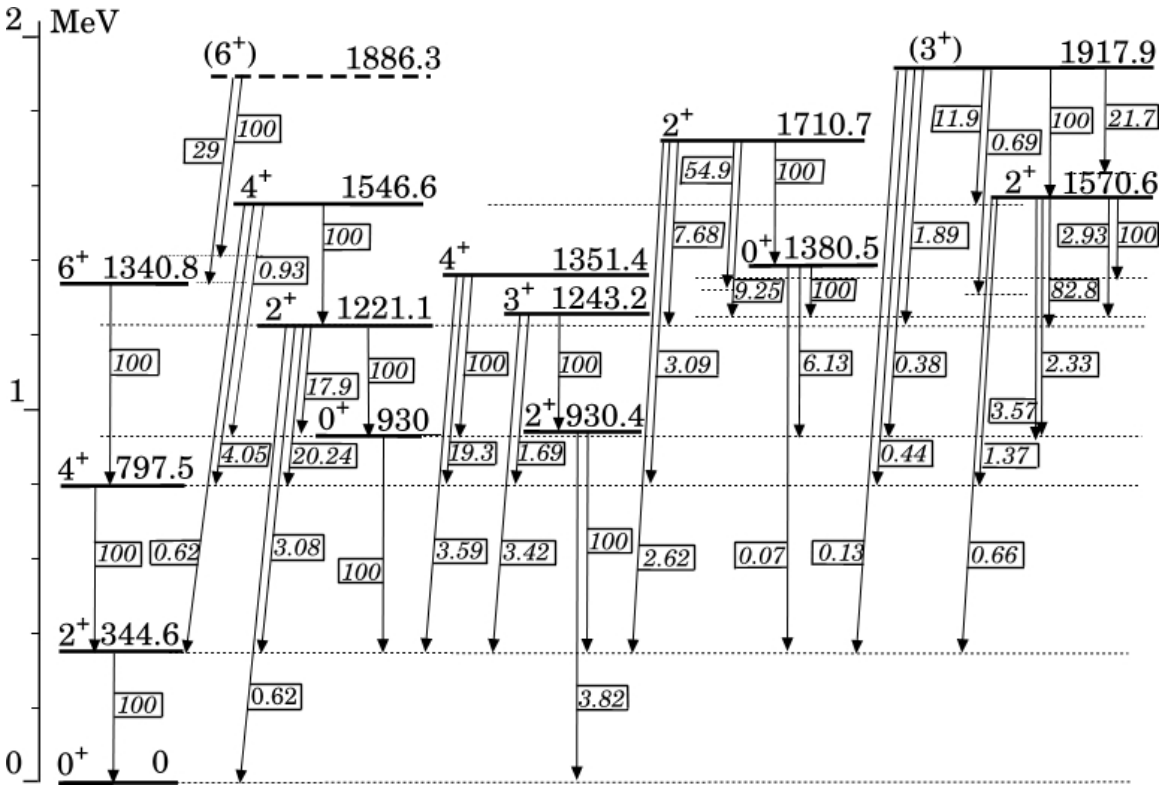

Figure 61: The placement of the low-lying positive-parity levels of ^{156}Er. The B(E2) values are shown along with the transitions. The levels are placed into rotational bands. The B(E2) values are normalized to the largest B(E2) value from the level.

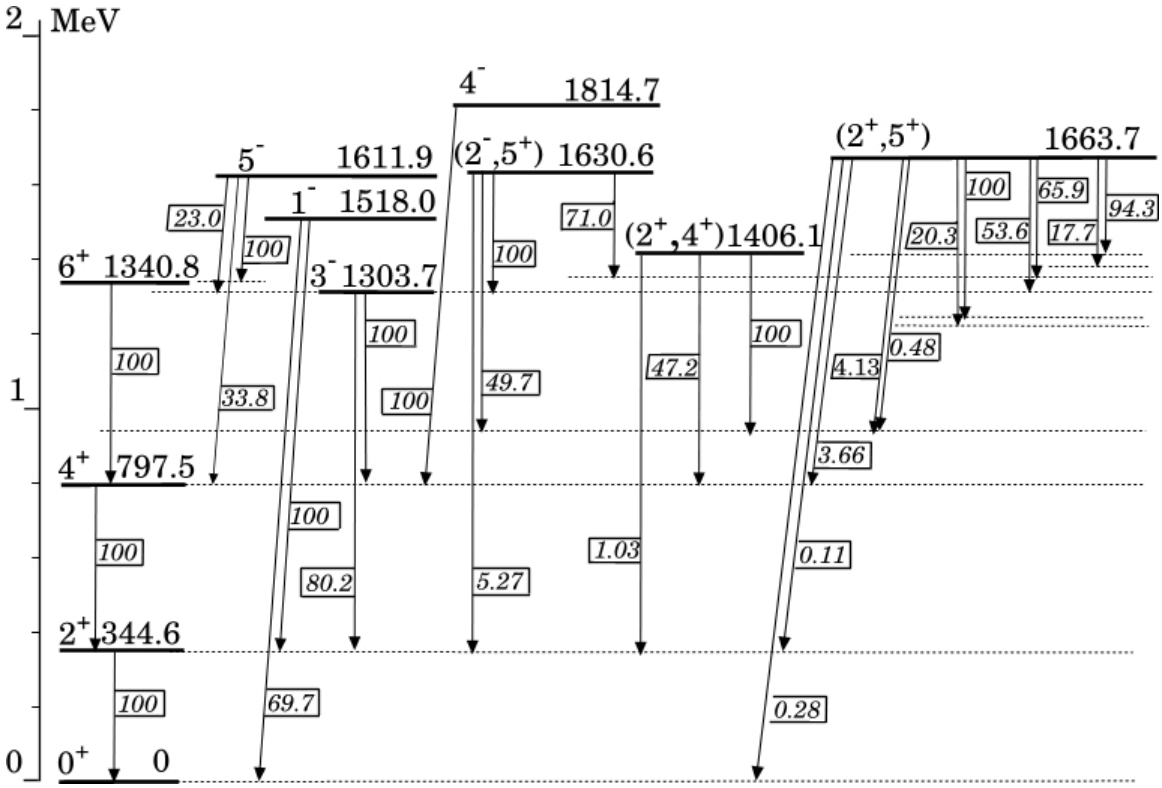

Figure 62: The placement of the low-lying negative-parity levels of ^{156}Er is shown along with some uncertain levels. The levels are placed into rotational bands. The B(E2) values which are are normalized to the largest B(E2) value from the level are shown along with the transitions.

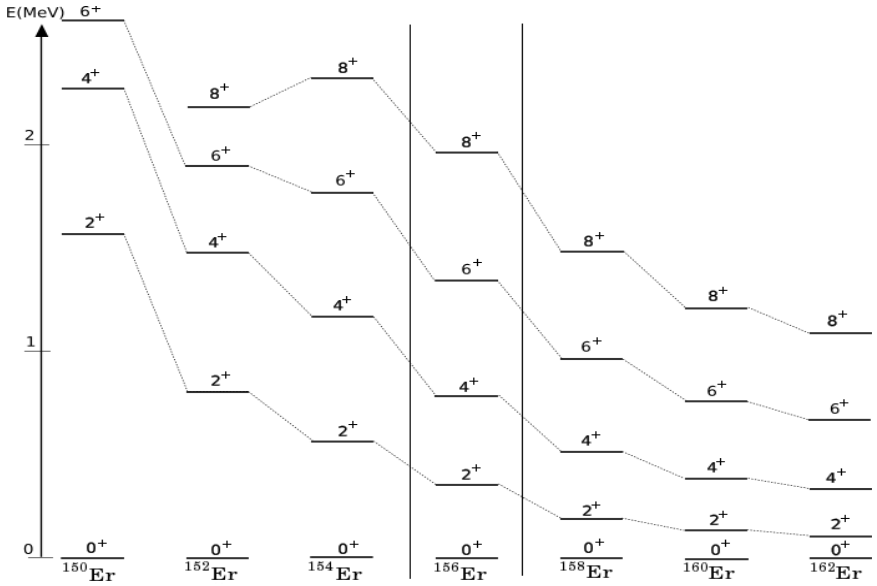

Figure 63: The ground-state bands of $^{150-162}$Er are illustrated. (The data are taken from *Nuclear Data Sheets* for A=150,...,162), except A=156.

The lifetimes of the ground-state band memebers are given in [1]. The lifetimes provide the absolute B(E2) values. The lifetimes are 1.9(3) ps, 5.0(3) ps, and 34.0(9) ps for 6^+, 4^+, and 2^+ levels, respectively. The ratio of the reduced transition probabilities for $B(E2; 4_1^+ \rightarrow 2_1^+)/B(E2; 2_1^+ \rightarrow 0_1^+)$ is 1.73.

If the nucleus is assumed to have a vibrational nature, a two-phonon triplet at twice the energy of the first excited 2^+ state is expected. In the harmonic vibrator model, the two-phonon states are expected to occur at ∼700 keV. The closest possible two-phonon members in the structure could be the 4_1^+ level at 798 keV, the 0_2^+ and 2_2^+ levels, both at 930 keV, despite the energy difference of ∼230 keV for 0_2^+ and 2_2^+ levels, with respect to ∼ 700 keV. The transition from 2_2^+ to 0_g^+ level disobeys the selection rule, $\Delta n = \pm 1$, for phonons which rules out that the 2_2^+ level is a two-phonon triplet member. A three-phonon quintuplet should give 0^+, 2^+, 3^+, 4^+ and 6^+ states. Best candidates would be the 0^+ state at 1380.5 keV, the 2^+ state at 1221.9 keV, the 3^+ state at 1243.2 keV, the 4^+ state at 1351.4 keV and the 6^+ state at 1340.8 keV. However, transitions to the 2^+ ground state from all of the states above (except from the 1340.8 keV state), and a transition from the 1221.9 keV level to the 0_g^+ preclude the three-phonon vibrational interpretation of these levels.

The "multiphonon" band, the $\beta\gamma$ band would be starting around twice of the sum of the energies of the bandheads of β and γ bands for ^{156}Er. The multiphonon structure signifies a deformed vibration. The $\beta\gamma$ bandhead would be at 1860 keV (sum of the energies of the 0^+_β and 2^+_γ), if the band built on 930 keV is assumed to be $\beta\gamma$ vibration. The coincidence relations of γ rays and B(E2) values do not give sufficient information about the 1860.1 keV level as being one of the bandheads of a multi-phonon band. The bandhead of the $\beta\gamma$ band can be interpreted as 1570.6 keV (see section 7.2.4.), which is lower than the expected energy.

It is possible to extract intrinsic structure information using the B(E2) values between two states. Alaga rules [59] are useful in determining K values and testing the nuclear wave functions [60]. In Table 4, some Alaga ratios calculated for the ^{156}Er, are given. The B(E2) ratios for transitions out of the γ band are much closer than the B(E2) ratios of the transitions out of the β band. The large deviations of the transition out of the β band might be attributed to mixing.

In even-even nuclei, it is common to see band mixing. The β' band, starting at 1380.6 keV and the β band, starting at 930.0 keV exhibit mixing. A 160.1 keV transition with a large relative B(E2) out of the 1380.6 keV level to the 2^+_β level adds strength to the mixing.

The γ band of even-even nuclei is described by many models in the literature. The N=88 isotones exhibit a systematic staggered spacing, e.g., a large spacing between the 2^+ and 3^+ levels, a small spacing between the 3^+ and 4^+ levels, again a big spacing between the 4^+ and 5^+ levels and so on. The same systematics is observed in ^{156}Er, albeit with undetermined levels above 4^+. The Wilets-Jean model [61] is successful in explaining the unusual spacings. The model is also called γ-unstable rotor in which the levels are classified as 0^+; 2^+; 2^+, 4^+; 0^+, 3^+, 4^+, and 6^+; 2^+, 4^+, 5^+, 6^+, and 8^+ for the quantum numbers 0, 1, 2, 3, and 4, respectively. The energies are given by the equation

$$E(\lambda) = c\lambda(\lambda + 3) \tag{35}$$

where c is a constant and λ is the quantum number. In the Wilets-Jean model, the spacing between the 3^+ and 4^+ states, and between 5^+ and 6^+ states is very small as observed in ^{156}Er.

Table 4: The ratio of B(E2) values for the decay of some levels. The experimental values are compared with the theoretical Alaga ratios.

B(E2) ratio	**Alaga**	**^{156}Er**
$\frac{B(E2;2^+_\gamma \rightarrow 0^+_g)}{B(E2;2^+_\gamma \rightarrow 2^+_g)}$	0.70	0.04
$\frac{B(E2;2^+_\gamma \rightarrow 4^+_g)}{B(E2;2^+_\gamma \rightarrow 2^+_g)}$	0.05	N/A
$\frac{B(E2;3^+_\gamma \rightarrow 2^+_g)}{B(E2;3^+_\gamma \rightarrow 4^+_g)}$	2.50	2.03
$\frac{B(E2;4^+_\gamma \rightarrow 2^+_g)}{B(E2;4^+_\gamma \rightarrow 4^+_g)}$	0.34	0.19
$\frac{B(E2;4^+_\gamma \rightarrow 6^+_g)}{B(E2;4^+_\gamma \rightarrow 4^+_g)}$	0.09	N/A
$\frac{B(E2;2^+_\beta \rightarrow 0^+_g)}{B(E2;2^+_\beta \rightarrow 2^+_g)}$	0.70	0.20
$\frac{B(E2;2^+_\beta \rightarrow 4^+_g)}{B(E2;2^+_\beta \rightarrow 2^+_g)}$	1.80	6.57
$\frac{B(E2;4^+_\beta \rightarrow 2^+_g)}{B(E2;4^+_\beta \rightarrow 4^+_g)}$	1.10	0.15

.

7.4.2 Model Descriptions for Negative-Parity States

The negative-parity bands in the ^{156}Er can be interpreted in terms of different types of models [22, 62, 63]. The "reversed order" of the 1^- and 3^- states is seen in all of the N=88 isotones. The band has K=0 because of the lack of even-spin states. The coupling of the state with other states or possibly with K=1 state might have created the inversion in the first two states, as suggested in the reference [64]. It is possible that Coriolis mixing [65] produced distortions of the energies of the states. The mixing occurs when states differ by $\Delta K = \pm 1$. The mixed states are repelled. The low-lying negative-parity bands in the N=88 isotones are shown in Figure 64.

It has also been proposed by Sunyar *et al.* that the negative-parity bands of ^{156}Er can be defined as rotational bands built on two-quasiparticle states. Octupole deformation has

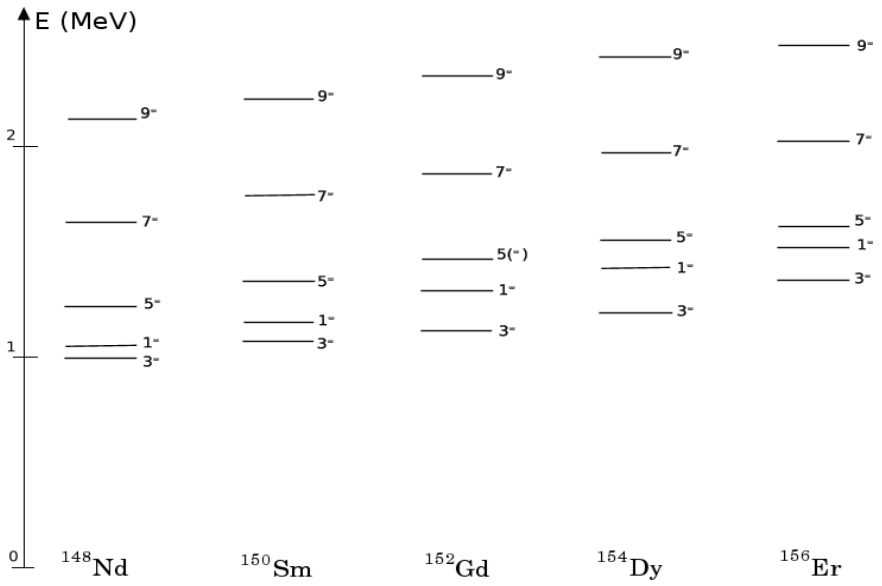

Figure 64: The low-lying negative-parity bands of the $N = 88$ isotones. The similarity of the band structure is clearly visible with approximately equal energy spacing. The inverted order of the 1^- and 3^- states is shown. (The data are taken from *Nuclear Data Sheets* [2, 3, 4, 5], except for ^{156}Er)

not been proven so far but Zamfir *et al*. have suggested that the N=88 isotones are good candidates to detect octupole deformation if it exists.

The quadrupole-octupole coupling model (QOC) for negative-parity states of ^{156}Er [22] was successful in describing the negative-parity states. It gave 1531 keV for a 1^- level, 1306 keV for a 3^-, and 1612 keV for a 5^- which agree with our results of 1518, 1304 and 1612 keV, respectively. (Below ^{148}Nd, the 3^- state moves above of the 1^- state which is consistent with their QOC calculations.) The even-spin negative-parity consistency with QOC model is rather weak. It gave 1679 keV for a 2^- level, 1797 keV for a 4^-, and 2211 keV for a 6^-. Only 4^- level agrees with our results to a certain extent.

CHAPTER VIII

CONCLUSION

The data for the decay of ^{156}Tm to ^{156}Er obtained with the 8π Spectrometer at TRIUMF provide a large amount of spectroscopic data. The γ-γ coincedence data has been analyzed using standard spectroscopic techniques and software.

This study extends the knowledge about the ^{156}Er low-energy low-spin structure and thus the knowledge of N=88 isotones. The placement of $\sim$700 γ rays along with 261 levels adds new insight to the structure of ^{156}Er. The spins and parities of some levels are determined through decay branches. The intensities of the γ rays are determined through a newly established method of coincidence intensities. The relative B(E2) values along with the rotational energy spacings helped to assign states to bands.

The newly established ($\beta^{'}$) band starting with a 0^+ state at 1380.5 keV, is one of the prominent outcomes of this study. The $\beta^{'}$ band is also observed in the neighboring isotones. The refutation of the spin-parity of 2^+ for the 1406.2 keV level changes the structure of ^{156}Er dramatically. The separation of nearly degenerate 0^+ and 2^+ states ($\Delta E < 1$ keV) at $\sim$930 keV was essential to the identification of the β and γ bands.

In terms of model descriptions, it is not easy to offer a unified-model description for this transition region of the Nuclear Chart. Some models are presented which explain ^{156}Er with only limited success. The complicated structure of the N=88 isotones requires more sophisticated models in order to obtain a deeper understanding of this transitional region..

The study also suggests that further investigation is needed for ^{156}Er. Angular correlations would be very useful for determining the spin assignments of the levels and the mixing ratios of the electromagnetic transitions. Conversion-electron data for ^{156}Er are also needed to determine multipolarities and to make E0 transition assignments. The measurement of

the lifetimes of the levels should also be carried out to determine the absolute B(E2) values which will be of great importance in structural analysis and model descriptions. A detailed study for ^{154}Dy would also be useful. Additionally, data for ^{158}Yb are completely missing. A study on this nucleus would shed more light on the systematics of the N=88 isotones.

REFERENCES

[1] C.W. Reich, Nuclear Data Sheets **99**, 753 (2002).

[2] M.R. Bhat, Nuclear Data Sheets **89**, 797 (2000).

[3] E. derMateosian and J.K. Tuli, Nuclear Data Sheets **75**, 827 (1995).

[4] A. Artna-Cohen, Nuclear Data Sheets **79**, 1 (1996).

[5] C.W. Reich and R.G. Helmer, Nuclear Data Sheets **85**, 171 (1998).

[6] M.G. Mayer, Phys. Rev. **75**, 1969 (1949).

[7] M.G. Mayer, Phys. Rev. **78**, 16 (1950).

[8] O. Haxel, J.H.D. Jensen, and H.E. Suess, Phys. Rev. **75**, 1766 (1949).

[9] O. Haxel, J.H.D. Jensen, and H.E. Suess, Z. Physik **128**, 295 (1950).

[10] N. Bohr and F. Kalckar, K. Dan. Vidensk. Selsk. Mat. Fys. Medd **14**, No.10 (1937).

[11] A. Bohr, K. Dan. Vidensk. Selsk. Mat. Fys. Medd. **26**, (1952).

[12] A. Bohr and B.R. Mottelson, Nuclear Structure, Vol. 2 (W.A. Benjamin, Inc., Reading, Ma, 1975).

[13] D.L. Hill and J.A. Wheeler, Phys. Rev. **89**, 1102 (1953).

[14] K.S. Krane, *Introductory Nuclear Physics*, (John Wiley & Sons, Inc., New York, 1987).

[15] V.F. Weisskopf, Phys. Rev. **83**, 1073 (1951).

[16] H. Morinaga, Phys. Rev. **101**, 254 (1956).

[17] K. Heyde, P. van Isacker, M. Waroquier, J.L. Wood, and R.A. Meyer, Phys. Rep. **102**, 291 (1983).

[18] J.L. Wood, K. Heyde, W. Nazarewicz, P. van Duppen, and M. Huyse, Phys. Rep. **215**, 101 (1992).

[19] J.L. Wood, E.F. Zganjar, C. De Coster, and K. Heyde, Nuc. Phys. A **651**, 323 (1999).

[20] K.S. Toth, R.L. Hahn, and M.A. Ijaz, Phys. Rev. C **4**, 2223 (1971).

[21] P. Aguer, C.F. Liang, J. Libert, P. Paris, A. Peghaire, A. Charvert, R. Duffait, and G. Marguier, Nuc. Phys. A **252**, 293 (1975).

[22] D.R. Zolnowski, M.B. Hughes, J. Hunt, and T.T. Sugihara, Phys. Rev. C **21**, 2556 (1980).

[23] J.O. Newton, in *Nuclear Spectroscopy and Reactions*, Part C, Vol.40-C of *Pure and Applied Physics*, edited by J. Cerny (Academic Press, New York, 1974).

[24] R.M. Diamond, F.S. Stephens, W.H. Kelly, and D. Ward, Phys. Rev. Lett. **22**, 546 (1969).

[25] B. Bochev, S. Iliev, R. Kalpakhcieva, S.A. Karamyan, T. Kutsarova, E. Nadzhakov, T. Venkova, Yad. Fiz., **30**, 593 (1979);
Sov. J. Nucl. Phys. **30**, 305 (1979).

[26] F. Azgui, H. Emling, W. Spreng, H.J. Wollersheim, R. Kulessa, T. Byrski, F.A. Beck, G.J. Costa, J. Dudek, B. Haas, C. Gehringer, J.C. Merdinger, R. Seltz, J.P. Vivien, and W. Nazarewicz, Z. Phys. **A320**, 699 (1985).

[27] F.S. Stephens, M.A. Deleplanque, R.M. Diamond, A.O. Macchiavelli, and J.E. Draper, Phys. Rev. Lett. **54**, 2584 (1985).

[28] M.K. Craddock, K.L. Erdman, and J.T. Sample, Nature **270**, 671 (1977).

[29] P.G. Bricault, M. Dombsky, P.W. Schmor, and G. Stanford, Nuc. Instrum. Meth. in Phys. Res. B **126**, 231 (1997).

[30] M. Dombsky, D. Bishop, P. Bricault, D. Dale, A. Hurst, K. Jayamanna, R. Keitel, M. Olivo, P. Schmor, and G. Stanford, Rev. of Scien. Inst. **71**, 978 (2000).

[31] J.M D'Auria, Nucl. Instrum. Meth. in Phys. Res. B **99**, 330 (1995).

[32] U. Köster, The Euro. Phys. Jour. A **15**, 255 (2002).

[33] http://www.triumf.info/wiki/exp-prog/*img_auth.php*/5/56/Target.jpg

[34] http://www.triumf.ca/isac/2007-01-24/is-24jan2007.jpg

[35] R. Silberberg, C.H. Tsao, The Astro. Jour. Suppl. Series **220(I)**, 315 (1973).

[36] R. Silberberg, C.H. Tsao, The Astro. Jour. Suppl. Series **220(II)**, 335 (1973).

[37] J.P. Martin, D.C. Radford, M. Beaulieu, P. Taras, D. Ward, H.R. Andrews, G. Ayotte, F.J. Sharp, J.C. Waddington, O. Häusser, and J. Gascon, Nucl. Inst. Meth. A **257**, 301 (1987).

[38] P.E. Garrett *et al.*, Acta Phys. Pol. B **38**, 1169 (2007).

[39] C.E. Svensson, R.A.E. Austin, G.C. Ball, P. Finlay, P.E. Garrett, G.F. Grinyer, G.S. Hackman, C.J. Osborne, F. Sarazin, H.C. Scraggs, M.B. Smith, and J.C. Waddington, Nucl. Inst. Meth. in Phys. Res. B **204**, 660 (2003).

[40] G.C. Ball *et al.*, J. Phys G **31**, S1491 (2005).

[41] G. Gilmore and J.D. Hemingway, *Practical Gamma-Ray Spectrometry* (John Wiley & Sons, Inc., New York, 1995).

[42] P.D. Schmelzenbach, Ph.D. dissertation, Oregon State University, (2003).

[43] W.D. Kulp, Ph.D. dissertation, Georgia Institute of Technology, (2001).

[44] J.M. Allmond, Ph.D. dissertation, Georgia Institute of Technology, (2007).

[45] A.H. Wapstra, in *Alpha-, Beta- and Gamma-Ray Spectroscopy*, edited by K. Siegbahn (North-Holland, Amsterdam, 1965), vol.1, p.539

[46] MIDAS, https://midas.psi.ch/intro/index.html

[47] ROOT, http://root.cern.ch/

[48] J. Kantele, *Handbook of Nuclear Spectroscopy* (Academic Press, Inc., San Diego, 1995).

[49] W.D. Kulp, J.L. Wood, K.S. Krane, J. Loats, P. Schmelzenbach, C.J. Stapels, R.-M. Larimer, and E.B. Norman, Phys. Rev. C **69**, 064309 (2004).

[50] W.D. Kulp, J.L. Wood, J.M. Allmond, J. Eimer, D. Furse, K.S. Krane, J. Loats, P. Schmelzenbach, C.J. Stapels, R.-M. Larimer, E.B. Norman, and A. Piechaczek, Phys. Rev. C **76**, 034319 (2007).

[51] D.C. Radford, Radware, http://radware.phy.ornl.gov/, (2005).

[52] D.C. Radford, *Notes on the use of the program gf3*, http://radware.phy.ornl.gov/gf3/gf3.html, (2000).

[53] BrIcc v2.2b (Conv. Coeff. Calc.), http://physics.anu.edu.au/nuclear/bricc/ (2009).

[54] T. Kibédi, T.W. Burrows, M.B. Trzhaskovskaya, P.M. Davidson, C.W. Nestor Jr., Nucl. Instr. Meth. in Phys. Res. A **589** 202 (2008). (Bricc calculator is set up based on the information in this paper).

[55] L.A. Currie, Anal. Chem **40**, 586 (1968).

[56] F. Azgui, Thesis Uni. Louis Pasteur de Strasbourg (1985); CRN/PN 85 31 (1985).

[57] N. Nica, Nuclear Data Sheets **108**, 1287 (2007).

[58] E.S. Paul, S.V. Rigby, M.A. Riley, J. Simpson, D.E. Appelbe, D.B. Campbell, P.T.W. Choy, R.M. Clark, M. Cromaz, A.O. Evans, P. Fallon, A. Görgen, D.T. Joss, I.Y. Lee, A.O. Macchiavelli, P.J. Nolan, A. Pipidis, D. Ward, and I. Ragnarsson, Phys. Rev. C **79**, 044324 (2009).

[59] G. Alaga, K. Alder, A. Bohr, and B.R. Mottelson, K. Dan. Vidensk. Selsk. Mat. Fys. Medd. **29**, No.9 (1955).

[60] R.F. Casten, *Nuclear Structure from a Simple Perspective* (Oxford University Press, Inc., New York, 2000).

[61] L. Wilets and M. Jean, Phys. Rev **102**, 788 (1956).

[62] A.W. Sunyar, E. derMateosian, O.C. Kistner, A. Johnson, A.H. Lumpkin, and P. Thieberger, Phys. Lett B **62**, 283 (1976).

[63] N.V. Zamfir, D. Kusnesov, and M. Babilon, Int. Jour. of Mod. Phys. E **14**, 147 (2005).

[64] D.R. Zolnowski, E.G. Funk, and J.W. Mihelich, Nucl. Phys. A **177**, 513 (1971).

[65] F.S. Stephens, Rev. Mod. Phys. **47**, 43 (1975).

VITA

Serkan Dursun was born in Yozgat, a small city in the central Turkey, in August 1979. He grew up in Yerkoy, a smaller city attached to Yozgat. He attended Ankara Anatolian High School's middle school section in Ankara, the capital city of Turkey, and moved to Izmir, a city in the western part of Turkey, where he graduated from the Izmir Fen High School. He received his B.S. degree in physics from Bogazici University, Istanbul, Turkey in 2003 and MS degree in physics from Georgia Institute of Technology in 2005, Atlanta, USA. He pursued his Ph.D degree in the Experimental Nuclear Physics under the supervision of Prof. John L. Wood.